Analysis of Flow, Breakage and Coating of Corn Seeds in a Mixer

by

Mehrdad Pasha

Submitted in accordance with the requirements for the degree of

Doctor of Philosophy

The University of Leeds
The School of Chemical and Process Engineering

September 2015

The candidate confirms that the work submitted is his own, except where work which has formed part of jointly-authored publications has been included. The contribution of the candidate and the other authors to this work has been explicitly indicated below. The candidate confirms that appropriate credit has been given within the thesis where reference has been made to the work of others.

Chapter 5 of this thesis has already been published in the Journal of Powder Technology as a jointly authored paper. The article can be found using the following citation:

M. Pasha, C. Hare, M. Ghadiri, A. Gunadi, P. M. Piccione, Effect of particle shape on flow in discrete element method simulation of a rotary batch seed coater, Powder Technology (2015). doi:10.1016/j.powtec.2015.10.055.

For the above publication, all the work has been carried out by the first author (Mehrdad Pasha) and the co-authors contributions to the publication were only supervisory.

This copy has been supplied on the understanding that it is copyright material and that no quotation from the thesis may be published without proper acknowledgement

© 2015 The University of Leeds and Mehrdad Pasha

Acknowledgements

I would like to take this opportunity to express my great thanks to Prof Mojtaba Ghadiri and Dr Colin Hare for their great encouragement, enthusiasm and technical assistance in supervising my PhD studies. They have been an excellent teacher and friend throughout this time.

The financial support from Syngenta Ltd. is gratefully appreciated. I would like to acknowledge my industrial coordinators, Dr Alfeno Gunadi, Dr Patrick Piccione and Dr Neil George, for their input into the direction of this research and providing the funding to this PhD program.

It has been a great pleasure to be a member of Ghadiri Research Group, which has a vibrant collaborative environment that has led to much friendship and enjoyment. I would particularly like to acknowledge the great help of Dr Graham Calvert and Dr Ali Hassanpour in useful discussions regarding this research. Past and present members of this research group have also helped to provide a great atmosphere in which to work and useful insight to aid the development of this research, namely Dr Afsheen Zarrebini, Dr Vincenzino Vivaqua, Dr Umair Zafar, Miss Tina Bonakdar, Mr Selasi Dogbe, Mr Siwarote Siriluck.

Many thanks to Dr Xiaodong Jia and Mr Rodrigo Guadarrama Lara for training me on Xray Micro Tomography at the University of Leeds. I would also like to thank Mr Robert Harris for construction and helping design the annular shear cell, along with numerous other technical jobs that were requested of him over the past 4 years. The help and support of Mr Ian Kay for all IT related issues is acknowledged.

A special thanks to Dr Massih Pasha for his great support and help during the course of this PhD program. Massih has not only been a great brother to me but also a great colleague for providing fantastic training and support for Distinct Element Method simulations of this PhD program.

Last but by no means least, I would like to convey an immeasurable amount of gratitude to my dearest parents, Mrs Alam Zarrebini and Mr Ahmadgholi Pasha, and to my sister and brother, Miss Leila Pasha and Dr Massih Pasha, for their unconditional love and support throughout the numerous ups and downs of my life.

To My Dear Parents

Abstract

In the seed processing industry, rotary batch seed coaters are widely used for providing a protective coating layer to the seeds consisting of various ingredients including fertilisers and crop protection chemicals. Seed motion and mixing are important in ensuring uniform coating; hence the focus of this work is to address the mixing efficiency and coating uniformity of corn seeds in a rotary batch seed mixer. In the present study, the Discrete Element Method (DEM) is used to analyse the motion and coating uniformity of the seeds. A comprehensive study has been carried out addressing the influence of the shape of corn seeds for accurately simulating their flow in the mixer using two commonly used techniques: (i) manipulation of coefficient of rolling friction of spherical particles, and (ii) clumping multiple spheres. Both methods were successful in simulating the flow of seeds in the mixer, however the former method is found to be an empirical approach rather than predictive.

A coating model is used for predicting the coating uniformity of corn seeds in the mixer. Effect of various process parameters on variation of coating mass among the seeds is investigated. For the seed mixer, the baffle clearance gap, baffle geometry and position of the atomiser disc were found to be the key influential process parameters affecting the coating uniformity of corn seeds. Other process parameters such as the base rotational speed, baffle angle, width and curvature had less effects on coating variability. A study has also been carried out on tailoring the existing methods of measuring the extent of breakage of particles for seeds. Four breakage criteria were proposed and assessed for consideration of mass of broken seeds, and the most suitable methods are suggested.

The simulations developed here are generic and can be applied to a wide range of coating processes, such as particle and tablet coating. The proposed methodology for measuring the extent of breakage of corn seeds can also be used for other types of seeds.

Table of Contents

Acknowledgements i

Abstract iii

Table of Contents i

List of Tables iv

List of Figures v

Nomenclature xi

CHAPTER 1 Introduction 1

1.1 Seed Coating 1

1.2 Seed Breakage 2

1.3 Objectives and Structure of the Thesis 3

CHAPTER 2 Literature Review 5

2.1 Material Characterisation 5

2.1.1 Density 5

2.1.2 Young's Modulus 6

2.1.3 Coefficient of Restitution 7

2.2 Breakage and Attrition 7

2.2.1 Breakage under Shear Deformation 8

2.2.2 Measurement of Seed Breakage 10

2.2.3 Concluding Remarks 12

2.3 Distinct Element Method 12

2.3.1 Time-step 13

2.3.2 Motion Calculations 13

2.3.3 Contact Force Models 14

2.3.4 Particle Shape 17

2.3.5 DEM Simulation of Seed Processing 21

2.4 Application of DEM to Seed Coating 24
2.5 Concluding Remarks 37
CHAPTER 3 Materials and Methods 38
3.1 Experimental Materials 38
3.2 Material Properties 39
3.2.1 Aspect Ratio 39
3.2.2 Coefficient of Restitution 40
3.2.3 Hardness and Young's Modulus 41
3.3 Particle Shape 44
3.3.1 Image Processing 46
3.3.2 Image Segmentation 46
3.3.3 Separation of Segments and Labelling 47
3.4 Method of Assessing Breakage 47
CHAPTER 4 Seed Breakage in a Shear Cell 50
4.1 Turnip Seed Breakage 51
4.1.1 Concluding Remarks 57
4.2 Corn Seed Breakage 57
4.2.1 Concluding Remarks 65
CHAPTER 5 Particle Velocity Distributions in the Mixer and the Effect of Particle Shape in DEM 66
5.1 Experimental Measurement of Particle Velocities 66
5.1.1 Lens Distortion Calibration 68
5.1.2 Perspective Correction 68
5.1.3 Experimental Particle Velocity Distributions 71
5.2 DEM Simulations of Effect of Particle Shape 72
5.2.1 Implementation of Clumped Spheres 74
5.2.2 Effect of the Rolling Friction Coefficient on Simulated Velocity Distributions 75

5.2.3 Effect of the Accuracy of Clumped Spheres on Simulated Velocity Distributions....78

5.3 Comparison of Experimental Results and Simulation Predictions....80

5.4 Concluding Remarks....83

CHAPTER 6 DEM Simulation of Coating Process....84

6.1 Coating Contact Model....84

6.2 Implementation of Droplet Generation in DEM Simulations....86

6.3 Effect of Process Parameters on Coating Uniformity of Corn Kernels....90

6.3.1 Baffle Angle and Clearance Gap to the Walls....91

6.3.2 Effect of Baffle Design on Coating Uniformity....95

6.3.3 Effect of Atomiser Disc Vertical Position....99

6.3.4 Effect of Base Rotational Speed on Coating Variability....101

6.3.5 Concluding Remarks....102

CHAPTER 7 Conclusions and Recommended Future Work....104

7.1 Conclusions....104

7.2 Recommended Future Work....107

References....108

List of Tables

Table 2.1: Measured density of corn kernels in the work of González-Montellano *et al*. [8] 6
Table 2.2: Behaviour of a bed of particles in a horizontal drum mixer [70] 25
Table 3.1: Various indenter specifications for calculation of projected imprint size [14]. 42
Table 4.1: Proposed analytical criteria for assessing breakage of seeds 51
Table 4.2: Shear cell experimental setup for turnip seeds 53
Table 4.3: Stresses applied to the bed of corns using dead weight 60
Table 5.1: Properties of particles and walls used in DEM simulations 74
Table 5.2: Contact properties used in DEM simulations 74
Table 6.1: Coating droplet collisional criteria in the proposed coating model 86
Table 6.2: Baffle angles and clearance gaps arrangements used in DEM simulations. 91

List of Figures

Figure 1.1: Seed processing stages.....1
Figure 1.2: Schematic diagram of the project plan 3
Figure 2.1: Schematic representation of forces acting on a particle. 14
Figure 2.2: Effective elastic modulus as a function of vertical lid pressure for pea (a) and bean (b) obtained from numerical simulations and experiments [7]. 22
Figure 2.3: Effect of calibrating particle-particle friction on flow patterns compared to the experiments for maize grains: (a) t=0T, (b) t=0.25T, (c) t=0.5T and (d) t=0.75T [58]. 23
Figure 2.4: (A) Average circulation time and (B) average surface time as function of rotational speed of the pan, where the error bars represent 95% confidence interval [78].....26
Figure 2.5: Effect of existence of baffles on tablets circulation time in horizontal rotating drum coater [68].....30
Figure 2.6: Schematic diagram of the spray zone in horizontal drum coaters [69]. ..31
Figure 2.7: Schematic of the top detection by introducing a discretised static plane [104] 33
Figure 2.8: Influence of the grid spacing on detection of particles on top of particle bed for (a) wide and (b) narrow spacing. The filled circles represent the particles being detected by top detection algorithm.....33
Figure 2.9: DEM simulation of tablet coating in a horizontal drum coater using spray drop model. The spray droplets are shown in blue, the lighter shades indicating smaller droplets. The tablets are coloured according to their coating mass where red colour showing high coating mass and white colour indicating tablets with no coating mass [69].....35
Figure 2.10: A) Principle of ray-tracing method where the blue and red dots are the centre position coated and uncoated particles, respectively. The vertical line represent the ray. B) Relative standard deviation of coating mass as a function of the number of rays [69] 36
Figure 3.1: Images of a number 1.18 – 1.4 mm turnip and 7.1 – 8.0 mm corn seeds. 39

Figure 3.2: Captured and binary image of corn seeds for aspect ratio measurements. 40

Figure 3.3: Loading and unloading curve obtained from indentation test with a maximum load of P_t and total penetration depth of h_t . dP/dh, h_a, h_p, h_r and h_e , are stiffness, depth of contact circle, depth of residual impression and displacement associated with elastic recovery during unloading, respectively.....41

Figure 3.4: Indentation load-displacement curves for four corn kernels at maximum indentation penetration depth of 1 µm. 43

Figure 3.5: Schematic diagram of X-ray Tomography principles. 45

Figure 3.6: Schematic representation of particle breakage modes.....48

Figure 4.1: Schematic diagram of slip between particles and groove rings.....52

Figure 4.2: Extent of breakage of 1.4 – 1.7 mm turnip seeds, subjected to shear strain corresponding to once cell rotation based on three definitions (R^+, R^- and R^*) using Criterion 1.....53

Figure 4.3: Extent of breakage of 1.4 – 1.7 mm turnip seeds as a function of strain for normal stress of 28 kPa. 54

Figure 4.4: Damage to the seeds in the range of 1 - 1.18 mm for (a) 3 kPa, (b) 4 kPa, (c) 7.7 kPa, (d) 20 kPa and (e) 28 kPa normal stresses. 54

Figure 4.5: Damage to the seeds in the range of 1.18 - 1.4 mm for applied normal stresses of (a) 3 kPa, (b) 4.3 kPa, (c) 7.7 kPa, (d) 20 kPa and (e) 28 kPa. 55

Figure 4.6: Schematic representation of collected damaged turnip seeds after shearing. 55

Figure 4.7: Comparison of the extent of breakage of 1.4 – 1.7 mm turnip seeds as a function of normal stress based on proposed the models.....57

Figure 4.8: Comparison of the extent of breakage of 1.4 – 1.7 mm turnip seeds as a function of strain at applied normal stress of 28 kPa based on the proposed criteria.....57

Figure 4.9: Schematic representation of new shear cell grooves. 58

Figure 4.10: Position of colour band seeds (a) before and (b) after shearing for measuring the bed slip angle against the top and bottom grooves. The highlighted area (shown in red colour) is the position of marked particles before shearing. 59

Figure 4.11: Calculated Strain as function of rotational angle. The error bars corresponds to the strain near the inner and outer wall of the cell. 59
Figure 4.12: Extent of breakage of 7.1 – 8.0 mm corn seeds subjected to shear strain of 11 (one rotation) as a function of applied normal stress based on three definitions (R^+, R^- and R^*) using Criterion 1. 61
Figure 4.13: Extent of breakage of 7.1 – 8.0 mm corn seeds as a function of applied normal stress for various applied shear strains.....61
Figure 4.14: Extent of breakage of 7.1 – 8.0 mm corn seeds as a function of applied shear strain for various applied normal loads.....62
Figure 4.15: Extent of breakage of 7.1 – 8.0 mm corn seeds subjected to a shear strain of 272 as a function of applied normal stress. 63
Figure 4.16: Extent of breakage of 7.1 – 8.0 mm corn seeds subjected to applied normal stress of 15.2 kPa as a function of applied shear strain. 63
Figure 4.17: Extent of breakage of 7.1 – 8.0 mm corn seeds as function of bed height subjected to applied normal force and strain of 15.2 kPa 330, respectively. 64
Figure 5.1: Particle tracking for obtaining tangential and radial velocity distributions of particles in the measurement cell located after the baffle; a) the region where the particle trajectories are analysed, b) detection of particles in the cell and c) representation of particle tracks within the region of interest67
Figure 5.2: Calibration for camera lens distortion error; a) calibration chart and b) error in calculating the positions with the reference point located at the centre of the camera lens.....68
Figure 5.3: Schematic diagram of the camera field of view. The green lines indicate the camera field of view away from the camera lens and the red and orange lines indicate the appearance of the inner surface of the coater wall in the obtained image due to the perspective view.....69
Figure 5.4: Schematic representation of position of the particles after the baffle 70
Figure 5.5: Calibration of field of view error as a function of distance from the top of the bed by considering same position on the calibration chart for all distances. 70
Figure 5.6: Assumption of bed profile after the baffle as a function of radial distance from the centre of the baffle. 71

Figure 5.7: Experimental tangential (a) and radial (b) velocity distributions in the measurement cell located after the baffle. 72
Figure 5.8: Measurement cells in DEM simulations for two positions in the vessel, one after (red) and another before (blue) the baffle 73
Figure 5.9: Three-dimensional structure of a corn seed obtained from XRT 74
Figure 5.10: Representation of Corn Seeds in DEM using (a) five, (b) ten, (c) fifteen and (d) twenty spheres 75
Figure 5.11: Predicted radial velocity distribution of particles in the measurement cell located after the baffle using rolling friction method 75
Figure 5.12: Predicted tangential velocity distribution of particles in the measurement cell located after the baffle using rolling friction method 76
Figure 5.13: Predicted radial velocity distribution of particles in the measurement cell located before the baffle using rolling friction method 77
Figure 5.14: Predicted tangential velocity distribution of spherical particles in the measurement cell located before the baffle using rolling friction method 77
Figure 5.15: Comparison of number of inter-particle contacts in the measurement cells located after and before the baffle for the simulation of rolling friction coefficient of 0.1. 78
Figure 5.16: Predicted radial velocity distributions of particles in the measurement cells located after the baffle using the overlapping spheres method 78
Figure 5.17: Predicted radial velocity distributions of particles in the measurement cells located before the baffle using the overlapping spheres method 79
Figure 5.18: Predicted tangential velocity distribution of particles in the measurement cell located after the baffle using the overlapping sphere method 80
Figure 5.19: Predicted tangential velocity distribution of particles in the measurement cell located after the baffle using the overlapping sphere method 80
Figure 5.20: Comparison of experimental results and simulation predictions for the measurement cell located after the baffle: (a) radial velocity; (b) tangential velocity 81
Figure 5.21: Comparison of radial velocity distribution of particles using clump sphere and rolling friction methods in DEM simulations 82
Figure 5.22: Comparison of radial velocity distribution of particles using clump sphere and rolling friction methods in DEM simulations 83

Figure 6.1:High-speed camera setup for measuring droplets size and velocity.....87
Figure 6.2: Measured droplet size distribution using high-speed video imaging 88
Figure 6.3: Measured droplet velocity distribution using high-speed video imaging88
Figure 6.4: Motion of de-ionised water droplets after being released from the atomiser disc. The coloured lines showing the tracked position of droplets in the high-speed video images. 89
Figure 6.5: Geometry of droplets factory used in DEM simulations. 90
Figure 6.6: Schematic representation of droplet generation and motion of the droplets being released from the atomiser disc in DEM simulations. 90
Figure 6.7: Schematic representation of baffle angle and clearance gap to the walls in the DEM simulations.....91
Figure 6.8: Schematic diagram of the original baffle design used for DEM simulations. 92
Figure 6.9: Standard deviation and CV of coating mass of corn kernels as a function of coating time for baffle angle and clearance gap of 45° and 15 mm, respectively.....93
Figure 6.10: Effect of baffle clearance gap to the walls of the coater on coating uniformity of corn kernels.....94
Figure 6.11: Effect of baffles angle on coating uniformity of corn kernels in DEM simulations 94
Figure 6.12: Baffles design used for investigation of effect of baffles width and face curvature on coating uniformity of corn kernels in DEM simulations. ..95
Figure 6.13: Effect of flatness and curvature of baffles on coating uniformity of corn kernels in DEM simulations.....96
Figure 6.14: Cross section view of corn kernels being sliced off from the bed surface as they approach one of the baffles at angle and clearance gap of 45° and 15 mm, respectively; each data point represents the centre point of a corn kernels and the orange line represents the position of the baffle. 97
Figure 6.15: New baffle design for controlling the proportionality of particles being sliced off from the bed surface. 97
Figure 6.16: Effect of baffles shape on coating uniformity of corn kernels in DEM simulations. 98
Figure 6.17: Cross sectional view of position of corn kernels approaching the baffle. 99

Figure 6.18: Schematic representation of atomiser disc position relative to the base of the coater. 100
Figure 6.19: Effect of vertical position of atomiser disc relative to the base of coater on coating uniformity of corn kernels in DEM simulations; the blue and green data points represent the original and optimised position of atomiser disc, respectively. 101
Figure 6.20: Effect of base rotational speed on coating variability of corn kernels in DEM simulations..... 102

Nomenclature

Latin Characters

A	Projected plastic area
A_{tot}	Unobscured projected surface area in coating
C_r	Damping constant
C_r^{crit}	Rolling critical viscous damping constant
d	Size of indenter, particle diameter
D	Deformation
D_c	Mean diameter of cell
D_x	Dispersion coefficient along the axis of a pan
e	Coefficient of restitution
f	Constant used in Elastic-plastic spring dashpot contact model, Gripping factor in annular shear cell
E	Young's modulus
E^*	Reduced Young's modulus
F	Applied Force, Contact force
F_c	Resultant contact forces acting on a particle
F_n	Normal component of the contact force acting on a particle
F_{nc}	Resultant Non-contact forces acting on a particle
F_g	Gravitational force
F_s	Shear component of the contact force acting on a particle
Fr	Froude number
G	Exponent in the Schuhmann formula, Shear modulus
G^*	Reduced shear modulus
h	Bed height in the annular shear cell
H	Hardness
I	Particle moment of inertia
I_r	Equivalent moment of inertia for relative rotational vibration
J_n	Coefficient in the Elastic-plastic spring dashpot contact model

k	Emperical constant in Paramanathan and Bridgwater formula, Particle stiffness
k_n	Normal stiffness
K_c	Fracture toughness
K_G	Proportionality constant in the Gwyn formula
K_N	Proportionality constant in the Neil and Bridgwater formula
K_0	Proportionality constant in the Ouwerkerk formula
K_U	Constant dependent on the minimum and maximum radii of curvature of sample
l	Characteristic particle size
l_{tab}	Relative axial position
m	Mass, empirical constant in Paramanathan and Bridgwater formula
$\bar{m}$	Average coating mass
m_{de}	Mass of debris
m_f	Mass of mother particles
m_i	Coating mass on the $i^{'th}$ seeds
m_m	Mass of mother particles
m_G	Exponent in the Gwyn formula
M	Resultant contact torque acting on a particle, total number of particles in the sample
M_r	Resistive torque between two particles in contact
M_r^d	Viscous damping torque
M_r^k	Spring damping torque
$M_{r,t}^k$	Spring damping torque at time t
p	Mass fraction
P_t	Maximum applied force
R	Radius
R^-	Attrition calculated assuming lost material is mother particles
R^+	Attrition calculated assuming lost material is debris
R^*	Reduced contact radius, Attrition calculated from collected material
R_r	Effective rolling radius

R_U	Maximum sample radius of curvature at point of contact with the tip of indenter
R'_U	Minimum sample radius of curvature at point of contact with the tip of indenter
R_y	Spray flux density constant
RSD	Relative standard deviation
RSD_r	Relative standard deviation of a random mixture
S	Stifness
t	Time
$t_{S,k}$	Spray zone residence time during the *k*th visit to the spray zone
T_R	Rayleigh time-step
v	Impact velocity
V	Particle velocity
W	Attrition

Greek Characters

α	Indenter effective cone angle
α_0	Logarithmic rate term in the Ouwerkerk formula
α_n	Normal overlap
β	Logarithm rate term of material degradation in the Neil and Bridgwater formula, Indenter geometry correction factor
ε	Strain
ε_{Dx}	Distortion error in *x* direction
ε_{Dy}	Distortion error in *y* direction
ε_{Px}	Error in position of particles relative to the centre point of the baffle in *x* direction
ε_{Py}	Error in position of particles relative to the centre point of the baffle in *y* direction
γ	Shear strain rate
Γ	Shear strain
ζ	Coating efficiency

η	Breakage propensity
η_k	Average exposed area percentage
η_r	Rolling viscous damping ratio
θ	Angle, Indenter semi-angle
θ_c	Cell rotation
θ_{sl}	Degree of slip against lower gripping ring
θ_{su}	Degree of slip against upper gripping ring
μ_w	Coefficient of wall friction
μ_r	Coefficient of rolling friction
υ	Poisson's ratio
ρ	Particle density
σ	Standard deviation
σ_{SCS}	Side-crushing strength
φ	Parameter describing the relative influence of stress and strain on material degradation
ω	Angular velocity
ω_{rel}	Relative angular velocity of two particles in contact

CHAPTER 1 Introduction

The majority of agricultural seeds in the market undergo a series of seed processing stages in order to improve their mechanical and physical properties, and germination quality. Once the seeds are harvested from the farm, they are sent for seed processing. The seed processing stages involve removal of corn kernels from cobs, drying the seeds to an optimum moisture level, cleaning the seed samples to remove unwanted materials, classification into different subsets based on size and shape, sorting the seeds to remove damaged and unwanted seeds and finally coating in order to improve their germination, immunity to insects and lifetime [1]. Figure 1.1 shows the common stages which are carried out during seed processing.

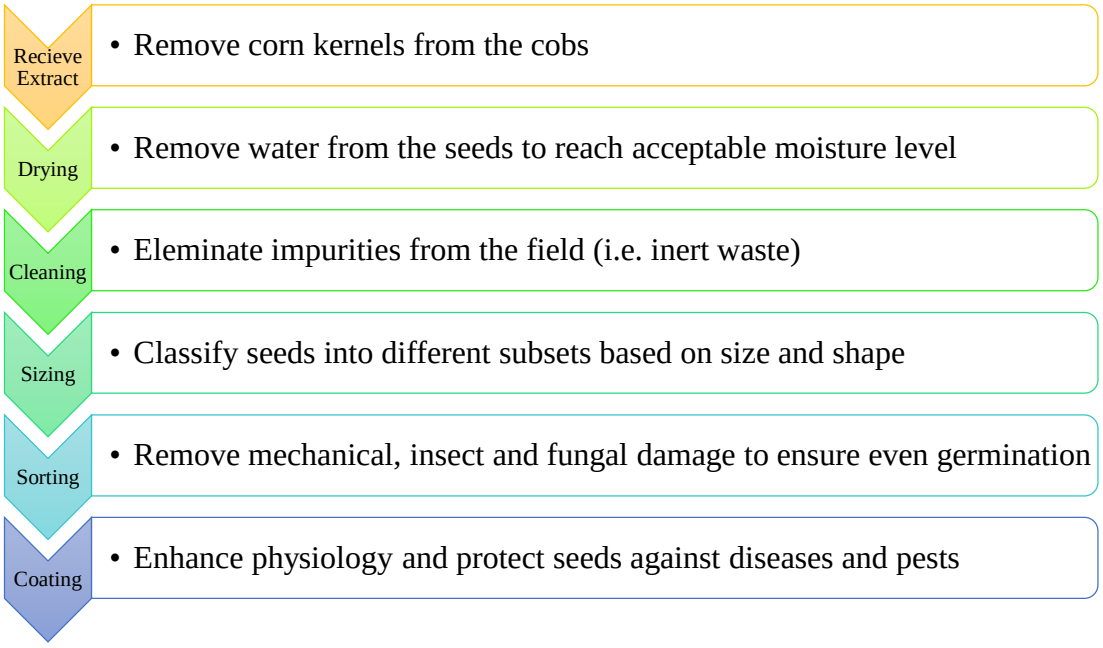

Figure 1.1: Seed processing stages

1.1 Seed Coating

Coating of particulate solids by a thin film layer is of interest in many industrial applications such as seed and tablet coating. In seed processing, seeds are commonly coated with a protective coating layer consisting of fertilisers and pesticides. The quality of the finished product is strongly dependent on the uniformity of the coated thin film on the seeds and the effectiveness of the coating liquid formulation. Rotary batch mixers are typically used for coating of corn seeds. The mixer consists of a

cylindrical vessel with a rotating atomiser disc in the centre, onto which the coating liquid is fed. The seeds are driven around the vessel by its rotating base, and are mixed by two baffles; one on either side of the vessel. Until now, there has been no work reported in the literature on understanding the dynamics of particle flow and effect of process parameters on coating uniformity of seeds in this type of mixer; hence the optimum process parameters are typically chosen by trial and error experiments. Although this type of optimisation may be adequate to meet the industrial standards, an in-depth knowledge of the effect of process parameters on the coating uniformity of the seeds is needed to optimise the coating process parameters further and consequently the quality of the finished product.

The Discrete Element Method (DEM) has attracted a lot of interest for the simulation of granular flow since it provides a wide range of information, which are relatively difficult to obtain from experimental work. In the present work is used to model the motion and coating process of corn seeds. In conventional DEM simulations, the particles are considered as spheres. Since the corn kernels are not spherical, and the motion of particles is influenced by their shape, a methodology for consideration of particle shape in DEM simulations is required. For this purpose, an extensive investigation is carried out to understand the effect of particle shape on flow of the corn seeds in the mixer by evaluating two commonly used methods; manipulation of coefficient of rolling friction to spherical particles and overlapping a number of spheres to generate the shape of the kernels.

1.2 Seed Breakage

As seeds are passed through various processing stages, they experience a portfolio of impact and shear stresses which may result in undesirable damage and quality degradation of seeds such as reduced probability of germination. Therefore, an in-depth study and understanding of the microscopic mechanisms of the various processes is needed to investigate and address the problem of seed damage. There exist a number of approaches in the literature for measuring the damage to particles by impact [2,3] and bulk shearing [4,5]. However, these methodologies need to be tailored for seed processing as any damage affecting germination quality must be considered. Paramanathan and Bridgwater [6] developed an annular shear cell for the purpose of measuring the extent of breakage of a range of particulate materials under various levels of stress and strain. In general, an increase in stress or strain applied to

the bed increases the extent of breakage. In the present work, turnip seeds were initially used as test material to establish the criteria in which the seeds are considered to be damaged in the annular shear cell and a similar approach was carried out for the corn seeds.

1.3 Objectives and Structure of the Thesis

The overall aim is to develop a coating uniformity prediction method for seed mixers and establish a method for analysis of seed breakage. The main objectives of the thesis are as follows:

(i) Investigation of the effect of particle shape on flow in a seed mixer in order to accurately simulate the mixing process in DEM.

(ii) Implementation of an appropriate DEM coating contact model for prediction of coating uniformity of corn seeds during the coating process.

(iii) Understanding of the effect of various process parameters on coating uniformity of corn seeds in the coating process.

(iv) Assessment of the extent of breakage of corn seeds under shear deformation.

The interaction between all the aspects of this thesis, optimisation of coating process parameters to achieve a more uniform coating, and assessment of the extent of breakage of agricultural seeds is shown in Figure 1.2.

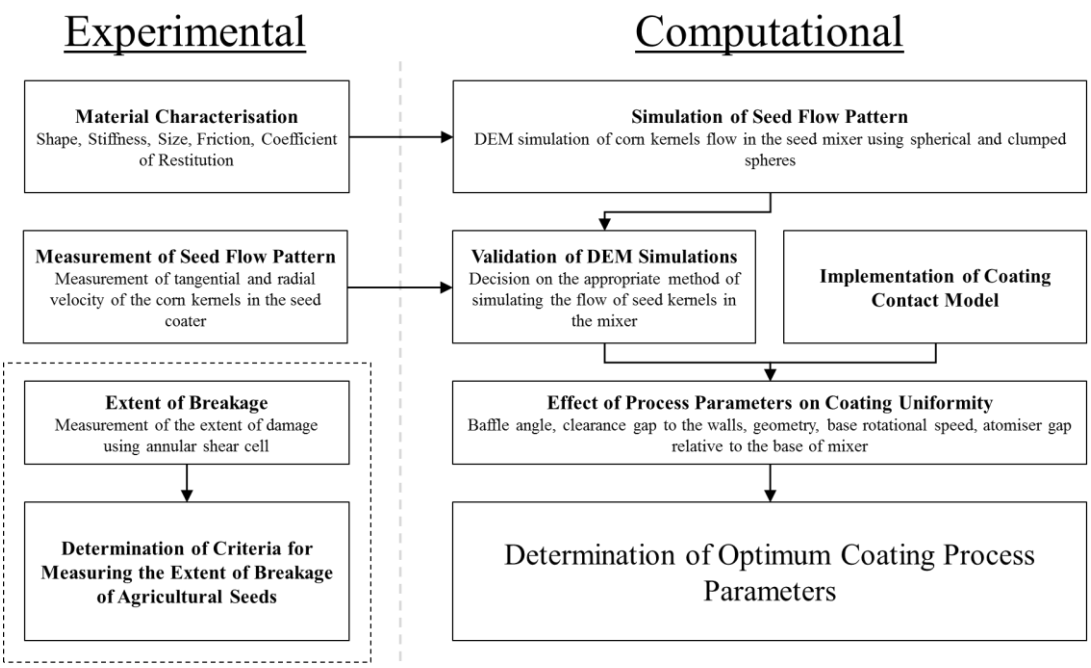

Figure 1.2: Schematic diagram of the project plan

Chapter 2 of this thesis covers the review of the literature on material characterisation of agricultural seeds as well as an overview of the current knowledge of measurement techniques for assessing the extent of breakage of agricultural seeds, particularly for corn seeds. Moreover, this chapter contains an overview of the application of DEM for seed processing, particularly for simulating the particle shape and coating. The details of the methods used for characterising corn seeds physical properties (e.g. hardness, Young's modulus, shape, etc.) is outlined in Chapter 3. The analysis of the extent of breakage of turnip and corn seeds is given in Chapter 4. In Chapter 5, the experimental and simulation results for the effect of particle shape on flow using two commonly used methods, addition of rolling friction and use of clumped-spheres, are presented. Chapter 6 covers the details of the coating contact model used, and the effect of various process parameters on coating uniformity of corn seeds in the seed coater. Finally, a summary of the findings of the thesis, concluding remarks and possible future works are covered in Chapter 7.

CHAPTER 2 Literature Review

2.1 Material Characterisation

Granular material such as corn, nuts and rice are important constituents in various food processes such as coating, transport, storage and drying. In order to model and understand the dynamics of such processes, material characterisation and knowledge of how materials and equipment interact within the processes is required. An accurate physical, mechanical and chemical characterisation of granular materials may result in more precise modelling of such processes [7]. The interactions between the materials and various items of equipment have been studied in the past using various analytical approaches, however they have not provided reliable results due to the complexity of the systems [8]. The Discrete Element Method (DEM) can be used to overcome the failings of analytical methods in the case of complex systems involved in seed processing [8].

In order to model the dynamics and behaviour of the seeds in DEM, various material properties such as Young's modulus (E), shear modulus (G), Poisson's ratio (υ), particle density (ρ_p), coefficient of restitution (e) and coefficient of friction (μ) are required [9]. These material properties can be either measured directly or estimated using calibration techniques. In the case of irregularly shaped particles, direct measurement of some of microscopic properties, such as Poisson's ratio and coefficient of friction. Hence, calibration by simulations has been commonly used for measurement of these particular parameters [10–12]. The calibration procedures are based on simple laboratory experiments and modelling of the experiment dynamics in which a preliminary value is set for the parameter and sensitivity analysis are carried out to determine the value of the parameter which fits the experimental data best [8]. However, the accuracy of the predicted values depends on the quality and simplicity of experimental setups, the accuracy of the numerical model code, and preliminary selected values.

2.1.1 Density

González-Montellano *et al.* [8] have reported a comprehensive methodology for measuring and predicting various material properties of olives and maize grains. They reported that density of a particle can be determined by two methods. The first method

measures the mass of individual particles directly using a precision balance and estimates the volume of individual particles, from which the density is calculated. The second method measures the density of a number of particles indirectly by measuring the volume change in a vessel, containing a known volume of liquid (e.g. water) after adding the particles to the vessel [8]. Table 2.1 shows the measured particle density for maize grains using the mentioned methods.

Table 2.1: Measured density of corn kernels in the work of González-Montellano *et al*. [8]

	Method 1	Method 2
ρ_{avg} (kg/m^3)	866.7	1163.3
Coefficient of Variation CV (%)	9.9	0.3

The results showed that the measurement of the particle density for well-defined shaped particles such as glass beads can be carried out using both methods. However, for irregularly shaped particles such as maize grains and olives, the first method may not determine the correct value for particle density due to inaccurate estimation of the volume of irregularly shaped particles. Moreover, the measurement accuracy of the second method depends on the density difference of the water and the seeds. When the density of the seeds is lower than water, the seeds float on top of water which leads to an inaccurate measurement of the density. In order to counter this issue, Geopyc Envelope Density Analyser [13] can be used which measures envelope density of a powder assembly by measuring the volume change of a fine powder assembly before and after the particle of interest is added.

2.1.2 Young's Modulus

Rigidity of a material is characterised by Young's modulus which is the relation between uniaxial stress and strain [14]. González-Montellano *et al.* [8] showed that Young's modulus of the maize grains and olives can be obtained from Eq. (2.1.1) and Eq. (2.1.2), respectively, with the use of indentation experiments with a spherical indenter.

$$E = \frac{0.338F\left(1-\upsilon^2\right)}{D^{1.5}} K_U^{1.5} \left(\frac{1}{R_U} + \frac{1}{R_U^{'}} + \frac{4}{d} \right)^{0.5} \qquad (2.1.1)$$

$$E = \frac{0.338F\left(1-\upsilon^2\right)}{D^{1.5}} K_U^{1.5}\left(\frac{4}{d}\right)^{0.5} \tag{2.1.2}$$

where F, D, d, υ, R_U and R'_U are the applied force, deformation size, size of indenter, Poisson's ratio and maximum and minimum radii of curvature of the sample at the point of contact with the tip of indenter, respectively, and K_U is a constant dependent on the minimum and maximum radii of curvature of the sample. Indentation experiments were carried out on a flat surface of seeds using a spherical indenter [8]. Due to the shape and mechanical behaviour of the corn seeds, the above equations may not determine accurate value for Young's modulus of the corn due to the distribution of stiffness across the sample. Moreover, in the experiments, the authors used a 4.8 mm spherical indenter in which the size of indenter is comparable to the curvature of the samples. This results in an inaccurate calculation of the size of imprint of the indentation. A smaller spherical indenter can be used in order to minimise the error on the calculation of the area of indentation. However, a comprehensive investigation needs to be done to fully characterise Young's modulus of corn seeds due to irregular shape and various mechanical response of the maize grain during the indentation process. According to Shelf and Mohsenin [15], the value of Young's modulus for corn seeds can vary between 166 to 6757 MPa depending on the type of corn seeds.

2.1.3 Coefficient of Restitution

According to Bedford and Fowler [16], the coefficient of restitution (e_p) of particles, when there is no rotation involved in the collision, can be obtained by measuring the velocity of particles before and after the collision. Wong *et al.* [17] reported that the value of particle-particle coefficient of restitution increases with increasing the impact velocity. However, González-Montellano *et al.* [8] found that the value of e_p decreases in the case of olives, while in the case of maize grains e_p remains constant. In the case of irregularly shaped particles, it is difficult to achieve a collision without particle rotation and therefore further investigation is required to measure coefficient of restitution of corn seeds.

2.2 Breakage and Attrition

When a force is applied to a particle, it deforms. As the force is increased, cracks may form and propagate in the particle. When a crack meets the surface of a particle at two points, it leads to the removal of a chip or fragment if the crack extends through the

body of the particle. Failure of particles can be classified into brittle, semi-brittle or ductile modes. In the brittle mode, failure is due to the existence of internal or surface flaws and deformation is elastic. In the semi-brittle mode, a degree of plastic deformation follows elastic deformation before failure through crack propagation. In the case of ductile failure, failure occurs through rupture, cutting or ploughing and deformation is plastic [18].

For a single particle, it is possible to predict the extent of breakage based on the material properties and process conditions. Ghadiri and Zhang [2] modelled material removal due to chipping in single impacts of semi-brittle particles and validated the model by experimental results. Their model describes the chipping mechanism, where the formation of subsurface lateral cracks causes the material loss from the particles. They reported that the extent of breakage of particles due to impact can be described using a dimensionless parameter, η,

$$\eta = \frac{\rho v^2 l H}{K_c^2} \tag{2.2.1}$$

where ρ, v, l, H and K_c are particle density, impact velocity, characteristic particle size, hardness and fracture toughness, respectively. The breakage propensity, η, describes the extent of breakage of particles upon the impact to a flat surface. As packing fraction increases, particles predominantly break through shear stress rather than impact [19]. Hence, there is a lack of understanding on the direct cause of breakage in process equipment and therefore DEM simulations of the system would result in better understanding of the cause of breakage.

2.2.1 Breakage under Shear Deformation

Breakage of particles in a shear band is the dominant breakage mechanism in many units of process equipment and therefore is of great industrial interest to investigate the shear breakage of particles [5,20,21]. Gwyn [21] investigated the attrition of catalysts in a fluidised bed and reported that the breakage can be described by,

$$W = K_G t^{m_G} \tag{2.2.2}$$

where W is the extent of breakage, K_G and m_G are the breakage constants and t is time. This model was developed to describe particle attrition in fluidised beds and lacks a description of the fragmentation of particles which is observed in shear cell

experiments. Paramanathan and Bridgwater [6] introduced the annular shear cell to study the breakage of particles in a shear band. They suggested that the rate of breakage can be described by an equation similar to Gwyn's equation,

$$W = k\gamma^m \tag{2.2.3}$$

where γ is the shear strain and k and m are empirical constants. Paramathan and Bridgwater [20] reported that a first order model was insufficient in describing the breakage rate and suggested that Gwyn's equation is more successful in describing the extent of attrition and it requires one less adjustable parameter. However, Gwyn's model was unsuccessful to describe the breakage as a function of applied stress. Benbow and Bridgwater [22] found that the extent of attrition of particles is proportional to shearing work where this work is proportional to the product of normal stress and strain ($\sigma\Gamma$). Potapov and Campbell [23] showed that breakage is also proportional to the product of normal stress and strain by the use of DEM simulations. Ning and Ghadiri [5] investigated the dependency of normal stress and strain with shear energy by the use of DEM simulations. It was found that attrition increases with increase of friction.

A considerable amount of energy contributes toward rearrangements of particles during shearing. This energy depends on the bed fabric which constantly changes. Based on this fact, Neil [24] proposed a new model for measuring breakage,

$$W = K_N \left[\left(\frac{\sigma}{\sigma_{SCS}} \right) \Gamma^{\varphi} \right]^{\beta} \tag{2.2.4}$$

where K_N , φ and β are breakage constants and σ_{SCS} is the side-crushing strength of material. Neil and Bridgwater [25] used this model to describe the breakage process for a wide range of materials where the size distribution of breakage products followed the Schuhmann [26] model,

$$W = W_T \left(\frac{d}{d_T} \right)^G \tag{2.2.5}$$

where d is sieve size, d_T is the largest sieve size, W_T is the breakage rate of the largest size the data is applied to and G is the distribution modulus. Due to the presence of a range of particle strength in a bed of particles, determination of a single value for

particle strength in Eq (2.2.4) is questionable. Ouwerkerk [27] developed a new model for predicting the extent of breakage where the extent of breakage can be predicted by,

$$W = K_0 \left[\left(\frac{\sigma}{\sigma_{ref}} \right)^2 \Gamma \right]^{\alpha_0} \tag{2.2.6}$$

where K_0 and α_0 are fitting constants and σ_{ref} is a reference stress which leads to the same amount of breakage for the material. Although this model showed success in Kenter's [28] work, the success of this model is not reported elsewhere in the literature. This is due to the fact that this model refers to a special case of Eq (2.2.4) where φ is equal to 0.5 and Neil and Bridgwater [25] showed that for a range of 11 materials, φ could vary between 0.26 and 1.0. Although Eq (2.2.4) suggests the breakage is as a result of fragmentation due to consideration of side-crushing strength, Ghadiri *et al.* [4] the model was more suited for abrasion rather than fragmentation since by only considering the fine products in their work the correlation was improved. [29].

Further analysis was carried out by Ning and Ghadiri [5] in order to understand the mechanism of fragmentation and chipping using DEM. They used the chipping model developed by Ghadiri and Zhang [2] and suggested that fragmentation could occur if the force acting on the particles exceeded its failure force. Although the simulation predictions followed the experimental results of Ghadiri *et al.* [4] at low strains, as strain increased the breakage was overestimated by the simulations. The authors attributed this behaviour to the removal of the fragments from the bed of particles as the fragmentation process could not be modelled accurately using DEM. In fact, this could be as a result of removal of fragments which affects the bed fabric and stress distribution.

2.2.2 Measurement of Seed Breakage

According to the United States grain grading standards, broken corn and foreign material (BCFM) is the fraction of material which passes through a 7.46 mm sieve and any foreign material that remains on top of sieve [30]. Fiscus *et al.* [31] found out that various handling processes would affect the extent of kernel damage and therefore suggested that it was very critical to measure the extent of breakage of corn kernels in order to meet the market standards. Paulsen and Hill [32] investigated the breakage

rate of exported corn seeds at origin and destination. Results revealed that the breakage of seeds occurred due to handling of the material during the transportation, which was in agreement with Fiscus *et al.* [31].

The Wisconsin Breakage Tester (WBT) and Stein Breakage Tester (SBT) are the most commonly used breakage testers in seed processing industries in order to measure the breakage of the kernels as a result of impact. The mechanism and type of damage created in these two breakage testers are different. In WBT individual seeds are impacted onto a stationary surface at very high velocity (i.e. 30 ms^{-1}), which leads to chipping or cracking of the kernels [33]. On the other hand, in SBT, damage to the seeds is caused by multiple impact of a moving blade in the sample bed at high speeds (i.e. 5 – 15 ms^{-1}) [34].

Watson and Herum [35] compared the breakage measurements in eight different breakage testing devices. Three of these devices, developed by the Cargill Grain Lab., University of Illinois and University of Wisconsin, are classified as centrifugal impact devices, where the seeds are dropped individually onto a spinning disk and are projected into a cylindrical metal wall. Missouri cracker (developed by the University of Missouri) and Ohio Impacter are other breakage testers where a centrifugal fan, driven by a motor, is enclosed in a metal housing and a vibrating feeder drops seeds onto the impeller, where the seeds experience several impacts. The sixth breakage tester, developed by US Grain Marketing Research Laboratory (USGMRL), is based on their observation that most of the breakage is caused by the impaction of seed kernels upon another kernels rather than on a metal surface. This device accelerates the seeds as they pass between rubber-covered rollers and impact them onto a bed of seeds. The last two devices (Stein Breakage Tester and the modified version) subject seed kernels to a combination of impact and abrasion. The authors concluded that Wisconsin Breakage Tester is the most reliable breakage tester as it produces a low value of coefficient of variation for repeating the experiments. They also mentioned that the WBT is the fastest among the eight tested devices.

Asota [36] studied the effect of drying on mechanical quality of soybeans. The extent of damage to the seeds after drying was investigated using a combination of compression and breakage tests. Experiments were carried out in various drying conditions, where the drying period and drying temperature were selected between 26

to 96 hours and 48° to 164°C, respectively. The breakage rate and compressive resistance of the seeds were measured using the Wisconsin Breakage Tester (WBT) and Instron Universal Testing Machine. The results revealed that by increasing the drying temperature, the compressive resistance decreased and the extent of breakage increased [36].

Dondee *et al.* [37] investigated the extent of cracking and breakage of soybeans during the drying process by a combination of near-infrared radiation and fluidised-bed drying. The visual inspection was done by inspecting a 200g sample under fluorescent light. Three different near-infrared radiation power (i.e. 4, 6 and 8 kW) were used. The results revealed that by increasing the intensity of the radiation, the cracking and breakage increased.

2.2.3 Concluding Remarks

The basis of evaluating of the extent of the breakage for powders has been reported in the literature and has shown success in several cases. However, the mechanism of seed breakage has not been investigated in the literature extensively. Therefore, it is required to investigate and understand the mechanism of seed breakage within several processing units. Moreover, in the literature, the extent of seed breakage is only investigated under impact, whereas in seed processing unit operations they often subjected to shear deformation. Therefore it is important to investigate this phenomenon using shear cell breakage testers. By assessing the breakage in a shear cell under a range of stresses and strains it is possible to establish an empirical relationship between the attrition of a given material and the prevailing stresses and strains.

The methods of characterising material properties of seeds such as Young's modulus, density and coefficient of restitution are reported in the literature. However, improvement to the existing methods is required to measure the material properties more accurately.

2.3 Distinct Element Method

Microscopic interactions between individual particles control the macroscopic behaviour of particulate materials. In order to understand this behaviour, DEM simulations can provide a wide range of information of transient forces acting on individual particles which is difficult to achieve by experiments [38]. DEM is

originated from Cundall and Strack's [39] work where slow deformation and failure of rock were modelled. In the following sections, the basics of DEM, existing contact models and simulation of shape are discussed.

2.3.1 Time-step

In particulate systems, particles displace independently from one another and interact only at contact point [39]. Not only the forces and torques originated from the contacts from neighbouring particles, also disturbance propagations from particles far away would affect the movement of a particle. Therefore, in DEM, particle displacement calculations (motion) are performed within a short time-step, where the disturbance waves cannot propagate further than the neighbouring particles [39]. After calculation of motion of particles at each time-step, the contact and body forces acting on all particles are calculated. According to Cundall and Strack [39], the time-step must be sufficiently smaller than Rayleigh time-step to avoid numerical instability within the simulations. The Rayleigh time-step can be calculated based on the physical and mechanical properties of the particles within the system [40].

$$T_R = \frac{\pi R \left(\frac{\rho}{G} \right)^{0.5}}{0.1631\upsilon + 0.8766} \tag{2.3.1}$$

where R, ρ, G and υ are radius, density, shear modulus and Poisson's ratio of the particles, respectively. For a particulate system consisting of different particle types and sizes, the critical time step should be the smallest among the particles due to variation of time step with respect to presence of different particles [5].

2.3.2 Motion Calculations

Particles within a granular flow can have translational and rotational motion. Newton's second law of motion can be used to calculate the accelerations for each motion. Therefore, integration of acceleration over the time-step gives particle velocities and consequently position of particles can be calculated. The rotational and translational motions are calculated from the following equations,

$$I \frac{d\omega}{dt} = M \tag{2.3.2}$$

$$m \frac{dV}{dt} = F_g + F_c + F_{nc} \tag{2.3.3}$$

where I is the moment of inertia, ω is the angular velocity, M is the resultant contact torque acting on the particle by surrounding particles or walls, V is the translational velocity of the particle, m is the mass of the particle, F_g is the resultant gravitational force acting on the particle and F_c and F_{nc} are the resultant contact and non-contact forces between the particle and surrounding particles or walls. The schematic representation of the above forces is presented in Figure 2.1.

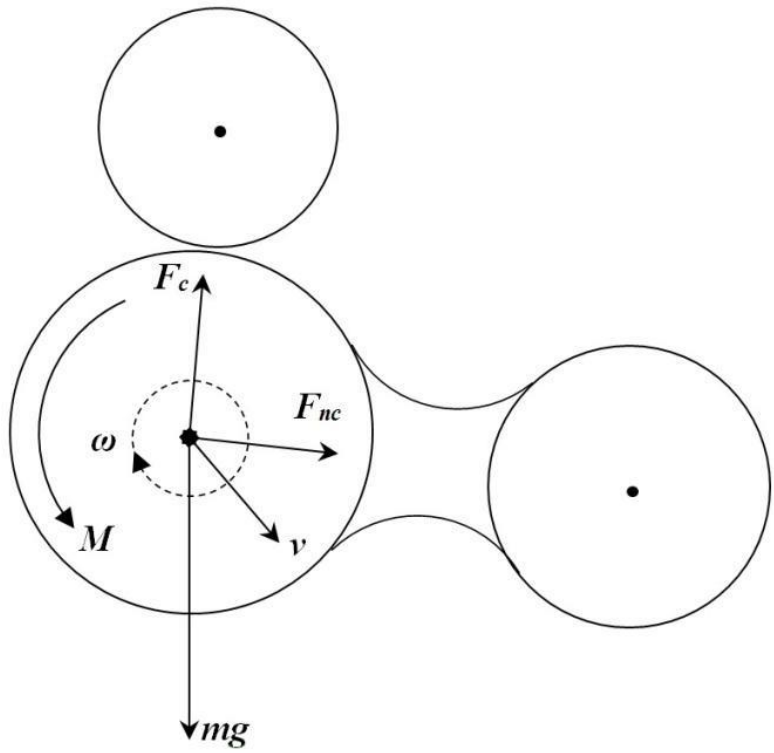

Figure 2.1: Schematic representation of forces acting on a particle.

2.3.3 Contact Force Models

A number of contact force models exist in the literature which allows the particles to overlap to represent deformation. According to Ketterhagen *et al.* [41], an overlap between particles can be used in order to model particles deformation and it is typically in the range of 0.1 – 1.0 percent of the particle size. In a particulate system, the resultant contact force acting on a particle, which is the vectorial sum of the contact forces, can be calculated by applying contact force models at each contact of any particle [38]. Linear spring contact model [39], Hertzian normal contact model and Mindlin no slip tangential contact model [42] are the most commonly used normal and tangential contact forces in the literature. A brief review of these contact models is discussed in the following section.

2.3.3.1 Linear Spring Contact Model

This model was first introduced by Cundall and Strack [39] where the deformation is treated as a linear spring. The contact force between two perfectly elastic spheres is resolved into normal and shear components with respect to contact plane. Therefore,

$$F = \vec{F}_n + \vec{F}_s \tag{2.3.4}$$

where F is the contact force, F_n is the normal and F_s is the shear component of the contact force. From the overlap of the particles in contact, the normal contact force is calculated,

$$F_n = k_n \alpha_n \tag{2.3.5}$$

where α_n is the normal overlap and k_n is the normal stiffness at the contact which can be calculated from Equation (2.3.6),

$$k_n = \frac{k_n^1 k_n^2}{k_n^1 + k_n^2} \tag{2.3.6}$$

where k_n^1 are k_n^2 the normal stiffness values for the particles in contact. Moreover, the increment of shear force in this model is calculated from,

$$\Delta F_s = -k_s \Delta \alpha_s \tag{2.3.7}$$

where $\Delta\alpha_s$ is the increment of shear displacement of the particles in contact and k_s is the shear contact stiffness which can be calculated as follows,

$$k_s = \frac{k_s^1 k_s^2}{k_s^1 + k_s^2} \tag{2.3.8}$$

where k_s^1 and k_s^2 are the shear stiffnesses for the particles in contact. Total shear force is calculated using,

$$F_s = F_{s_\mathrm{pre}} + \Delta \mathrm{F_s} \tag{2.3.9}$$

where F_{s_pre} is the previous shear force which accounts for the force from any rotations [43].

2.3.3.2 Hertzian Normal Contact Model

In Hertzian normal contact model, the normal contact force between two perfectly-elastic spheres in contact is given by [44],

$$F_n = \frac{4}{3} E^* R^{*\frac{1}{2}} \alpha^{\frac{3}{2}} \tag{2.3.10}$$

where E^* and R^* are the reduced Young's modulus and the reduced radius, which are given by Eqs (2.3.11) and (2.3.12), respectively, and α is the normal overlap.

$$E^* = \left(\frac{1-\upsilon_1^2}{E_1} + \frac{1-\upsilon_2^2}{E_2} \right) \tag{2.3.11}$$

where E_1 and E_2 are the Young's moduli of the particles in contact and υ_1 and υ_2 are Poisson's ratio of the particles in contact.

$$R^* = \left(\frac{1}{R_1} + \frac{1}{R_2} \right)^{-1} \tag{2.3.12}$$

where R_1 and R_2 are the radii of the particles in contact.

2.3.3.3 Mindlin No Slip Tangential Contact Model

According to DEM Solutions [40], the tangential contact force of two elastic spheres can be modelled based on,

$$F_s = -k_s \alpha_s \tag{2.3.13}$$

$$k_s = 8 G^* R^{*\frac{1}{2}} \alpha^{\frac{1}{2}} \tag{2.3.14}$$

$$G^* = \left(\frac{1-\upsilon_1}{G_1} + \frac{1-\upsilon_2}{G_2} \right)^{-1} \tag{2.3.15}$$

where α_s is the tangential overlap, k_s is the tangential stiffness, R^* is the equivalent radius, G^* is the equivalent shear modulus, G_1 and G_2 are the values of the shear moduli of the particles in contact. Although this model considers tangential displacement with no slip, Mindlin and Deresiewicz [45] investigated the presence of tangential slip in the model. They found that the force-displacement relation depends on the loading history and instantaneous rate of change in the normal and tangential forces. Due to

accurate evaluation of tangential displacement and contact force, this model is very complex which makes it computationally expensive for DEM codes [42].

2.3.4 Particle Shape

In general, friction forces between individual particles prevent spherical particles from rotating. However, in the case of irregularly shaped particles, rotation is not only affected by friction but also by mechanical interlocking. According to Favier et al. [46] for spherical particles only tangential forces lead to the rotation of particles, whereas for irregularly shaped particles, rotation can be as a result of both normal and tangential contact forces. It has been shown in the literature that irregularly shaped particles tend to have a larger angle of repose [47] and increased bulk shear strength [48]. According to Cleary [49], spherical particles may differ from irregularly shaped particle in shearing strength, dilation during shearing, voidage distribution and partitioning of energy between linear and rotational modes. The author reported that irregularly shaped particles show resistance to shear forces due to interlocking [49].

There are a number of approaches through which the shape of irregularly shaped particles can be taken into account in DEM. Below is a review of most commonly used approaches for simulating particle shape with DEM.

2.3.4.1 Introduction of Rolling Friction

In simulating particulate systems, spherical shaped particles are preferred due to the simplicity of contact detection, where the contact can be detected if the distance between two particles becomes less than the sum of their radii. This would result in efficient and accurate detection of contact and therefore leads to fast and accurate calculation of contact forces. Based on this advantage, Morgan [50] proposed a new method for simulating mechanical interlocking of irregularly shaped particles by restricting spherical particles rolling. This method showed that application of rolling friction would lead to more realistic values of assemblage friction compared to free rolling spheres. In a recent review of rolling friction, Ai *et al.* [51] classified the rolling resistance models into four categories which are detailed in the following sections.

2.3.4.1.1 Directional Constant Torque Models

In these models, a constant resistive torque is applied which is proportional to the normal contact force and it is in opposite direction to the rolling direction. In a 2D case, the resistive torque between two particles in contact can be calculated by,

$$M_r = -\mu_r R_r F_n \left(\frac{\omega_{ref}}{|\omega_{rel}|} \right) \tag{2.3.16}$$

$$\omega_{rel} = \omega_i - \omega_j \tag{2.3.17}$$

$$R_r = \frac{r_i r_j}{r_i + r_j} \tag{2.3.18}$$

where μ_r is coefficient of rolling friction, F_n magnitude of the normal contact force, R_r and ω_{rel} are effective rolling radius and relative angular velocity of two particles in-contact which can be calculated based on equations (2.3.18) and (2.3.17), respectively. A typical example of this type of models is the work of Zhou *et. al.* [52], where formation of sand pile is modelled by introducing rolling friction to spherical particles in a three-dimensional simulation of generation of a stable heap of spheres. They reported that the angle of repose increased with rolling friction coefficient and decreased with particle size. The authors also reported that implementation of rolling friction in the simulation led to better agreement between simulation and experimental results. This suggests that rolling friction will play an important role within the DEM simulations.

2.3.4.1.2 Viscous Models

In viscous models, the applied resistive torque is not only proportional to normal contact force, but also to relative angular or translational velocity of two particles, and it can be calculated based on the following equation,

$$M_r = -\mu_r R_r F_n \left(\omega_i r_i - \omega_j r_j \right) \tag{2.3.19}$$

where $\omega_i r_i - \omega_j r_j$ is representative of relative translational velocity due to rolling of two particles at the contact. A typical example of this type of model is the work of Zhou *et. al.* [52], which is explained in Section 2.3.4.1.1 in detail.

2.3.4.1.3 Elastic-plastic Spring-dashpot Models

The total resistive torque in these models consists of two components of spring torque and viscous damping torque, where the spring torque depends on relative rotation between the two particles in contact.

$$M_r = M_r^k + M_r^d \tag{2.3.20}$$

where M_r^k and M_r^d are spring and viscous damping torques, respectively. The spring torque part of this model is defined incrementally by,

$$M_{r,t+\Delta t}^{k} = \begin{cases} M_{r,t}^{k} - k_r \omega_{rel} \Delta t & if \quad \left| M_{r,t+\Delta t}^{k} \right| < \mu_r R_r F_n \\ \mu_r R_r F_n \dfrac{M_{r,t}^{k} - k_r \omega_{rel} \Delta t}{\left| M_{r,t}^{k} - k_r \omega_{rel} \Delta t \right|} & otherwise. \end{cases} \tag{2.3.21}$$

where $M_{r,t}^k$ is spring torque at time t and k_r is rolling friction which can be calculated from,

$$k_r = 2 J_n R_r F_n \tag{2.3.22}$$

where J_n is a dimensionless coefficient which varies from 0.25 to 0.5 theoretically [51]. On the other hand, the viscous torque part of this model can be defined in the form of,

$$M_{r,t+\Delta t}^{d} = \begin{cases} -C_r \omega_{rel} \Delta t & if \quad \left| M_{r,t+\Delta t}^{d} \right| < \mu_r R_r F_n \\ -f C_r \omega_{rel} \Delta t & if \quad \left| M_{d,t+\Delta t}^{d} \right| = \mu_r R_r F_n \end{cases} \tag{2.3.23}$$

where C_r is damping constant and f is a constant, where it is set to zero if the viscous damping torque is only active before the contact rolling torque fully mobilises and is set to one if the viscous damping component is always present to simulate any physical viscous dissipative interaction that may exist between the particles [51]. According to Ai *et. al.* [51], rolling viscous coefficient can also be calculated from,

$$C_r = \eta_r C_r^{crit} \tag{2.3.24}$$

$$C_c^{crit} = 2\sqrt{I_r k_r} \tag{2.3.25}$$

$$I_r = 1 \Bigg/ \left(\frac{1}{I_i + m_i r_i^2} + \frac{1}{I_j + m_j r_j^2} \right) \tag{2.3.26}$$

where η_r is the rolling viscous damping ratio, C_r^{crit} is the rolling critical viscous damping constant, I_r is the equivalent moment of inertia for relative rotational vibration at the contact point, I_i , I_j , m_i and m_j are the moment of inertia with respect to centre of the two particles and mass of the two particles, respectively.

Iwashita and Oda [53] took advantage of this type of model to simulate microstructure of shear bands. The authors reported that the relative movement of particles at the contact can be divided into sliding and rolling components. The rolling component would lead to relative rotation of two in-contact particles, which conserves law of angular momentum. Moreover, they reported that generation of not only large voids in a shear band but also gradient of particle rotation along the shear band boundaries is only possible by implementing rolling resistance in DEM simulations.

2.3.4.1.4 Contact-independent Models

In this model, the rolling resistance torque is dependent on total rotational velocity of the particle rather than the relative rotational velocity of the two in-contact particles. As these models may lead to different resistive torques being applied to two contacting particles, they may violate the equilibrium state of the system and therefore it is not recommended for the use in DEM [51].

Although the implementation of rolling resistance models has been used widely in the literature for representation of shape of particles, Wensrich and Katterfeld [54] reported that consideration of only rolling would not lead to representation of shape of particles in the case of angle of repose. In their work, the angle of repose simulations were carried out by using spherical spheres with rolling friction and clumped spheres. They reported that some similarities were observed but in most cases the results were not in agreement. They attributed this to the fact that the rolling friction only acted to oppose the rolling motion, whereas the shape would not only act as rolling resistance but it also could cause of rolling.

2.3.4.2 Clumped Spheres

In this method, particle shape is approximated by a number of overlapping or touching spheres with potentially different sizes. The spheres are fixed in position relative to each other. The advantage of this method is that it provides an approximation of the actual irregularity while maintaining computational contact detection efficiency and the contact law of spheres. It must be noted that this advantage comes at the expense of increased total number of spheres and usually reduced particle size, which increases the computational complexity of the simulations [55]. Theoretically, any particle shape can be modelled, however highly angular particles require a large number of small spheres to approximate their sharp edges, which makes this method unsuitable

for these sort of shapes [46]. Approximation of shapes with this technique mostly produces inadvertent surface roughness for the modelled particles [41]. The induced roughness can be controlled by increasing the number of spheres, while the computations are kept within a reasonable range of complexity.

Kodam *et al.* [56] investigated the influence of the forces generated by each component sphere using a simple case in which a particle collides with a flat wall. It was shown that when multiple component spheres contact the wall, the component sphere contact stiffness should not be the same as the master sphere's contact stiffness. If the same contact stiffness is used in the clumped-sphere model, then the contact becomes effectively stiffer. The optimal values of the component sphere contact stiffness depends upon the number of component spheres contacting the wall or other particles simultaneously and on the degree of overlap for each component sphere contact. Kruggel-Emden *et al.* [57] showed that the results for the multi-sphere method strongly depended on the alignment of the particles. These studies demonstrate that great care must be taken when using the clumped-spheres approach to modelling non-spherical particles in DEM simulations.

Favier *et al.* [46] used this method to model discharge of ellipse-shaped particles through an orifice in a flat-bottomed hopper and the results were also compared to similar simulations where the particles were represented by spheres They reported a good agreement between simulations of ellipse-shaped particles and physical flows for the rate of discharge and the vertical velocity profiles. The spherical particles also had a good agreement with simulated and experimental results of ellipse-shaped particles in frequency of arch formation, for a given particle mean diameter, and orifice diameter.

2.3.5 DEM Simulation of Seed Processing

Wiącek *et al.* [7] investigated the influence of the grain shape and inter-particle friction of pea and bean grains on mechanical response of the granular assemblies in a uniaxial compression test. The investigation was carried out comparing the DEM simulations and experimental results. In simulations, spherical and non-spherical particles with different aspect ratios (ratio of the longest to the smallest particle dimensions) were used. For the latter, spheres were clumped together to form the non-spherical particle shapes. The results showed that the mechanical response of the granules was highly

affected by increasing the aspect ratio of the particles, the lateral-to-vertical pressure decreased as the particle aspect ratio was increased. However once the aspect ratio of the particles exceeded 1.6, the lateral-to-vertical pressure became relatively invariant [7]. Moreover, the authors have reported that the DEM simulations have predicted the value of effective bulk elastic modulus close to those obtained in experiments for spherical particles (i.e. peas). However, in the case of oblong particles (i.e. beans), simulations results did not agree with experimental results [7]. Figure 2.2 shows the comparison of the measured effective elastic modulus as function of average vertical pressure for spherical and non-spherical particles.

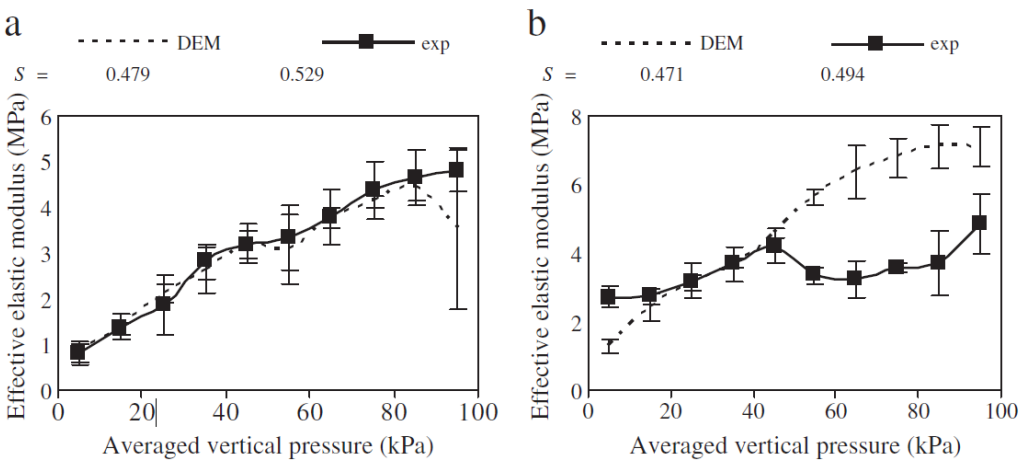

Figure 2.2: Effective elastic modulus as a function of vertical lid pressure for pea (a) and bean (b) obtained from numerical simulations and experiments [7]**.**

It is clear that shape of particles affects the simulation results and a systematic study is required to understand and develop a suitable model to tackle these issues.

González-Montellano *et al.* [8,58] investigated the discharge flow of glass beads and corn grains in silos using DEM, where the glass beads and corn seeds were simulated using spherical and clumped spherical particles, respectively. Their predictions for mean bulk density for filling phase, discharge time and flow patterns were then compared to the experimental results. Due to the shape and difficulty of measuring the friction of irregularly shaped particles, the flow pattern and discharge time in the simulations did not follow those obtained in experiments. Therefore, the value of particle-particle friction coefficient was calibrated using sensitivity analysis based on Balevicius *et al.* [59] approach. An increase in friction coefficient decreased the discharge rate and bulk density value only at the end of the silo filling phase. Figure

2.3 shows the comparison of the various calibration simulations by altering the coefficient of friction with those observed in experiments.

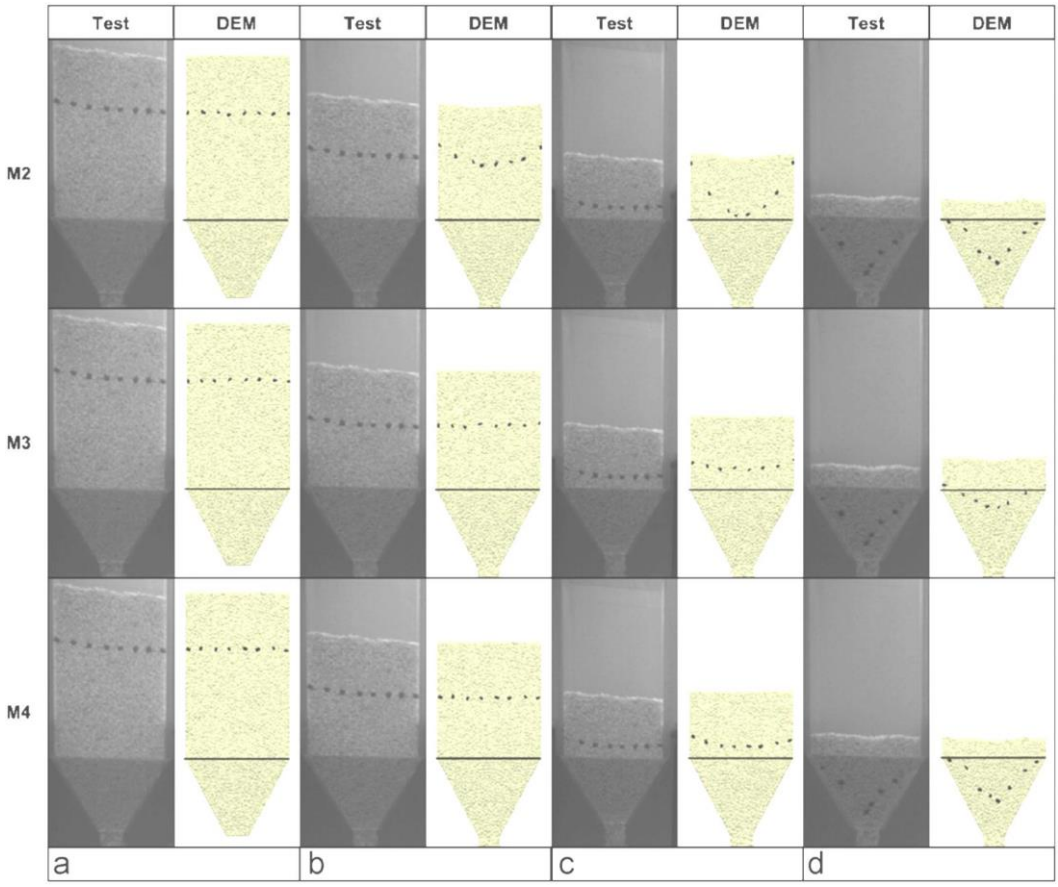

Figure 2.3: Effect of calibrating particle-particle friction on flow patterns compared to the experiments for maize grains: (a) t=0T, (b) t=0.25T, (c) t=0.5T and (d) t=0.75T [58]**.**

It is clear that for modelling of irregularly shaped particles, calibration would play an important role for achieving reliable results.

Recently, González-Montellano *et al.* [60] investigated the vertical and horizontal distribution of the normal pressure, tangential stresses, mobilised friction and velocity profiles for filling and emptying the silos using experiments and DEM. They reported that the numerical simulations were in agreement with experiments. However, the predicted horizontal distribution of normal stress was greater for the central positions on the walls compared to the experimental results. The authors suggested that, by using hybrid models similar to the work of Lu *et al.* [61], where FEM and DEM were coupled, the predicted results would improve.

Effective separation and size classification of seeds using screening process has always been a challenge in seed processing industries. Li *et al.* [62] investigated the effect of particle bed height to find the optimum bed height during the screening process. The dynamics of the process was developed using a two dimensional DEM model. In the simulations, the authors used two common crop seeds, soybeans and mustard seeds, and investigated the screening rate and the required screen length as a function of feed rate [62]. They reported that as the bed height increased (i.e. increasing the feed rate), the efficiency of the separation decreased and small particles could not segregate towards the mesh screens.

2.4 Application of DEM to Seed Coating

Controlling inter-particle coating variability is crucial for functional particle coating. In seed processing, seeds are commonly coated with a protective layer consisting of fertilisers and pesticides. The protective layer controls the release and availability of fertilisers and pesticides. Variations from the required amount of coating, e.g. coating thickness and mass, can adversely impact the effectiveness of the product.

Inter- and intra-particle coating variability are the two parameters for assessing the coating variability. The former is the variation in the average coating mass from a granule to another, whilst the latter is the distribution of coating liquid on the surface of individual granules, in which both factors can be quantified using the coefficient of variation [63]. Inter-particle coating variability can be defined as the coefficient of variation of the coating mass between particles [63],

$$CoV_{\text{inter}} = \frac{\sigma}{\bar{m}} \tag{2.4.1}$$

where standard deviation, σ, and average coating mass, $\bar{m}$, can be calculated using,

$$\bar{m} = \frac{1}{N}\sum_{i=1}^{N} m_i \tag{2.4.2}$$

$$\sigma = \sqrt{\frac{1}{N}\sum_{i=1}^{N}\left(m_i - \bar{m}\right)^2} \tag{2.4.3}$$

where m_i is the coating mass on the ith seed and N corresponds to the total number of particles in the system.

In pharmaceutical industries, horizontal drum coaters are commonly used for coating tablets with a thin layer of coating film. In this type of coater, a large number of tablets are placed inside the drum and the drum is rotated along its axis. The rotational motion of the drum leads to radial and slight axial mixing of the tablets [64]. The coating film is formed by spraying a liquid onto the moving tablet bed. Mixing and uniformity of coating is enhanced by placing a number of baffles inside the drum. This type of coater is similar to that used for coating of seeds with two main differences: i) in seed coating the drum is placed vertically instead of horizontally and motion is brought about by a rotating base; ii) a rotating disc atomiser is used instead of nozzle sprayers. The behaviour of a bed of particles in horizontal rotating drums have been well investigated in the literature [64–69] where it was found that drum filling level and Froude number , $Fr \equiv \omega^2 R/g$ where ω and R are the rotational speed and radii of the drum and g is the gravitational acceleration, influence the particle flow. Mellmann [70] identified seven different bed behaviours in horizontal drum mixers/coaters (as shown in Table 2.2): slipping, surging, slumping, rolling, cascading, cataracting, and centrifuging.

Table 2.2: Behaviour of a bed of particles in a horizontal drum mixer [70]

Basic form	Slipping motion		Cascading ("tumbling") motion			Cataracting motion	
Subtype	Sliding	Surging	Slumping	Rolling	Cascading	Cataracting	Centrifuging
Schematic							
Physical process	Slipping		Mixing			Crushing	Centrifuging
Froude Number Fr [–]	$0 < Fr < 10^{-4}$		$10^{-5} < Fr < 10^{-3}$	$10^{-4} < Fr < 10^{-2}$	$10^{-3} < Fr < 10^{-1}$	$0.1 < Fr < 1$	$Fr \geq 1$
Filling degree f [–]	$f < 0.1$	$f > 0.1$	$f < 0.1$	$f > 0.1$		$f > 0.2$	
Wall friction μ_W[–]	$\mu_W < \mu_{W,c}$	$\mu_W \geq \mu_{W,c}$	$\mu_W > \mu_{W,c}$			$\mu_W > \mu_{W,c}$	
Application	No use		Rotary Kilns and reactors; rotary dryers and coolers; mixing drums			Ball mills	No use

In addition to Froude number and filling level, the behaviour of the bed in horizontal drum coaters also depends on the friction coefficient between the wall and particles [71]. It has been reported in the literature that parameters such as particles stiffness, density and coefficient of restitution do not have any significant effect on behaviour

of the bed [67,72–74]. However, it has been shown that in applications such as fluidisation, where cohesion is present in the system, varying stiffness of particles in DEM affects the flow of particles [75,76].

The tablet residence time per pass on the free surface of a bed in horizontal pan coaters have been widely investigated in the literature [65,66,68,77–79]. Pandey and Turton [78] investigated the effect of particle shape on the movement of particles in a pan coating device by placing a CCD camera in the position of the sprayer. The circulation time, surface time, projected area of particle per pass, dynamic angle of repose, cascading velocity and dispersion coefficient of a tracer particle in the coater were measured. They reported average circulation time of the tracer increases with increasing the fill level in the coater (fill level varied from 12.5% to 25%) and decreases with increasing the rotational speed of the pan, as shown in Figure 2.4A. The former is due to the fact that by increasing the fill level, there are a larger number of particles in the system and the probability of a particle being present in the spray zone is decreasing. The time that the particles spent in the spray zone was also analysed, where the particles residence time on the surface of the bed was decreased by increasing the rotational speed of the pan, as shown in Figure 2.4B. Moreover, Pandey and Turton [78] also investigated the dispersion coefficient, D_x, along the axis of the pan. The dispersion coefficient was increased with increasing the rotational speed of the pan, indicating more axial movement of particles by increasing the pan rotational speed.

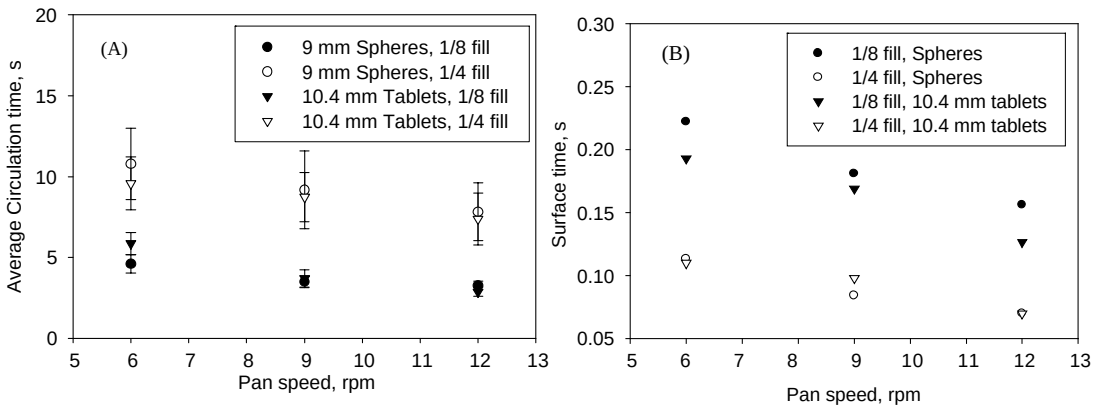

Figure 2.4: (A) Average circulation time and (B) average surface time as function of rotational speed of the pan, where the error bars represent 95% confidence interval [78]**.**

Pandey *et al.* [79] investigated particle motion in a pan coating device using both experiments and DEM simulations. The dynamic angle of repose was increased with increasing the pan rotational speed and fill level. The average cascading velocity, V_y, was found to increase linearly with rotational speed of the pan. The measured average cascading velocity in experiments was found to be slightly higher than those calculated from simulations. The authors attributed the 'wavy' shape of the cascading layer to the slight variation between the experimental and simulation results. The velocity profiles of the cascading layer was found to be more symmetric by increasing the fill level and the maximum velocity of particles were found to be close to the midpoint of the cascading layer.

Suzzi *et al.* [80] investigated the effect of tablet shape, as shown in Figure 2.6, and fill level on inter-tablet coating variability in a continuous rotating drum coater. Similar to the work done by Brone and Muzzio [81], for a double cone blender, the mixing constant k is used for quantifying the mixing efficiency, defined as relative standard deviation (RSD), in the coater,

$$RSD^2 = RSD_r^2 + e^{-kN} \tag{2.4.4}$$

where N is the number of revolution of the coater, RSD_r is the relative standard deviation of a random mixture, defined for a certain composition of particles and a given sample size as the minimum theoretical value of relative standard deviation that can be achieved by random mixing. The theoretical relative standard deviation of a random mixture can be calculated using,

$$RSD_r = \frac{\sigma_r}{\overline{W}} \tag{2.4.5}$$

$$\sigma_r = \sqrt{\frac{p(1-p)}{M}} \tag{2.4.6}$$

where p is the mass fraction of one component in the mixture and M is the total number of particles in the sample [82]. Suzzi *et al.* [80] reported that mixing efficiency for all investigated tablet shapes was decreased with increasing the fill ratio of the coating chamber, as shown in Figure 2.7. Moreover, they concluded that the dispersive mixing of the bi-convex tables was faster than oval shape tablets. A significantly better performance was achieved at lowest fill ratio in the case of rounded tablets. However,

the mixing quality was drastically decreased with increasing the fill ratio. It has to be noted that the mixing constant, *k*, only quantifies the radial diffusive mixing and does not shed lights on the recirculation behaviour of the tablets under the spray zone. The inter-tablet coating uniformity was investigated by a first order approximation, where the back-splashing of satellite droplets and the transfer of coating solution from a tablet to neighbouring tablets were neglected. Based on this approximation, the inter-tablet standard deviation was directly correlated to the relative standard deviation of residence time of tablets in the coating zone. Suzzi *et al.* [80] assumed a certain coating efficiency, ζ, of the impacting spray droplets, the coating mass ratio remaining and impinging on the tablet, and $\dot{m}_{spray}$ the impinging mass on a tablet per second in order to quantify the coating performance in a continuous coater. Therefore, the average coating mass on a tablet after *N* number of pan revolutions can be calculated using,

$$m_{coat}\left(N\right) = f_R \frac{2\pi}{\omega} N \zeta \dot{m}_{spray} \tag{2.4.7}$$

Suzzi *et al.* [80] concluded that average fractional residence time, for the investigated tablet shapes, was decreased with increasing the fill ratio, leading to slower coating speed. However, the bi-convex shaped tablets seemed to be less affected by fill ratio. They also reported that relative standard deviation of fractional residence time of tablets was increased with increasing the fill ratio.

Kalbag and Wassgren [63] investigated inter-tablet coating variability and tablet residence times within the spray zone in a horizontal coating pan using a periodic random coating model. In their model the uniformity of tablet coating at a given processing time, *t*, is given by,

$$CoV\left(t\right) = \sqrt{\frac{\Delta t_{seg}}{t}\left(\frac{1}{n/N} - 1\right)} \tag{2.4.8}$$

where Δt_{seg} is the time the tablets in the spray zone remain in a quasi-segregated state, *n* number of tablets being coated per coating trial and the total number of tablets in the system is *N*. The quantity of Δt_{seg} depends on the pan, tablet and spraying mechanism as well as operational conditions, hence a series of experiments or DEM simulation are required to calculate this quantity. The authors reported that the coefficient of variation of tablet residence time followed a power law relation with coating time,

where it was decreased by increasing the coating time. For a randomly mixed tablet batch, the coating variability was shown to be inversely proportional to the square root of the number of coating trials. The DEM simulations showed that tablets in the spray zone remain in a quasi-segregated state from those located outside the spray zone for a time period, known as Δt_{seg}. They showed that Δt_{seg} was decreased with increasing the Froude number of the pan, the aspect ratio of the spray zone, and tablet-tablet and tablet-pan friction coefficients. This leads to a more uniform residence time and consequently coating mass on the tablets.

Li *et al.* [83] investigated the effect of particle size distribution on coating uniformity and segregation in an industrial paddle coater using DEM and spray post-processing analysis. DEM was used to analyse the segregation and position of particles in the system and a spray post-processing algorithm was used to analyse the coating growth as the particles arrive in the coating zone. The coating mass a particle gains during its *k*th visit to the spray zone was calculated using,

$$\Delta m_{Y,k} = R_y A_{tot} \eta_k t_{S,k} \tag{2.4.9}$$

where R_y, A_{tot}, η_k and $t_{S,k}$ are the constant spray flux density, unobscured projected surface area, average exposed area percentage and spray zone residence time during the *k*th visit to the spray zone. The overall coating mass for an individual particle after *N* number of visits to the spray zone was then calculated using,

$$\Delta m_Y = R_Y A_{tot} \sum_{k=1}^{N} \left(\eta_k t_{S,k} \right) \tag{2.4.10}$$

The authors reported that for poly-disperse particles, smaller particles tend to have a relatively high frequency of spray zone visit and low shielding by surrounding particles, resulting in a spray preference toward smaller particles in the system.

Sandadi *et al.* [68] developed a digital imaging system to analyse the circulation time (τ_{circ}), surface exposure time (τ_{surf}) and surface area of tablet projected toward the spray nozzle (A_{tab}) during each pass through the spray zone in a horizontal rotating pan coater. A range of drum rotational speeds (6 – 12 rpm), drum fill levels (1/8 and 1/4) and tablet sizes (6.3, 7.9 and 10.4 mm) were investigated. The average circulation time was decreased with increasing the drum rotation speed for both drum fill ratios and a similar trend was found for the systems where baffles were present. Larger

tablets were found to have lower circulation time compared to smaller tablets. The authors attributed this to the fact that there were fewer tablets in the system (for the same fill ratio compared to the smaller tablets), hence larger tablets were seen in the coating zone more often. It was also found that the drum fill ratio significantly affected the circulation time of tablets, where a higher circulation time was observed for larger drum fill ratios. The existence of baffles in the system however was found to have an insignificant effect on the circulation time of tablets as shown in Figure 2.5. The average surface time and projected surface area were found to decrease with increasing drum rotation and loading rate.

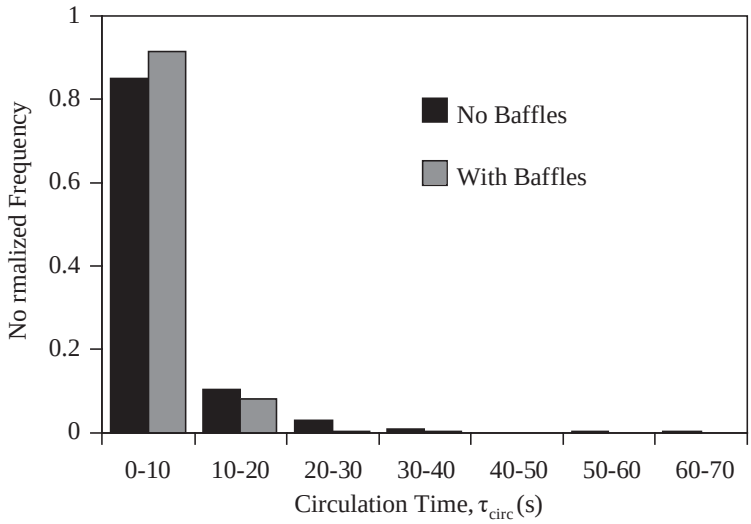

Figure 2.5: Effect of existence of baffles on tablets circulation time in horizontal rotating drum coater [68]**.**

Recently, Just *et al.* [84] looked at optimising the inter-tablet coating uniformity in a pan coater for an active coating process by varying various process parameters, such as pan load and speed, spray rate, number of spray nozzles and spraying time, using an approach based on statistical design of experiments. The experiments were carried out using a lab and pilot scaled pan coaters. They reported that a low spray rate and high pan rotational speed improved the coating uniformity in both scales. The most influential parameter affecting the uniformity of coating was found to be the number of nozzles used in the system, where a significant improvement was found by using four spray nozzles as compared to two. The coating uniformity of the tablets was also improved with increasing the coating time. The authors reported that it was possible to achieve the desired uniformity of coating by optimising the pan load, pan speed, spray rate and number of spray nozzles while maintaining the spray time.

There are a number of coating models [69,79,83,85] available in the literature for predicting the uniformity of coating of particles using DEM. However, three of these models fits well for the purpose of this work which are discussed in the following sections.

2.4.1.1 Enhanced Spray Zone Approach

This model has originally been developed by Toschkoff *et al.* [69], where a geometric region (static spray zone) is defined in the system in which the particles receive a coating mass as they pass through. At each time step, the coating residence time of a particles is increased if the particle is detected to be inside the static spray zone. In a realistic spraying process, only the top layer of particles inside the spray zone receives coating. In the systems where the bed top is stationary, a static spray zone can be defined around the top part of the bed (i.e. only the upper layer of particles in the zone). In drum coaters however, the bed top is not stationary and therefore Toschkoff *et al.* [69] proposed a two component model, spray zone detection and top detection, where the particles located on top of the bed can also be detected.

2.4.1.1.1 Spray Zone Detection

The geometry of the spray zone is represented by a cylindrical zone with an elliptical cross section [69]. The schematic diagram of the spray zone is shown in Figure 2.6.

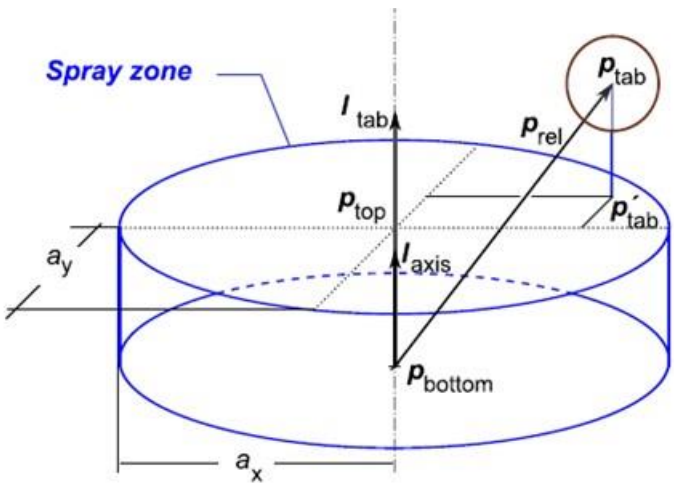

Figure 2.6: Schematic diagram of the spray zone in horizontal drum coaters [69]**.**

The position, orientation and size of the zone are defined by the centre points of the bottom and top faces of the cylinder (p_{bottom} and p_{top}, respectively) and major and minor ellipse axes normal to the cylinder axis. At each time step, a check is performed for

each particle to determine if it is located within the zone axially and inside the mantle. The relative axial position of a particle can be obtained by projecting the particle position onto the axis vector,

$$l_{tab} = p_{rel} \cdot l_{axis} = |p_{rel}||l_{axis}|\cos(\alpha) = |p_{rel}|\cos(\alpha) \tag{2.4.11}$$

$$p_{rel} = p_{tab} - p_{bottom} \tag{2.4.12}$$

where p_{rel} and α are the vector from the bottom face to the particle centre and the angle between p_{rel} and l_{axis} vectors, respectively. If l_{tab} is between zero and cylinder height, the tablet is considered to be axially inside the spray zone and for l_{tab} larger than cylinder height or lower than zero, the tablet is considered to be positioned above the op or below the bottom face of spray zone, respectively. The position of the tablet is then checked to find out if it is located inside the cylinder's mantle,

$$p'_{tab,i} = \frac{p_{tab} \cdot a_i}{|a_i|}, \qquad i = x, y \tag{2.4.13}$$

$$\frac{{p'_{tab,x}}^2}{|a_x|^2} + \frac{{p'_{tab,y}}^2}{|a_y|^2} < 1 \tag{2.4.14}$$

If Eq. (2.4.14) holds true, the tablet is considered to be inside the spray zone mantle and therefore the residence time of the particle in the spray zone is increased by the length of the simulation time step. Although, this model detects the particles in the spray zone, there may be a number of layers present in the spray zone and this leads to over estimating the coating, since only the particles on the top layer can receive the coating in reality. This model also does not consider the amount of coating being transferred from one particle to another due to collision and sliding. Moreover, the amount of coating being transferred to the particles as function of residence time in the spray zone is mainly based on the empirically established equations, hence this method is empirical rather than predictive.

2.4.1.1.2 Top Detection

Toschkoff *et al.* [69] proposed a new algorithm, top detection, in addition to the spray zone detection model that detects the top most particles in the spray zone. This is required since only particles on top of a bed receive coating. A static plane parallel to top of the particle bed is defined for the detection as shown in Figure 2.7. The static

plane is then divided into a regular grid with a grid spacing of Δ_g in both x and y directions.

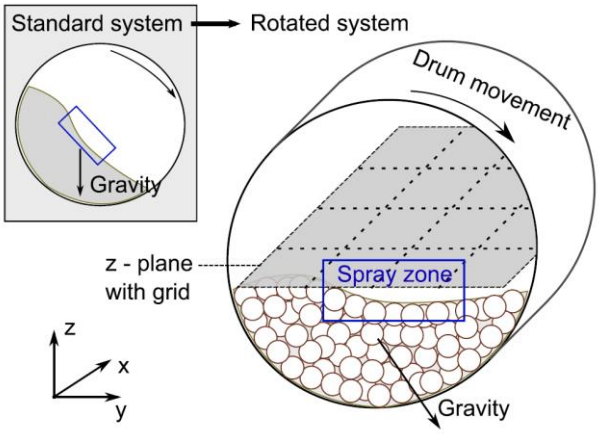

Figure 2.7: Schematic of the top detection by introducing a discretised static plane [69]

At each time step, the position of particles in each grid is checked and the top most particle is considered to be on the top of the bed. The accuracy of the selected of top layer particles mainly depends on the grid spacing, Δ_g, where a wide or narrow grid spacing leads to under or over estimation of the number of particles on the surface of the bed, respectively, as shown in Figure 2.8.

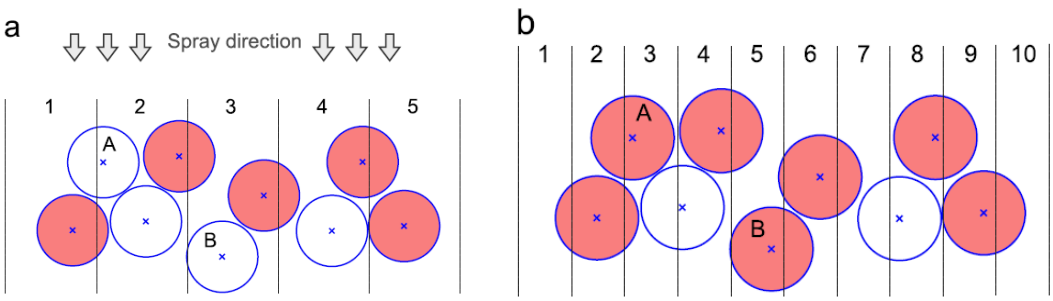

Figure 2.8: Influence of the grid spacing on detection of particles on top of particle bed for (a) wide and (b) narrow spacing. The filled circles represent the particles being detected by top detection algorithm.

The detection accuracy of the top layer using this method is mainly dependent on the grid spacing and the optimum spacing has to be calibrated. Toschkoff *et al.* [69] suggested the optimum grid spacing is similar to the diameter of particles however for non-spherical particles it is difficult to determine only one optimum value of grid spacing and it is more likely the algorithm fails to detect all the particles on the surface

of the bed accurately. For determination of optimum grid spacing, the results have to be compared to those measured experimentally, hence this method is empirical rather predictive.

2.4.1.2 Discrete Drop Method

Due to the limitations of the 'Enhanced Spray Zone' approach, a new model was proposed by Toschkoff *et al.* [69], where the particles in the spray zone are detected based on contact between the spray droplets and the particles. In the model, spray droplets are represented by solid particles, since a spray description based on particles are closely aligned with reality. All drop-drop contacts are neglected and no force calculation is carried out. Once a droplet comes into contact with a particle (e.g. tablet or seed), the droplet is removed from the simulation and the mass of the droplet is added to a global particle property called coating mass. In general, the following kinematics for collisions of droplets are considered in the model,

- Drop – drop: the collision is neglected and the calculation proceeds to the next particle
- Drop – non-drop particle (i.e. seed or tablet): The droplet is removed from the simulation and its mass is added to the particle global coating mass property.
- Drop – wall: The droplet is removed from the simulation and its mass is added to the geometry global coating mass property.

Since the droplets in this model are represented by solid particles, it is possible to incorporate the right particle size and velocity of the droplets which would result in a more realistic and accurate prediction of coating uniformity. Similar to the 'Enhanced Spray Zone' approach, the coating uniformity of particles can be evaluated by considering both coating mass coefficient of variation and residence time of particles in the spray zone. The coating residence time can be calculated based on detection of particle with increased coating mass. A snapshot from DEM simulation of tablet coating in a horizontal rotary drum coater carried out by Toschkoff *et al.* [69], is shown in Figure 2.9.

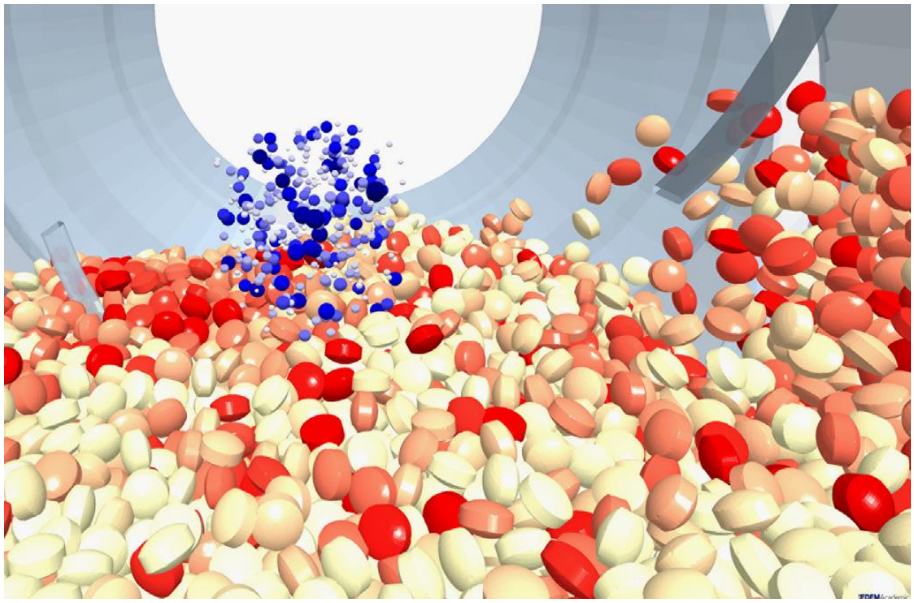

Figure 2.9: DEM simulation of tablet coating in a horizontal drum coater using spray drop model. The spray droplets are shown in blue, the lighter shades indicating smaller droplets. The tablets are coloured according to their coating mass where red colour showing high coating mass and white colour indicating tablets with no coating mass [69]

This model is more reliable than other models for processes where the shape of the spray zone is complicated, i.e. rotary seed coaters. Moreover, depending on the type of coating liquid, the size and velocity distribution of droplets can be measured experimentally and incorporated in the simulations. In most cases, the existence of coating on the surfaces of particles may change the flowability of particles. It is possible to account for changes in cohesion and friction of particles by establishing a relationship between the amount of coating on the surface of particles and their adhesion, then change the adhesion of particles based on particle's coating mass in this model. It is noteworthy to mentioning no such work has been reported in the literature.

2.4.1.3 Ray-tracing Model

In coating processes where the coating liquid is applied to the surface of a particle bed, ray-tracing models can be used in order to investigate the coating uniformity of particles [69]. This model is considered as a post-processing approach for DEM simulations where the position, velocity, angular velocity and orientation of all particles in the system are obtained at defined intervals. The detection of particles in the spray zone is achieved in a similar way to the discrete drop method with one difference being that they are detected by the intersection of a virtual drop (ray)

trajectory and the particle, as shown in Figure 2.10A. In the case of a spherical particle with a centre *c*, unit-length direction vector *a*, and a radius of *r*, the distance between the ray origin, *o*, and the intersecting point, *d*, can be calculated using,

$$d_{1,2} = (c-o)\cdot a \pm \sqrt{D} \tag{2.4.15}$$

$$D = \left[(c-o)\cdot a\right]^2 - (c-o)\cdot(c-o) + r^2 \tag{2.4.16}$$

For values of *D*, greater than zero, the ray and particle are considered to intersect, for values equal to zero, the particles and rays are considered to be tangentially touched and for values less than zero, they do not intersect. Once the above equation is solved for all the particles at each interval, the coating mass accumulated during the coating process can be calculated by accumulating the number of rays intersecting individual particles. Similarly, the number of visits to the spray zone and single-visit residence time can be calculated [63]. Toschkoff *et al.* [69] investigated reliability of ray-tracing algorithm by varying the number of rays used in the model. A range of 24 – 572 rays were chosen and the coating relative standard deviation of particles were calculated, as shown in Figure 2.10B. They reported that a minimum of 200 rays is required to reach an asymptotic value relative standard deviation. In their work, the number of rays in the algorithm were chosen randomly and therefore it may not represent the experiments. Moreover, the results obtained using this method were not compared with experiments.

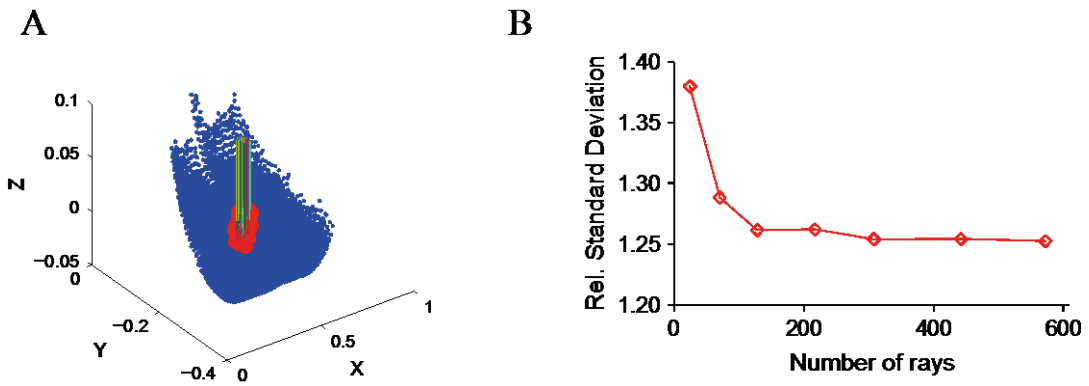

Figure 2.10: A) Principle of ray-tracing method where the blue and red dots are the centre position coated and uncoated particles, respectively. The vertical line represent the ray. B) Relative standard deviation of coating mass as a function of the number of rays [69]

2.5 Concluding Remarks

The attrition of particles under shear deformation and impact has been extensively investigated in the literature. For agricultural seeds, some work has been reported on the extent of breakage under impact, however, no work has been reported for extent of breakage under shear deformation. Since the seeds undergo shear deformation while passing through various seed processing unit operations, this should also be analysed. To do so, the existing methodologies for measuring particle should be tailored for agricultural seeds since a small amount of damage to the seeds may result in degradation of their germination.

DEM simulations have proved useful in understanding and optimising various particulate processes. For particle coating in particular, many studies have been carried out using DEM to understand the effect of various process parameters on coating uniformity of particles. Most of the work reported in the literature focuses on tablet coating, in which rotating drum coaters were analysed. In this study however, the mixer dynamics are different to those used in the literature and no such analysis is reported for the mixer used in this study. Various coating contact models have been reported in the literature, however there is a need to tailor them to seed coating processes.

In DEM simulations it is important to calibrate the simulation parameters with those achieved in the experiments. This is due to the fact it is difficult to accurately measure some material and parameters used in simulations, such as static friction, rolling friction, coefficient of restitution and shape. It has been shown that the motion of particles in DEM can be affected by their shape. Many studies have been carried out in the literature to accurately simulate the effect of particle shape. Among the existing methods of consideration of particle shape, manipulation of coefficient of rolling friction of spheres and clumping multiple spheres promise to be adequate in the case of corn seeds since they are fairly smooth and spherical. However, the validity of the two methods has to be investigated systematically to consider which method is most suitable for simulating the coating process in DEM.

CHAPTER 3 Materials and Methods

There is much in literature on understanding the mixing and coating of pharmaceutical powders [65,67,69,78,79,81–83] using various types of drum coaters. For agricultural seed coating however, no work has been reported. In this work, an attempt is made to understand the dynamics of flow and coating mechanism of corn seeds in a vertical drum batch mixer. To achieve this goal, a series of experiments and DEM simulations are carried out. The experimental work consists of obtaining material physical properties (e.g. size, shape, Young's modulus, hardness etc.) which are necessary for DEM simulations and validating the flow of particles in the investigated mixer. The validation of DEM simulations is required since the flow of corn seeds affects the mixing and coating uniformity of seeds. Hence, an accurate simulation of particle flow is required. Additionally, a short study is carried out to establish the methodology for measuring the extent of corn seeds breakage under shear deformation. Particle breakage in particulate processes is mainly caused by impact and shear deformation of particles. Seed breakage under impact deformation has been extensively studied in the literature, however, there is a lack of understanding on breakage of agricultural seeds under shear deformation. Therefore, it is desirable to develop an appropriate analysis based on particle shear deformation in order to understand the mechanism of breakage for agricultural seeds (i.e. corn and turnip seeds). For analysis of seed breakage, a series of experiments are carried out to measure the extent of breakage under various shear stresses in an annular shear cell, detailed in Chapter 4. In this chapter the methodology used for obtain the material physical properties, and the resulting measurements, the contact model used for simulating inter-particle interactions and method of measuring the extent of breakage of particles are detailed.

3.1 Experimental Materials

The material chosen for analysing extent of breakage in the shear cell were turnip and corn seeds. The latter is supplied by Syngenta Ltd, Bracknell, UK. The breakage analysis under shear deformation using an annular shear cell was initially carried out on turnip seed since the existing shear cell at the University of Leeds was not sufficiently large to accommodate the corn seeds, due to their size distribution. The experiments and modelling of particle flow and coating uniformity in the seed mixer are carried out using corn seeds. Corn and turnip seeds were sieved prior to the

experiments and the modes of size distributions of turnip and corn seeds are used (1.18 – 1.4 mm and 7.1 – 8.0 mm, respectively). Figure 3.1 show the images of a number of turnip and corn seeds that have been sieved to the above size ranges, and deviate more from spherical shape.

Turnip Seeds **Corn Seeds**

Figure 3.1: Images of a number 1.18 – 1.4 mm turnip and 7.1 – 8.0 mm corn seeds.

As it can be seen from the figures above, the turnip seeds have a uniform particle shape and they are relatively spherical. Corn seeds, however, have a variation in shape compared to turnip seeds.

3.2 Material Properties

3.2.1 Aspect Ratio

The aspect ratio, a_r, describes the length of a particle relative to its width and can be calculated using,

$$a_r = \frac{l}{w} \tag{3.2.1}$$

where l and w are length and width of particle, respectively. The aspect ratio of corn seeds was measured by capturing their images using a Canon EOS Rebel T3i camera. The obtained images from the camera were then converted to binary images (black and white) and the aspect ratio of the corn seeds was calculated using ImageJ software. It was found that corn seeds have an average aspect ratio of 0.90, with a standard deviation of 0.06. The upper and lower limits of calculated aspect ratio were found to

be 1 and 0.65, respectively. The binary and obtained images of a number of corn seeds for measurement of their aspect ratio are shown in Figure 3.2.

Captured Image Segmented Image

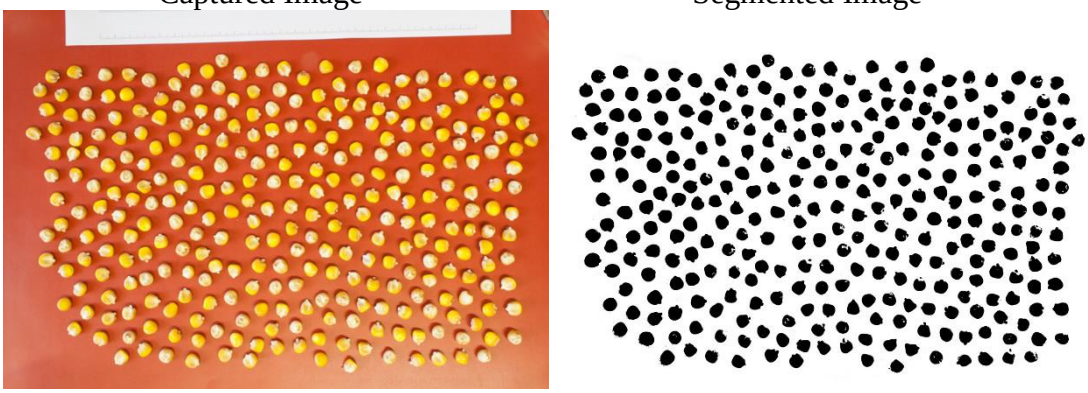

Figure 3.2: Captured and binary image of corn seeds for aspect ratio measurements.

3.2.2 Coefficient of Restitution

The coefficient of restitution, *e*, represents the degree of elasticity in a collision of an object to another which can be measured using a high speed camera recorder. The coefficient of restitution is measured by impacting one object to another stationary object, and given by,

$$e = \frac{v_2}{v_1} \tag{3.2.2}$$

where v_1 and v_2 are the velocity of the object before and after the impact, respectively. Although this parameter depends on the surfaces of both objects in collision, a value is generally considered for a given material.

The coefficient of restitution of twenty corn kernels was measured using a Redlake HG-100K high-speed digital camera. The kernels were individually dropped from a height of approximately 200 mm onto a flat stainless steel plate. Their incident and rebound velocities (v_1 and v_2, respectively) were obtained using ImageJ software. The average coefficient of restitution for twenty corn kernels was 0.69 and due to variation in particle shape and orientation during the impact, a relatively large standard deviation (0.13) was found. Moreover, the upper and lower limit of the measured coefficient of variation was 0.32 and 0.85, respectively.

3.2.3 Hardness and Young's Modulus

The hardness and Young's modulus of the corn kernels were assessed by nanoindentation. Nanoindentation tests provide a measure of force and penetration depth, from which the hardness, *H*, is inferred. The hardness of a material is given by,

$$H = \frac{P_t}{A} \tag{3.2.3}$$

where P_t is the maximum applied force and *A* is the projected plastic area. A typical force-displacement curve obtained from nanoindentation is shown in Figure 3.3. In conventional hardness tests, the hardness of the materials is obtained by measuring the size of the indenter imprint by microscopy. However, for nanoindentation, the size of impression is calculated indirectly by relating the projected area to the penetration depth, as given in Table 3.1.

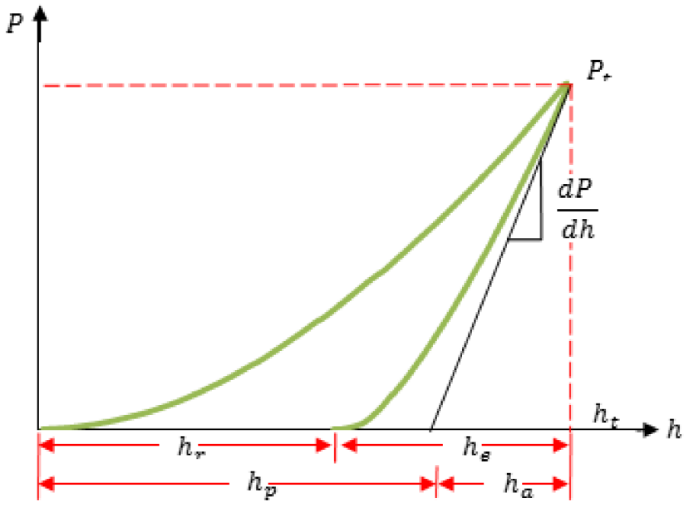

Figure 3.3: Loading and unloading curve obtained from indentation test with a maximum load of P_t and total penetration depth of h_t . dP/dh, h_a, h_p, h_r and h_e , are stiffness, depth of contact circle, depth of residual impression and displacement associated with elastic recovery during unloading, respectively.

Table 3.1: Various indenter specifications for calculation of projected imprint size [14].

Indenter Type	Projected Area	Semi-angle θ°	Effective cone angle α°	Intercept factor	Geometry correction factor β
Spherical	$A \approx \pi 2Rh_p$	N/A	N/A	0.75	1
Berkovich	$A = 3\sqrt{3}h_p \tan^2\theta$	65.3°	70.3°	0.75	1.034
Vickers	$A = 4h_p^2 \tan^2\theta$	68°	70.32°	0.75	1.012
Knoop	$A = 2h_p^2 \tan\theta_1 \tan\theta_2$	θ_1=86.25° θ_1=65°	77.64°	0.75	1.012
Cube Corner	$A = 3\sqrt{3}h_p^2 \tan^2\theta$	35.26°	42.28°	0.75	1.034
Cone	$A = \pi h_p^2 \tan^2\alpha$	N/A	N/A	0.72	1

Young's modulus, *E*, is a measure of the stiffness of a material, and is quantified as the ratio of stress to strain,

$$E = \frac{\sigma}{\varepsilon} \tag{3.2.4}$$

In indentation, the reduced modulus of the indenter and the sample is given by,

$$E_r = \frac{\sqrt{\pi}}{2}\frac{S}{\sqrt{A}} \tag{3.2.5}$$

$$S = \frac{dP}{dh} \tag{3.2.6}$$

where *S* is the contact stiffness (see Figure 3.3). The reduced modulus of the contact is related to Young's moduli and poisson ratios of the sample and indenter in the following manner,

$$\frac{1}{E_r} = \frac{1-v_s^2}{E_s} + \frac{1-v_i^2}{E_i} \tag{3.2.7}$$

where subscripts *s* and *i* refer to the sample and indenter, respectively.

For nanoindentation, corn seeds were stuck to a sample holder by superglue. A small quantity of the superglue was applied to the sample holder and spread to produce a thin coating on the sample holder. The sample holder was then inverted and lowered onto the surface of corn kernel, which was lying flat on a glass slide. The sample holder was then attached to the nanoindentation stage. The nanoindentation test machine used here was a NanoTest, manufactured by Micro Materials Ltd, Wrexham, UK.

The NanoTest device comprises a Berkovich nanoindenter and a microscope. The separation distance between these was calibrated. Indentation sites were selected using the microscope with a 10× magnification. The sample stage was then moved in front of the indenter and the sample brought into contact with the indenter. The indenter was driven into the sample at a fixed loading rate of 4 mN/s, until a pre-defined maximum depth was obtained. Once the maximum penetration is achieved, the indenter is kept stationary for 10 s prior to unloading at the same rate. The indentation load-displacement curves for four corn kernels are shown in Figure 3.4. The average hardness and Young's modulus of the corn seeds were found to be 348.8 MPa and 7.56 GPa, whilst a small variation was found where the standard deviation for the former and latter was 116.5 MPa and 1.56 GPa, respectively.

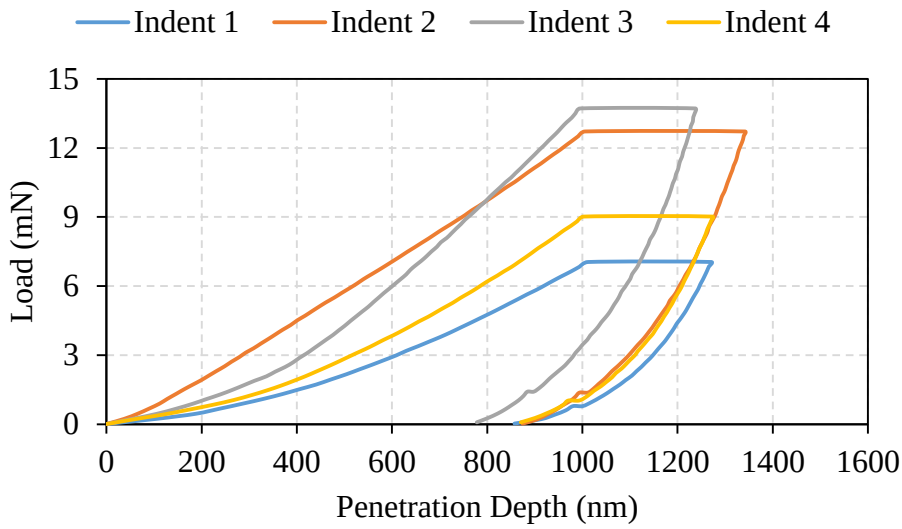

Figure 3.4: Indentation load-displacement curves for four corn kernels at maximum indentation penetration depth of 1 µm.

3.3 Particle Shape

X-Ray Micro Tomography (XMT) is a non-destructive technique for visualising internal features and external shape of porous and non-porous particles and obtaining digital information on their 3D geometry and structural properties. This technique is particularly useful in characterising particle shape for use in DEM simulations. The process of XMT consists of taking a number of X-ray radiographs (referred to as projection images) at various angles by projecting an X-ray beam through the specimen and measuring the energy attenuation of the beam received on the detector. The energy attenuation of the beam is captured as the specimen is rotated on a viewing stage, which mainly depends on the density and the thickness of the specimen in the direction of the beam. The grey level value of each projection image represents the net intensity of the X-ray beam passing through the object in the direction along a line connecting the X-ray source and the image pixel. Since the energy attenuation of the X-ray beam is dependent on material absorption and density, it is important to choose an appropriate X-ray energy level when scanning. In general, the higher the atomic number, the higher the density of the material, and the more energy is lost as the X-ray penetrates the sample [86]. In an image where two different materials with two different densities and absorption levels exist, an energy level that is too high leads to similar grey level values for both material, whereas energy levels that are too low leads to a faint image. Therefore, it is important to use the right level of X-ray beam energy in order to obtain a good image for analysis.

Filter Back-projection can be used to reconstruct the 3D volume of the specimen. A schematic diagram of how a sample is scanned and the reconstructed 3D volume of the sample is created is shown in Figure 3.5.

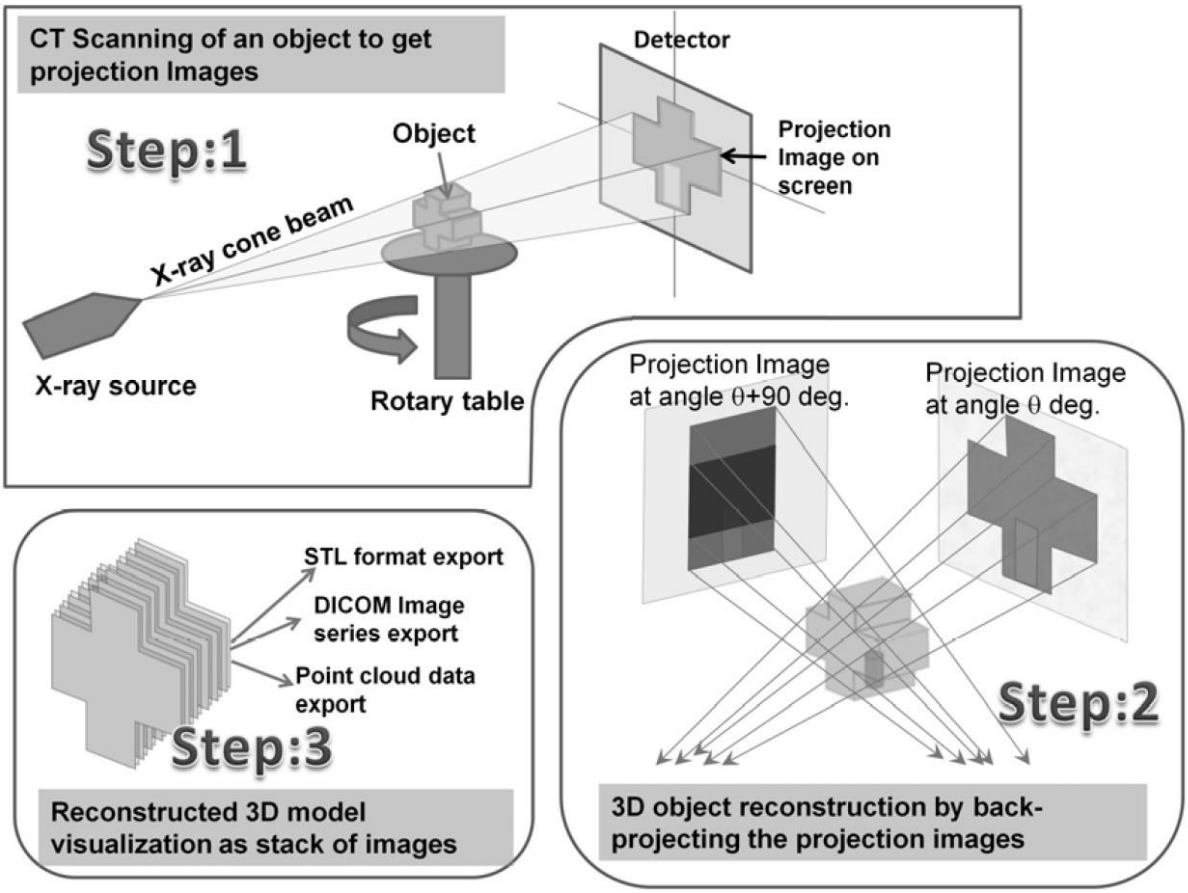

Figure 3.5: Schematic diagram of X-ray Tomography principles.

Once the 3D volume of the specimen is obtained, a range of image analysis techniques can be used to visualise the internal structure of the specimen and obtain digital information on their 3D geometry and structural properties. In general, the following operations are carried out on the images in order to reveal the internal structure of the sample:

- Filtering the raw dataset
- Grey level thresholding
- Separation and connectivity analysis
- Quantification
- Visualisation

Depending on the structure of the sample, the technique for image analysis can vary. In this study, a GE Phoenix Nanotom was used to obtain the 3D volume of the samples, VGStudio software was used to reconstruct the images from projection images and Avizo Fire software was used for image analysis of the obtained volumes.

Since the contrast of the obtained images from XRT is strongly influenced by the Xray beam power source (Voltage and Current), a series of optimisation tests were carried out and it was found that voltage and current values of 100 kV and 350 mA, respectively, result in an optimum contrast for the corn seeds.

3.3.1 Image Processing

Apart from optimum XRT parameters, image processing of the acquired XRT images is the most important part in the analysis. Image analysis operations on images can result in a change of structure of the images, therefore an incorrect image processing technique leads to misleading information about the structure of the material of interest. It is therefore important to choose the right techniques to ensure the final results are as close as possible to the real structure of the material.

In general, image filtration and segmentation are the key image processing operation which could lead to misleading results. However, it is possible to minimise the degree of error in the analysis by choosing the right techniques for these operations. A brief description of the operations that can be applied to the images are described below.

3.3.1.1 Image Filtration

Due to the nature of any image acquisition techniques, the acquired images contain a degree of noise, which should be minimised (possibly removed) in order to carry out analysis on the images. There are a wide range of image filtration (image smoothing) techniques available in the literature, such as Gaussian, Median, Edge-preserving and Non-local mean filters that can be used to achieve this goal. However, these techniques are case dependent and it is critical to ensure the right technique is chosen for each dataset. A non-local mean filter was used to eliminate the majority of the noise in the dataset, whilst maintaining the sharpness of the edges.

3.3.2 Image Segmentation

Image segmentation is an image processing technique where a digital image is partitioned into multiple segments (sets of pixels or voxels) in order to simplify or change the representation of an image into a form that is more meaningful and easier to analyse. Each pixel is assigned to specific labels such that the pixels with the same label share similar characteristics. There are a wide range of image segmentations techniques available in the literature, such as manual segmentation, manual and automatic thresholding, and watershed segmentation.

In the case of corn seeds, an automated segmentation technique was used. This technique is applied based on the image histogram, where the distribution of grey level values in the image as function of number of pixels is calculated. From the calculated histogram, the maxima, representing the presence of various material (e.g. air and particles), is identified and boundaries between these maxima are calculated.

3.3.3 Separation of Segments and Labelling

In the process of image segmentation, the image is converted into a binary image, where each pixel value represents a certain material with the same density and absorption. In order to obtain information about the shape and structure of individual particles, it is necessary to separate the connecting particles from each other. An image processing technique, known as grain separation, is used to separate individual particles from each other. In this method the local maxima on the distance map of the binary image are calculated and the probability of the pixels belonging to the local maxima is calculated and therefore the particle boundaries are established. Once the boundaries are found, a watershed technique is used in order to remove the connecting pixels on the edges, which leads to the separation of particles in the image. Once the particles are separated, a binary value is assigned for each particle by the labelling module of Avizo Fire software. Moreover, the particles on the edge of the image are removed from the analysis as they do not represent a complete shape of a particle.

3.4 Method of Assessing Breakage

Chipping and fragmentation are the most common causes of particle breakage. The generation of sub-surface lateral cracks as a result of a minimum applied force extends to the surface of particle; it leads to the removal of small chips of material. Once the applied force reaches a threshold force, radial cracks will extend to the centre of particle and causes fragmentation of particles [18]. In the chipping breakage mode, the size distribution of chips is very narrow whereas in fragmentation mode the size distribution of fragmented particles is very wide. Figure 3.6 shows schematically the typical size distributions generated from these two breakage mechanisms [29].

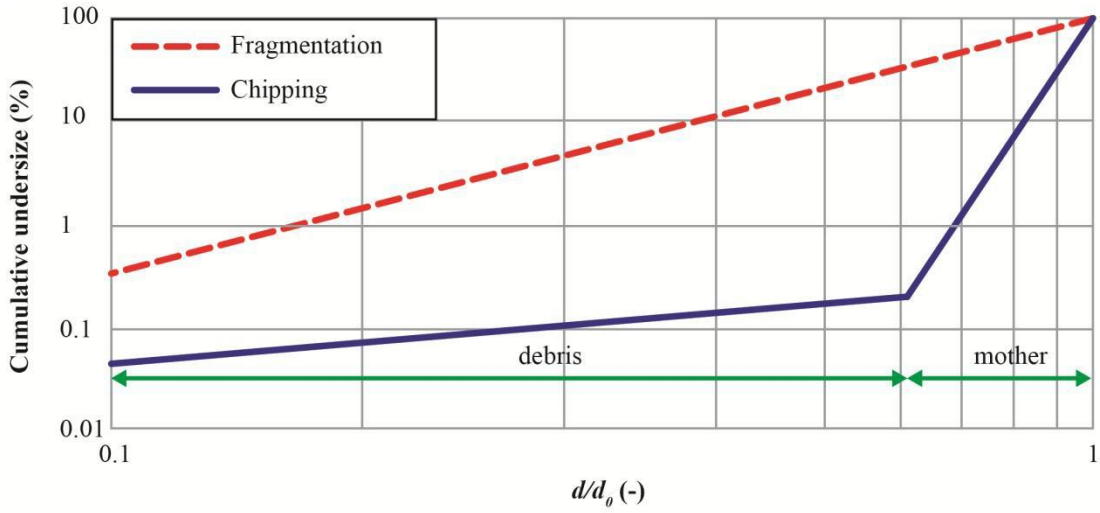

Figure 3.6: Schematic representation of particle breakage modes

In order to assess the fraction of debris, a cut-off sieve size above which mother particles are expected and below which the particles represent debris must be considered. Consideration of two sieve sizes below the feed size is reported in the literature to represent an appropriate cut-off point [43]. This approach is also chosen here as the base of analysis and in the further step, a modified method is proposed for analysing the extent of seed breakage in the shear cell.

According to Ghadiri and Zhang [2], due to material handling, it is possible to lose some of material while sieving the material, hence they suggested that this loss could be attributed to either mother particles or debris. The extent of breakage can therefore be defined by R^- for the former case and R^+ for the latter case,

$$R^- = \frac{m_{de}}{m_f} \times 100 \tag{3.4.1}$$

$$R^+ = \frac{m_f - m_m}{m_f} \times 100 \tag{3.4.2}$$

where m_{de}, m_f and m_m are the mass of debris, feed and mother particles respectively. As the fraction of mother and debris in the lost material cannot be experimentally identified, the extent of breakage can be evaluated based on the collected material as described by the following equation,

$$R^* = \frac{m_{de}}{m_m + m_{de}} \times 100 \tag{3.4.3}$$

In this work, turnip seeds are initially classified based on the size of seeds using a Haver & Boecker EML Plus 200 shaker. The sieving experiments are carried out with a sieving time of 3 minutes, a frequency of 50 Hz, amplitude of 1 mm and a rest time of 2 seconds after every 5 seconds. The broken materials after shear cell experiment are also classified using the mentioned parameters. Similar shaking conditions are also used for corn seeds.

CHAPTER 4 Seed Breakage in a Shear Cell

In this chapter, the developed methodology for measuring the extent of breakage of turnip and corn kernels under shear deformation using an annular shear cell is presented. Experimental work using an annular shear cell, based on the design of Paramanathan and Bridgwater [6], was carried out on the turnip and corn seeds to measure the extent of breakage under shear deformation. Initially, turnip seeds were used to establish appropriate breakage criteria, as discussed in Section 4.1, for the existing cell used by Hare [29] whilst a new shear has been developed in this work for the corn seeds as size of the previous cell was unsuitable to accommodate corn seeds due to their large size distribution. The extent of breakage is measured, for both turnip and corn seeds, as function of various applied normal stresses and strains.

The shear cell consists of an annular base with radially-grooved ring to grip neighbouring particles and is filled with seeds up to a chosen height. The height of the seeds in the cell is controlled by using a T-shape piece of plastic to flatten the bed surface and any excess material is removed. The lid of the cell, similar to the cell base consisting radially-grooved ring, is then lowered onto the bed surface to apply a normal stress to the bed. A stopper-arm is placed on the cell lid which prevents the lid from rotation. This causes the seeds to be sheared since the movement of particles near the wall are inhibited by the stopper. The resistance of the flow caused by this results in the formation of a velocity gradient across the bed hence generating a shear stress in the bed. The level of strain to the bed is controlled by limiting cell rotation once a pre-set cell rotation is reached. According to Neil and Bridgwater [25], the bed strain is given by,

$$\Gamma = \frac{\theta_c}{360}\frac{\pi D_c}{h} f \qquad (4.1.1)$$

where θ_c is the cell rotational angle, D_c the mean diameter of the cell, h the bed height and f the grip factor of the groove ring. The material is removed after designated cell rotation, the cell is dismantled and any debris on the groove rings are gently brushed. The extent of breakage after shearing is then assessed as described in Section 3.4.

The work done by Paramanathan and Bridgwater [20] on analysis of bed deformation in an annular shear cell showed that a shear band of five to six particle diameter exists

in the cell; hence a bed height of approximately six times the median sieve size of the seeds is used. The inner and outer diameter of the annular cell used here are 120 and 160 mm for turnip seeds and 120 and 230 mm for corn seeds, respectively. This results in a mean diameter of 140 and 175 mm and a strain rate ratio of 0.75 and 0.52 between the inner and outer extremities of the cell for turnip and corn seeds, respectively. The size of the inner and outer diameter of the cell is chosen in a way that the average bed strain describe the extent of bed deformation, although there is a slightly greater and smaller strains at the outer and inner diameter of the cell, respectively.

4.1 Turnip Seed Breakage

Turnip seeds were initially used since the existing shear cell at the University of Leeds, used by Hare [29], was unsuitable for large size corn seeds. The analysis of the seed breakage was carried out using the method of Neil and Bridgewater [25]. Four breakage criteria were proposed to assess the extent of breakage of seeds as shown in Table 4.1. The breakage is defined as the mass percentage of collected material passing through a certain sieve below the lower feed size. The extent of breakage generally increases as stress and strain increases.

Table 4.1: Proposed analytical criteria for assessing breakage of seeds

Criteria Name	Description
Criteria 1	Mass of debris is determined based on the total mass of particles which are two sieve-cut below the feed particle size
Criteria 2	Mass of debris is determined based on the total mass of particles, which is one sieve-cut below the feed particle size
Criteria 3	Mass of debris is determined based on the total mass of particles which is smaller than the feed particle size
Criteria 4	Mass of damaged particles is determined based on the sum of total mass of particles, which are smaller than the feed particle size and the amount mother particles which are damaged

The gripping factor, *f*, for the existing shear cell was estimated by analysing the slip of a coloured band of particles, as shown in Figure 4.1, against the grooved rings after 360° cell rotation. The gripping factor is then calculated using,

$$f = \frac{\theta_c - (\theta_{sl} + \theta_{su})}{\theta_c} \tag{4.1.2}$$

where θ_{su} and θ_{sl} are the degree of slip between the upper and lower groove rings and the particles, respectively. At the minimum and maximum normal stresses, turnip seeds were found to slip 10 degrees against the upper and lower grooves; hence resulting in a grip factor of 0.94. For intermediate bed stresses of turnip seeds similar gripping factor was assumed.

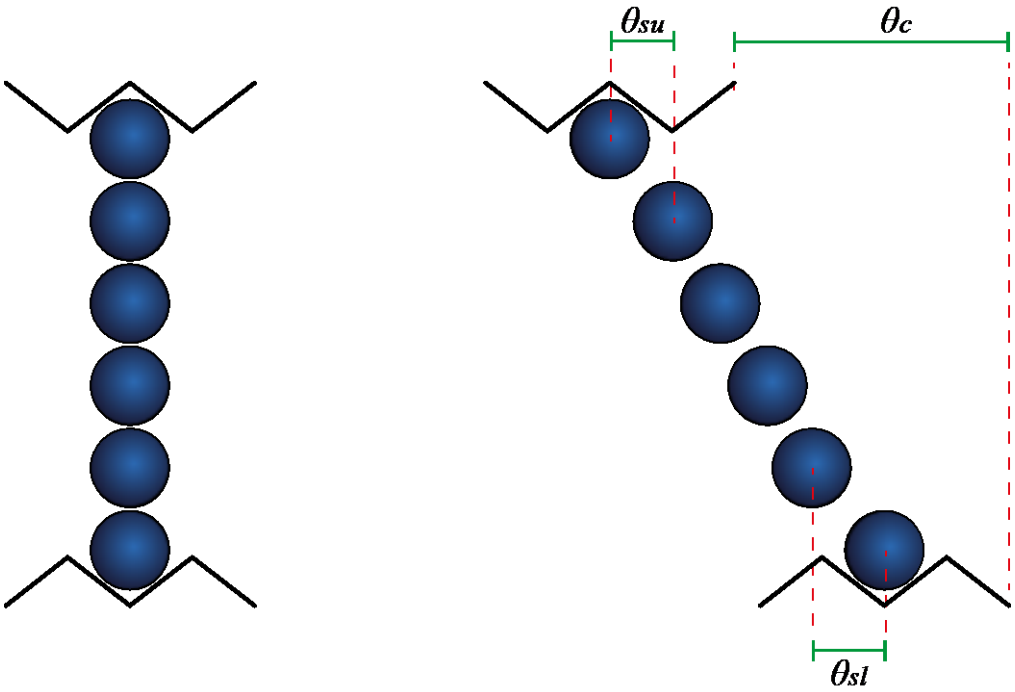

Figure 4.1: Schematic diagram of slip between particles and groove rings.

The extent of breakage of turnip seeds was investigated by applying a range of normal stresses and strains as given in Table 4.2. Initially, the breakage of 1.4 – 1.7 mm turnip seeds was measured using Criterion 1. Using this criterion, the extent of breakage is measured by three breakage definitions (R^+, R^- and R^*). The results are shown in Figure 4.2. In the case of R^+, the trend exhibits discrepancy in the breakage of turnip seeds as the normal stress increases; hence this would not represent the extent of breakage in the case of seeds since the size of debris is not sufficiently small to be lost. The values of R^- and R^* overlap and the trend shows an increase in the breakage as normal load is increased, although this increase is not significant. In fact it is unlikely that the material loss is from the large mother particles. Hence, the extent of breakage throughout this work is assessed based on the breakage definition (R^*).

Table 4.2: Shear cell experimental setup for turnip seeds

Normal Stress σ (kPa)	Number of Rotations
3	1
4.3	1
7.7	1
20	1
28	1, 2, 3, 5, 10

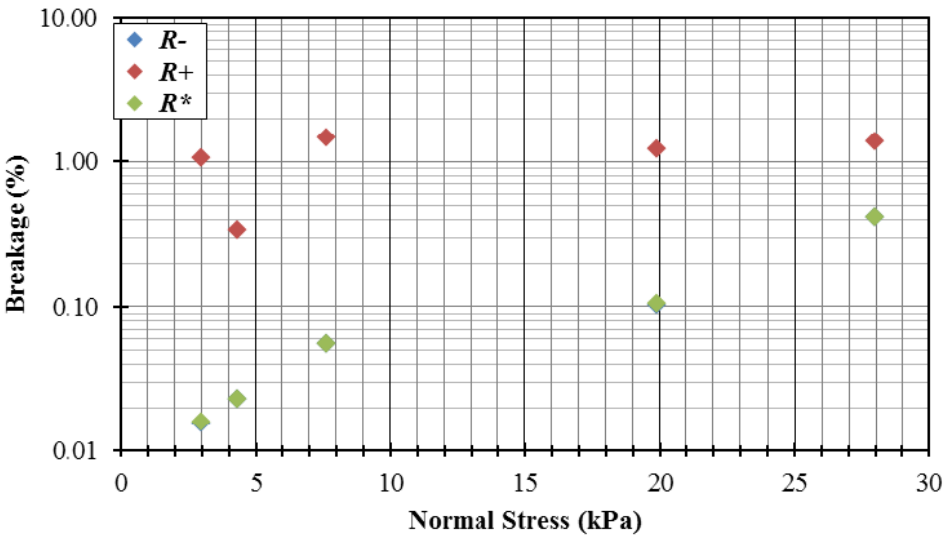

Figure 4.2: Extent of breakage of 1.4 – 1.7 mm turnip seeds, subjected to shear strain corresponding to one cell rotation based on three definitions (R^+, R^- and R^*) using Criterion 1 (the green and blue data points are overlapping and are not clear on the graph).

Due to insignificant change in the trend of breakage, a new series of experiments were carried out at the high normal load of 28 kPa for different number of rotations. The results are shown in Figure 4.3, where the extent of breakage is plotted as a function of strain, corresponding to 1, 2, 3, 5 and 10 complete cell rotations. The extent of breakage increases as strain increases. At a strain of 117, the breakage decreases and this could be due to experimental errors, which require further to ensure the accuracy and repeatability of the results. However, as the emphases was shifted to corn kernels work and other data points showed good consistency. This data point was not repeated. A series of image analysis, by microscopy, was carried out to check the validity of the obtained analytical results. Five random sample of approximately 200

particles were chosen for each sieve-cut. The inspection revealed that most of the particles which were classified as two sieve-cuts below the feed particle size (less than 1 mm) were damaged. This suggests that the assessment of seed breakage using Criterion 1 is not valid as it does not consider the particles which are below the mentioned sieve-cut as damaged particles. The obtained images of turnip seeds in the range of 1 – 1.8 mm after application of 3 – 28 kPa normal stress are shown in Figure 4.4.

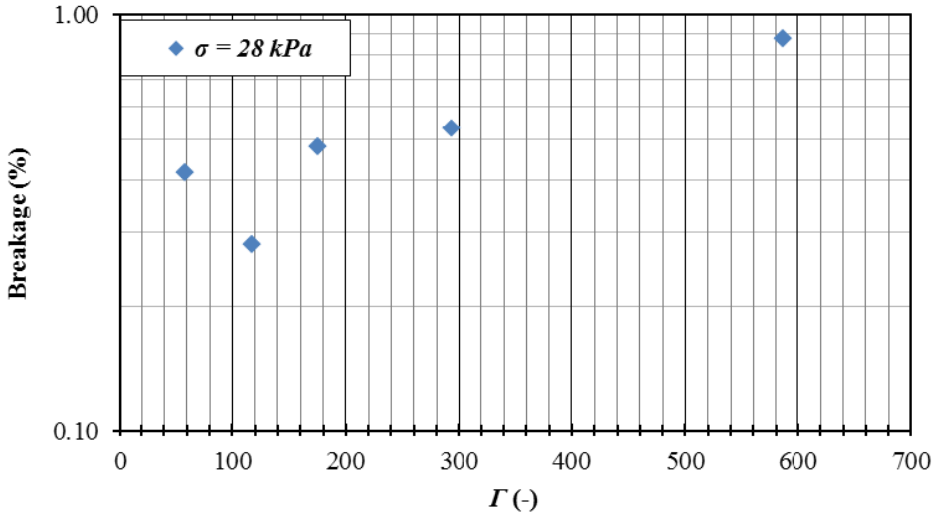

Figure 4.3: Extent of breakage of 1.4 – 1.7 mm turnip seeds as a function of strain for normal stress of 28 kPa.

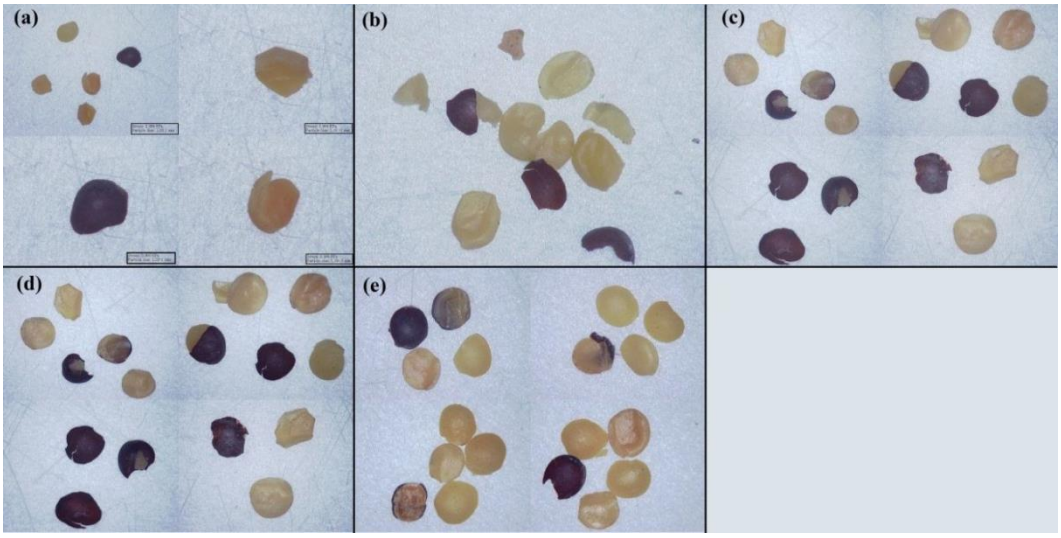

Figure 4.4: Damage to the seeds in the range of 1 - 1.18 mm for (a) 3 kPa, (b) 4 kPa, (c) 7.7 kPa, (d) 20 kPa and (e) 28 kPa normal stresses.

Further inspection was also carried out for the turnip seeds classified by one sieve-cut below the feed size, as shown in Figure 4.5. A considerable amount of damaged seeds was also found for this sieve range of seeds. These particles should also be considered as debris for analysing the extent of breakage. In fact, this suggests that Criterion 2 is not suitable enough to evaluate the extent of breakage for turnip seeds. Similarly, damaged particles were also present in the sieve-cut of mother particles; however the fraction of damaged particles was considerably less than that of the sieve-cut below. This is represented in Figure 4.6.

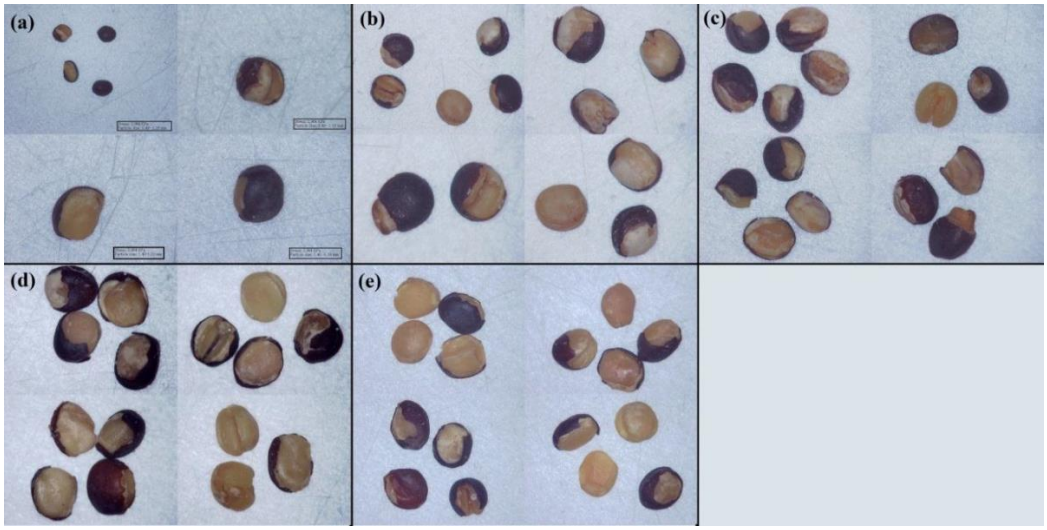

Figure 4.5: Damage to the seeds in the range of 1.18 - 1.4 mm for applied normal stresses of (a) 3 kPa, (b) 4.3 kPa, (c) 7.7 kPa, (d) 20 kPa and (e) 28 kPa.

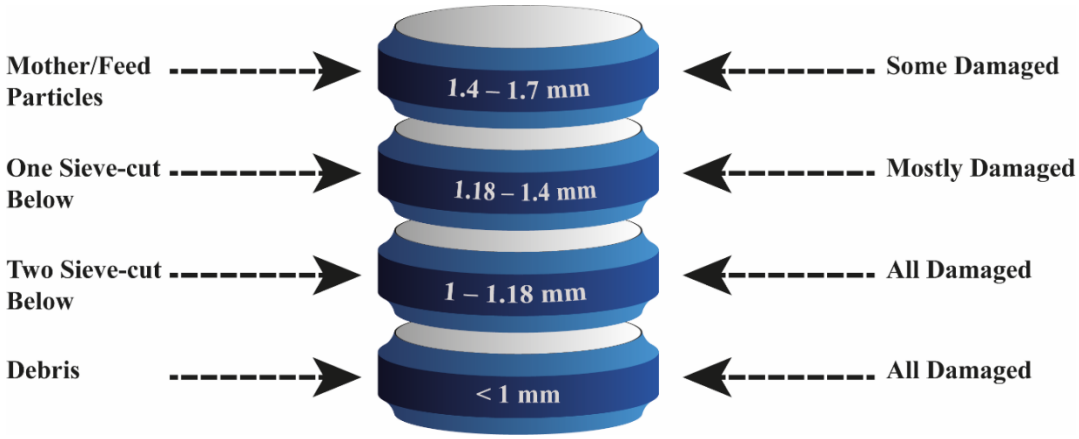

Figure 4.6: Schematic representation of collected damaged turnip seeds after shearing.

It is clear that even among the feed particle size range, there are particles that are damaged. These particles should also be considered as damaged particles for the

breakage analysis. Therefore, Criteria 2 and 3 are not able to evaluate the extent of breakage sufficiently well for the seeds. Criterion 4 suggests that the total damage is made of the mass of debris and damaged mother particles,

$$m'_d = m_{de} + m_{dmg}$$
$$m'_m = m_m - m_{dmg} \tag{4.1.3}$$

where m'_d , m'_m and m_{dmg} are masses of debris and damaged mother particles, undamaged mother particles and damaged particles, respectively. In order to measure the mass of damaged particles, five sampling portions are selected from the mother particles and the broken seeds are determined by visual inspection using microscopy and the weights of these damaged seeds are measured. Accordingly, the breakage of the seeds can be calculated using the following equation.

$$R^{*} = \frac{m'_d}{m'_m + m'_d} \tag{4.1.4}$$

The extent of breakage evaluated by the four proposed models as a function of normal stress and strain are shown in Figure 4.7 and Figure 4.8, respectively. The measurement of the extent of seed breakage using Criteria 3 and 4 show a more realistic value (based on image analysis) and can be chosen as the assessment model. Criteria 3 gives a close agreement with Criteria 4 and it requires a considerable less experimental effort to measure the extent of breakage. Therefore, a strategic decision is needed on which base to adopt based on the required accuracy of results.

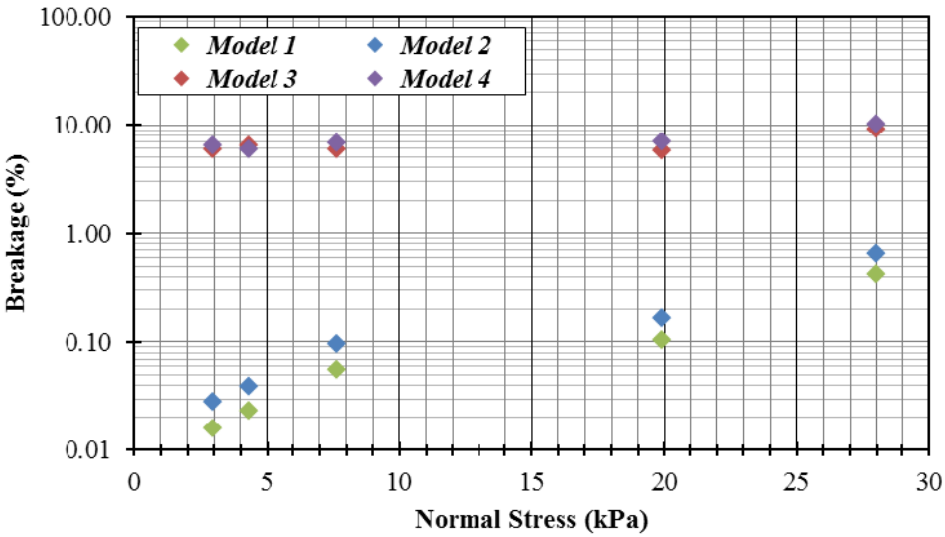

Figure 4.7: Comparison of the extent of breakage of 1.4 – 1.7 mm turnip seeds as a function of normal stress based on proposed the models.

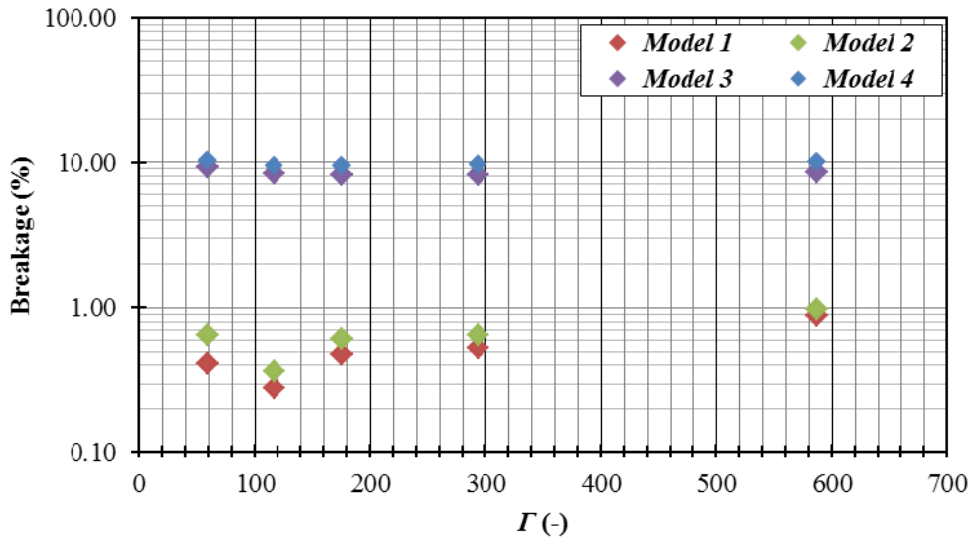

Figure 4.8: Comparison of the extent of breakage of 1.4 – 1.7 mm turnip seeds as a function of strain at applied normal stress of 28 kPa based on the proposed criteria.

4.1.1 Concluding Remarks

Four seed breakage criteria were evaluated to analyse the extent of the breakage of turnip seeds. Among the proposed criteria, Criterion 4 showed most reliable and realistic method of measuring breakage of turnip seeds. It is shown that the extent of breakage increases with increasing the normal applied stress and strain. It is also shown that that breakage analysis needs to be validated by the use of image analysis technique in order to measure the extent of breakage more accurately. The size of debris and mother particles are sufficiently large that it is unlikely to lose particles and debris while carrying out the sieving; hence the extent of breakage can be calculated using R^*. Therefore, the breakage of seeds can be assessed based on collected mass of material by using Eq (4.1.4). A close agreement was found using Criteria 3 and 4; however, Criterion 3 is much quicker to perform and a strategic decision was made on which criteria to use based on the required accuracy of results.

4.2 Corn Seed Breakage

The analysis of the extent of breakage of corn seeds was carried out using Neil and Bridgwater [25] method. Corn seeds were too large for the existing shear cell, hence a new shear cell was developed for the corn seeds. The height and width of the grooves

are chosen based on the work done by Ghadiri *et al.* [4] where they suggested that the grooves height should be between 25% and 38% of particle diameter and a width of at least one particle diameter is required. Hence, for corn seeds in the range of 7.1 – 8 mm, the height and width of grooved were chosen to be 2 mm and at least one particle diameter (near the inner wall), respectively. The schematic representation of the grooves is shown in Figure 4.9.

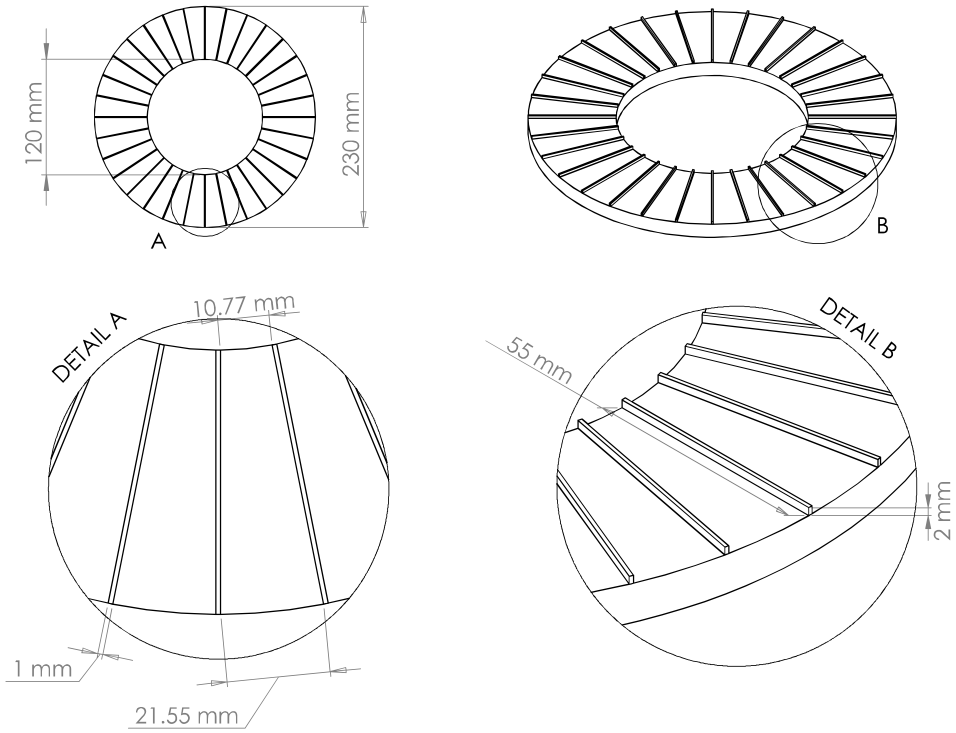

Figure 4.9: Schematic representation of new shear cell grooves.

Similar to the shear cell used for turnip seeds, the gripping factor of the bed in the cell was evaluated by placing a band of coloured corn seeds and measuring the angle of slippage of seeds against the upper and lower grooves, as shown in Figure 4.10. Corn seeds were found to slip 9° after shearing the bed for 180°, resulting in a gripping factor of 0.90.

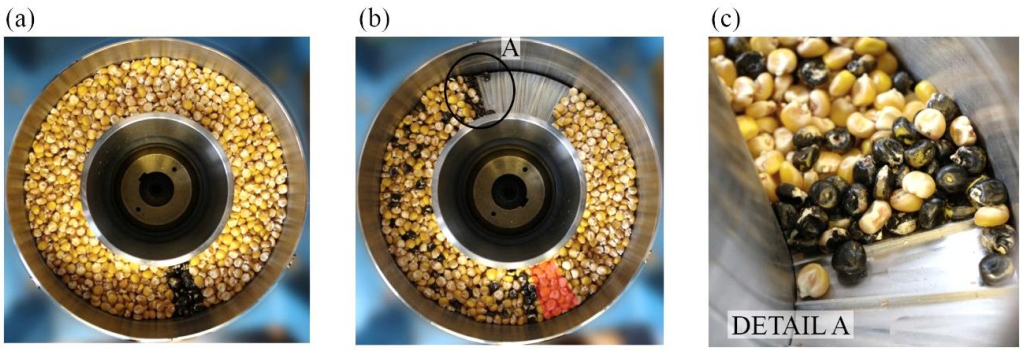

Figure 4.10: Position of colour band seeds (a) before and (b) after shearing for measuring the bed slip angle against the top and bottom grooves. The highlighted area (shown in red colour) is the position of marked particles before shearing.

The extent of breakage of corn seeds in the annular shear cell was investigated by applying a range of normal stresses and strains. The strain that the bed of corn seeds experienced is controlled by varying the number of rotation of cell, as shown in Figure 4.11, where the error bars in the graph represent the minimum and maximum strain that the particles experience near the inner and outer wall, respectively. The range of normal stresses that is applied to the bed was chosen based on the minimum and maximum load that can be used using the annular shear cell at the University of Leeds and is summarised in Table 4.3.

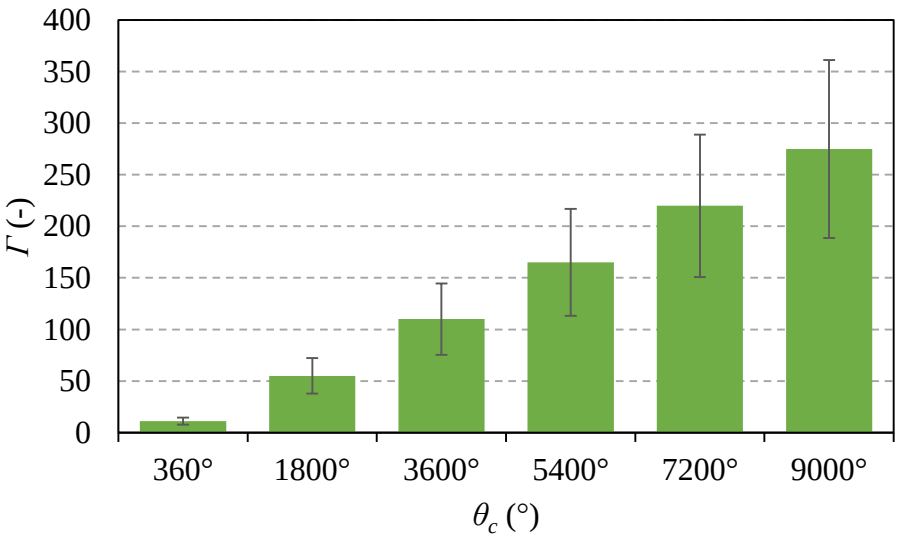

Figure 4.11: Calculated Strain as function of rotational angle. The error bars corresponds to the strain near the inner and outer wall of the cell.

Table 4.3: Stresses applied to the bed of corns using dead weight

Added Mass (kg)	Normal Stress (Pa)
0	2891
4.22	4260
8.28	5577
16.98	8399
33.16	13649
37.98	15212

Corn seeds were classified by sieving and the material on the sieve-cut corresponding to the mode of particle size distribution was used in the experiments. The breakage analysis was carried out using four proposed breakage criteria, as described in Section 4.1. Initially, the breakage of corn seeds was measured using Criterion 1 and the three extent of breakage (R^+, R^- and R^*) were assessed. The results are shown in Figure 4.12. Similar trends were observed compared to turnip seeds, where the values of R^- and R^* overlapped and in the case R^+, the trend exhibits notable differences in the breakage of corn seeds as the normal stress increases. Due to unlikelihood of losing mother particles and debris during the experiments, the extent of breakage throughout the experiments on corn seeds was assessed based on the total breakage parameter (R^*).

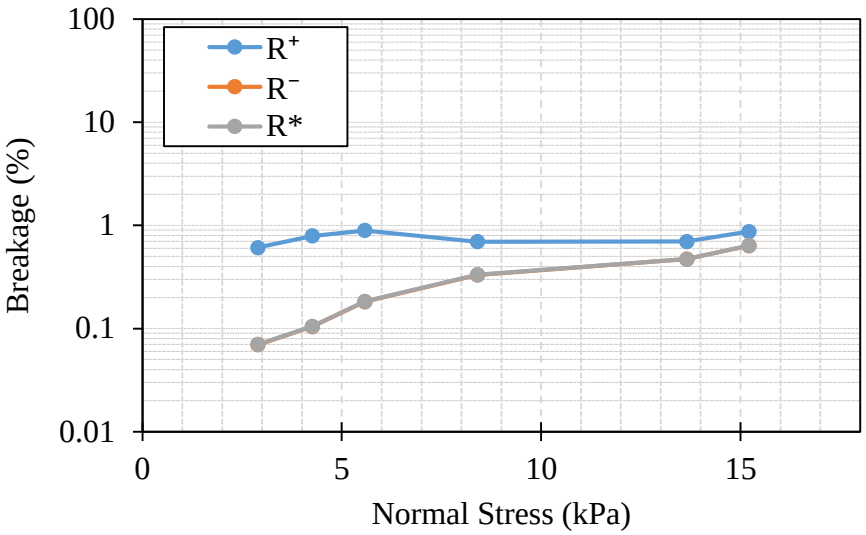

Figure 4.12: Extent of breakage of 7.1 – 8.0 mm corn seeds subjected to shear strain of 11 (one rotation) as a function of applied normal stress based on three definitions (R^+, R^- and R^*) using Criterion 1 (the grey and orange data points are overlapping).

The analysis of corn breakage using the applied stresses and strains are shown in Figure 4.13 and Figure 4.14 as is assessed based on Criteria 1. In general, the extent of breakage increases with increasing the stress and strain. However, the increase in the level of breakage is not significant with increasing the level of stress and strain.

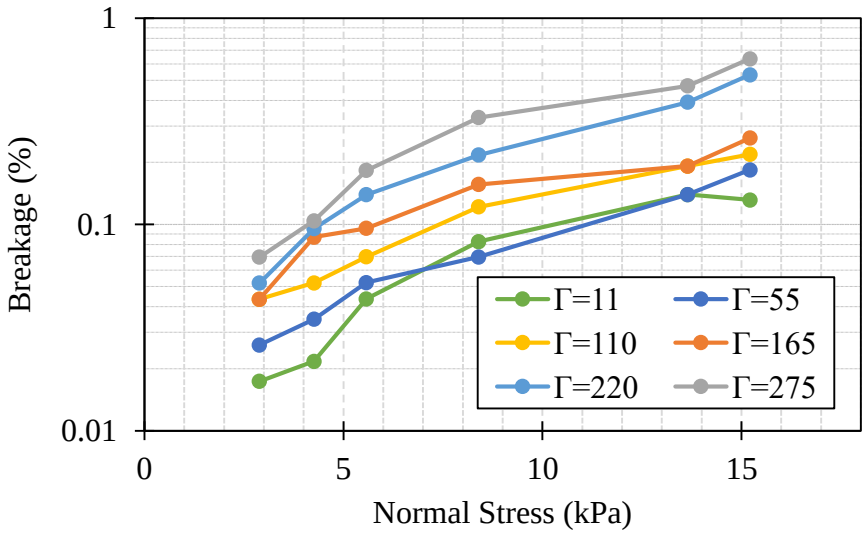

Figure 4.13: Extent of breakage of 7.1 – 8.0 mm corn seeds as a function of applied normal stress for various applied shear strains.

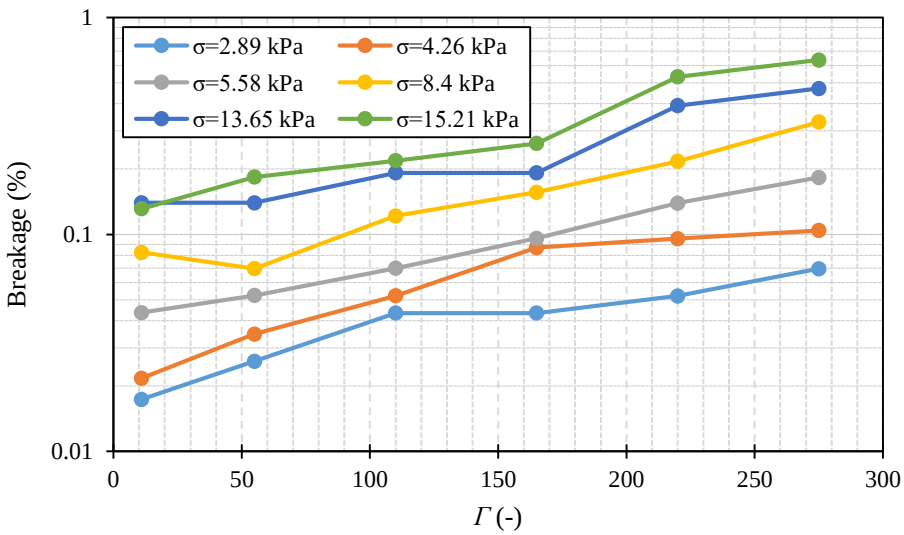

Figure 4.14: Extent of breakage of 7.1 – 8.0 mm corn seeds as a function of applied shear strain for various applied normal loads.

Similar to the turnip seed experiments, a series of image analyses were carried out for investigating the extent of damage to corn seeds visually. At each applied normal force, a series of images of mother particles and debris are captured using a USB microscope. The collected materials below the feed size were mainly dust; hence suggesting there is no breakage at these levels of stresses and strains. This is also validated by comparing the extent of breakage using the four suggested criteria, where no significant change in the trend was observed by considering each criteria. The comparison of the extent of breakage of corn kernels using the four proposed criteria as function of applied normal stress and strain is shown in Figure 4.15 and Figure 4.16. It has to be noted that at the highest stress and strain, only one seed was found to be damaged. The dust material generated after the test, known as 'Bee's Wing', come mainly from the tip of the corn seeds.

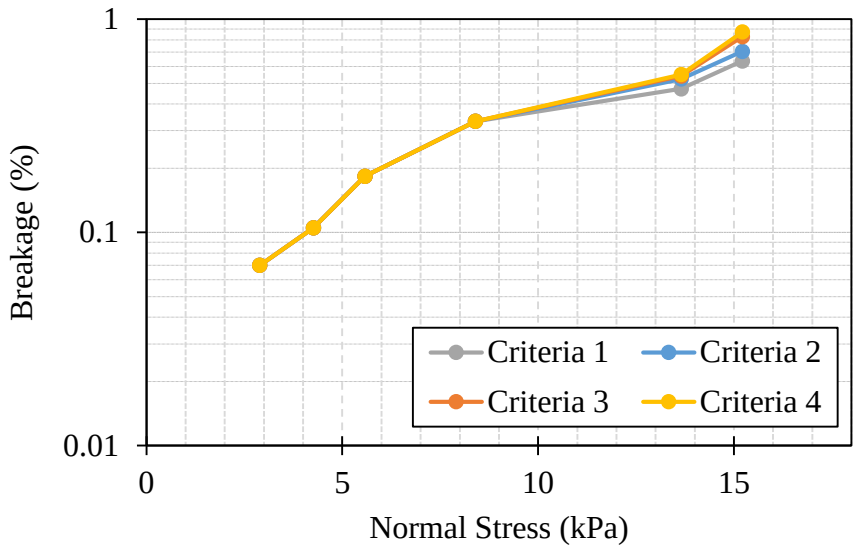

Figure 4.15: Extent of breakage of 7.1 – 8.0 mm corn seeds subjected to a shear strain of 272 as a function of applied normal stress.

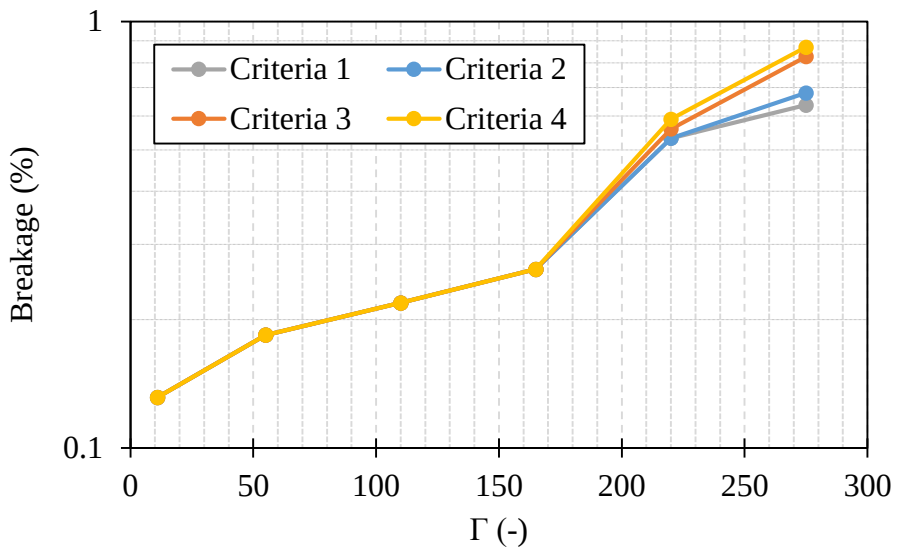

Figure 4.16: Extent of breakage of 7.1 – 8.0 mm corn seeds subjected to applied normal stress of 15.2 kPa as a function of applied shear strain.

Since no breakage was observed at the applied normal forces and strains mentioned above, a new series of experiments were carried out to investigate the effect of bed height on the extent of breakage of corn kernels. The intention of these tests was to investigate whether the kernels experienced breakage while passing through small clearance gaps in various unit operations; hence four bed heights of 15, 20, 25 and 45 mm were chosen, which represented a bed height of approximately 2, 3, 4 and 6

particle diameter, respectively. The applied normal stress and strain were kept constant for all tests. According to Eq. (4.1.1), strain changes with changing the bed height; hence the amount of rotation of cell was adjusted to ensure the bed experienced the same level of strain for all bed heights. A normal load and bed strain of 15.2 kPa and 330 were considered for all the tests, respectively.

As it can be seen from Figure 4.17, the extent of breakage increases with decreasing the bed height. For bed height of 45 and 25 mm, the change in the extent of breakage was insignificant. However, as the bed height was decreased further (i.e. 20 and 15 mm), there was a considerable change in the extent of breakage especially in the case of 15 mm bed height. This suggest that the majority of corn kernel breakage is happening while the kernels pass through narrow clearance gaps under shearing. Further analysis was also carried out to check the validity of the four proposed breakage criteria, as discussed in Section 4.1. Similar to the previous experiments on validation of the proposed breakage criteria, Criteria 1 and 2 lack the consideration of the total amount of damaged particles. A good agreement between Criteria 3 and 4 and image analysis was found, suggesting both breakage criteria can be used to assess the extent of damage of seeds under shear deformation.

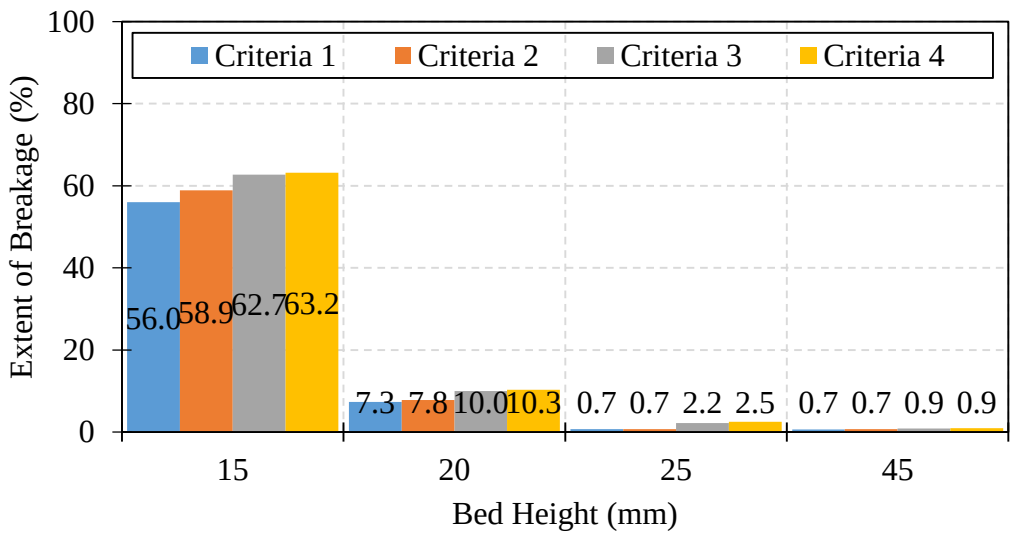

Figure 4.17: Extent of breakage of 7.1 – 8.0 mm corn seeds as function of bed height subjected to applied normal force and strain of 15.2 kPa 330, respectively.

4.2.1 Concluding Remarks

The extent of damage on corn seeds was investigated using the modified annular shear cell at University of Leeds. The gipping grooves of the cell were manufactured according to the criteria proposed by Ghadiri *et al.* [4]. Similar to experiments carried out for turnip seeds, Criterion 4 showed to be the most reliable and realistic method of assessing the damage of both turnip and corn kernels. It is also shown that the extent of breakage increases with increasing the normal load and bed strain. However, the increase of extent of breakage for the investigated normal loads and bed strains were insignificant and the debris generated after the tests were mainly dust and is referred to as 'Bee's Wing'. This suggest that under the tested conditions, it is unlikely that the corn kernels break. This was also validated by feeding the corn seeds into the seed coater and running the coating process for 30 seconds where no breakage was observed after sieving the corn kernels except generation of small amount of dust. Further investigation was also carried out to look at the extent of breakage of corn kernels while passing through small gaps under shear deformation. For this purpose, the bed height of material in the annular shear cell was varied from 15 to 45 mm. For the first two investigated bed heights (45 and 25 mm), there was an insignificant increase in the extent of breakage. However, for lower bed heights, 20 and 15 mm, a considerable extent of breakage was found. This suggests that the corn kernels tend to break more while passing through unit operations, where the kernels pass by small clearance gaps, i.e. screw conveyor.

In overall, Criteria 3 and 4 can be used for assessing the extent of breakage of agricultural kernels. Criterion 4 was found to be the most reliable and realistic method of assessing the breakage; however it requires a considerable amount time to analyse the data. Criterion 3 was found to be a faster yet still reliable and realistic method of measuring the breakage, compared to Criterion 4.

CHAPTER 5 Particle Velocity Distributions in the Mixer and the Effect of Particle Shape in DEM

The coating quality of finished product is strongly influenced by the rate of mixing and coating coverage which is in itself dependent on the spraying and spreading processes. Hence it is important to understand the effect of each process parameter on the final product quality and to optimise them. To do so, the particle kinematic behaviour (flow field, mixing pattern, etc.) needs to be analysed. DEM provides a robust way of simulating particulate systems while spherical particles are commonly used as model particles due to the simplicity of contact detection and mechanics, since contacts can be detected if the distance between two particles become less than the sum of their radii. Corn kernels investigated in this work are not spherical, hence the shape of kernels affects the motion of particles in the system. Looking at the single particle level, two types of behaviour are observed during the collisions. Considering the impact of a corn kernel onto a flat surface; (i) the kernel rebounds without changing the orientation and (ii) the kernel rotates upon impact and hits the flat surface for the second time before rebounding with a change in the orientation as well as the rebound angle. The former case can be simulated using spherical particles in DEM, while the latter can only be simulated by considering the particle shape. As discussed Section 2.3.4, there are a number of approaches for considering the shape of particles, such as using spherical particles and artificially changing their rolling friction, overlapping spheres [55], ellipses [87], polygons [88], bonded assemblies of polygons [89], sphero-simplices [90] and super-quadric particles [91]. In this study however, the effect of shape on motion of particles is investigated using the overlapping and rolling friction approaches, due to simplicity of contact detection and speed of simulations. The motion of particles in terms of tangential and radial velocity distributions is analysed and compared to experimental results.

5.1 Experimental Measurement of Particle Velocities

For both simulations and experiments, the base rotational speed is 300 rpm in anti-clockwise direction, the baffle angle is 45° and the baffle to wall clearance is 15 mm. The motion of particles moving on the bed surface near the vertical baffles is captured

using a Redlake HG-100K high-speed video camera. The velocities in the *x* and *y* directions are calculated from the travelled distance of each particle between consecutive frames (4 ms) in the measurement cell (50 mm by 50 mm) highlighted in Figure 5.1 using an automated particle tracking algorithm in ImageJ software. The motion of particles is then analysed based on the tangential and radial components, where the tangential, V_θ, and radial, V_r, velocities of the particles in the system are calculated using,

$$V_\theta = V_x \sin(\theta) + V_y \cos(\theta) \tag{5.1.1}$$

$$V_r = V_x \cos(\theta) + V_y \sin(\theta) \tag{5.1.2}$$

where V_x and V_y are velocities in *x* and *y* direction, respectively, and θ is the angular position of the particle (anti-clockwise from the x-axis). Since the observed plane is distanced from the camera lens and a single point camera is used, distortion and perspective errors have to be corrected to accurately calculate the particle velocities.

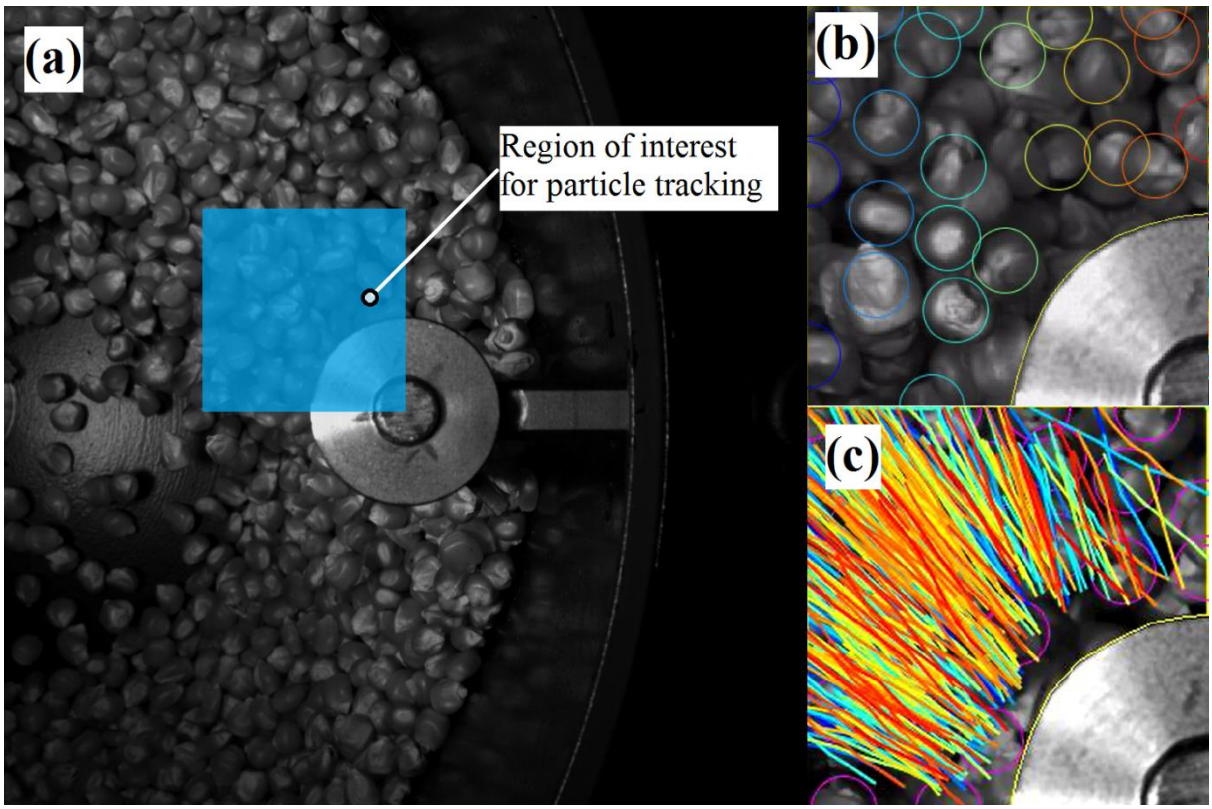

Figure 5.1: Particle tracking for obtaining tangential and radial velocity distributions of particles in the measurement cell located after the baffle; a) the region where the particle trajectories are analysed, b) detection of particles in the cell and c) representation of particle tracks within the region of interest

5.1.1 Lens Distortion Calibration

Distortion of the camera lens in this study is calibrated by placing a calibration sheet, shown in Figure 5.2, in front of the camera lens and capturing a still image. The centre point of the lens is considered as the reference point for calibration and the size of each pixel is calculated based on this reference point. A number of known positions (in pixel dimensions) on the image obtained from the distortion calibration chart obtained from the camera are considered on both the *x* and *y* axes. The position and deviation from the known distances are calculated to obtain distortion error as function of distance from the reference point as shown in Figure 5.2.

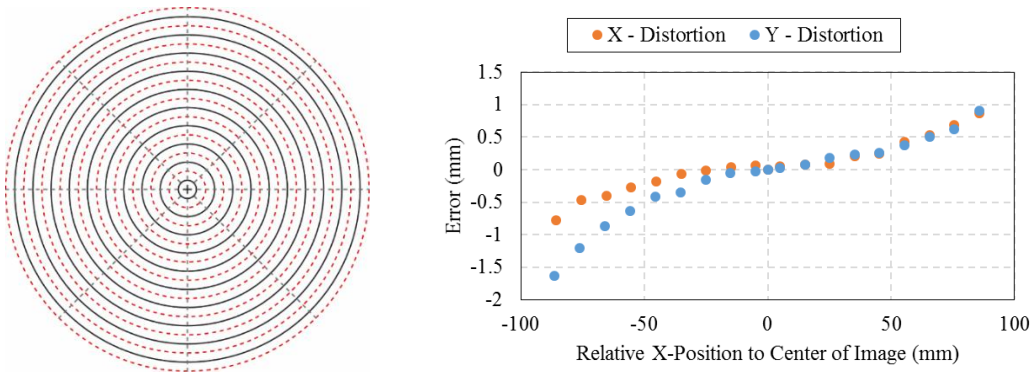

Figure 5.2: Calibration for camera lens distortion error; a) calibration chart and b) error in calculating the positions with the reference point located at the centre of the camera lens

Polynomial expression equations are then used to obtain the extent of error on each axis in the calculated the position of corn kernels,

$$\varepsilon_{Dx} = \left(9\times10^{-7}\right)x^3 + \left(4\times10^{-6}\right)x^2 + 0.0029x + 0.0477 \qquad (5.1.3)$$

$$\varepsilon_{Dy} = 10^{-6}y^3 - \left(5\times10^{-5}\right)y^2 + 0.0054y + 0.0178 \qquad (5.1.4)$$

where ε_{Dx} and ε_{Dy} are the distortion errors in *x* and *y* directions, respectively, and *x* and *y* are the calculated positions of the kernels in the *x* and *y* axes, respectively, before applying distortion calibrations.

5.1.2 Perspective Correction

The physical size of the camera sensor is smaller than the coater geometry, hence a degree of error exists in measuring the position of particles (in both *x* and *y* axis) relative to the global coordination system. A schematic diagram of the field of view of the camera directed at the seed coater is shown in Figure 5.3. Although the coater

walls are vertically aligned, they appear to be inclined in the images obtained from the camera. Hence, the *x* and *y* positions of particles measured from the obtained images have to be calibrated against field of view error.

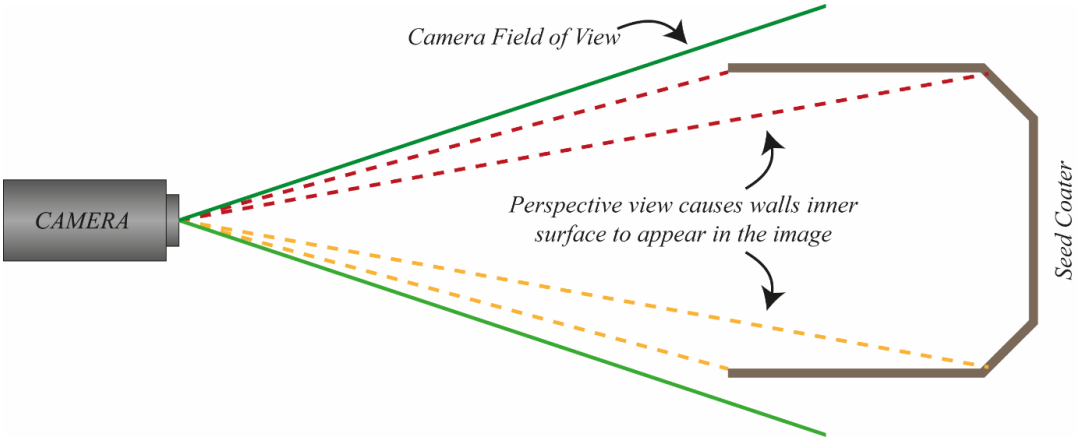

Figure 5.3: Schematic diagram of the camera field of view. The green lines indicate the camera field of view away from the camera lens and the red and orange lines indicate the appearance of the inner surface of the coater wall in the obtained image due to the perspective view.

The calibration against perspective view error is taken into account by estimating the upper and lower position of particles that form the heap next to the baffle. Using high-speed video recording, only the particles at the top of the bed surface can be analysed. However, as the surface profile is inclined, the axial position of particles is estimated by considering their radial distance from the baffle. A measurement window of approximately 10 particle diameters (80 mm) is considered after the baffle and the kernel's axial position relative to the top of the bed surface (located near the baffle) extending from the baffle is measured by a still image. A schematic diagram of the bed profile extending from the baffle is shown in Figure 5.4.

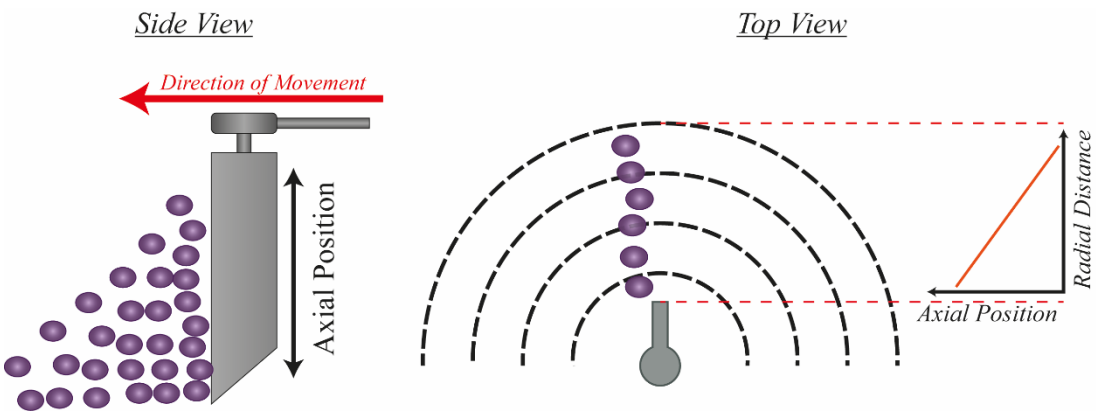

Figure 5.4: Schematic representation of position of the particles after the baffle

Similar to the distortion calibration discussed in previously, a calibration chart is placed at both extreme axial positions (lower and upper position of the bed) and a linear fit as a function of radial displacement from the baffle is considered for correcting for *x* and *y* positions of particles as they move away from the baffle. The distortion calibration is applied to the dataset prior to view factor error calibration since the distortion error exists in the image prior to the field of view error. The calibrations of field of view error as a function of kernel distance from the top of the bed and radial distance to the centre point of the baffle are shown in Figure 5.5 and Figure 5.6, where the error of *x* and *y* positions are plotted against the radial distance from the centre point of the baffle.

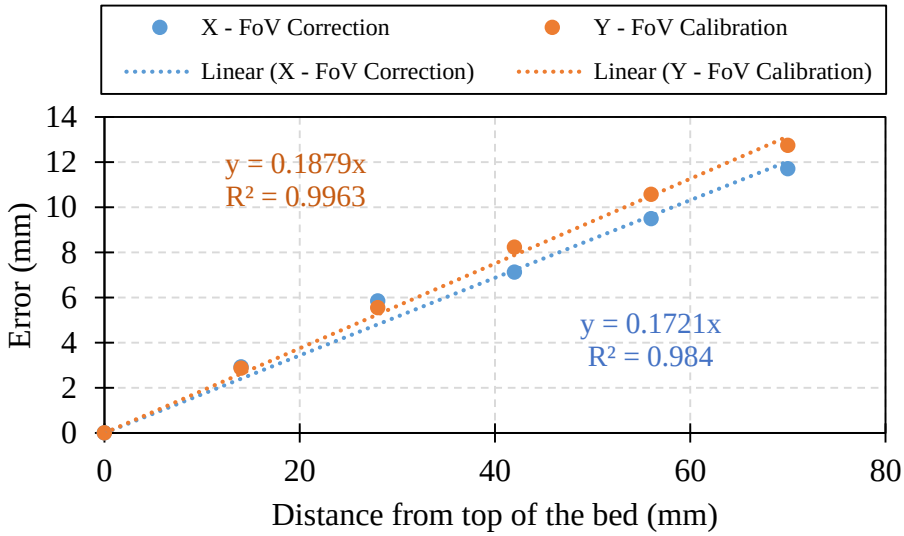

Figure 5.5: Calibration of field of view error as a function of distance from the top of the bed by considering same position on the calibration chart for all distances.

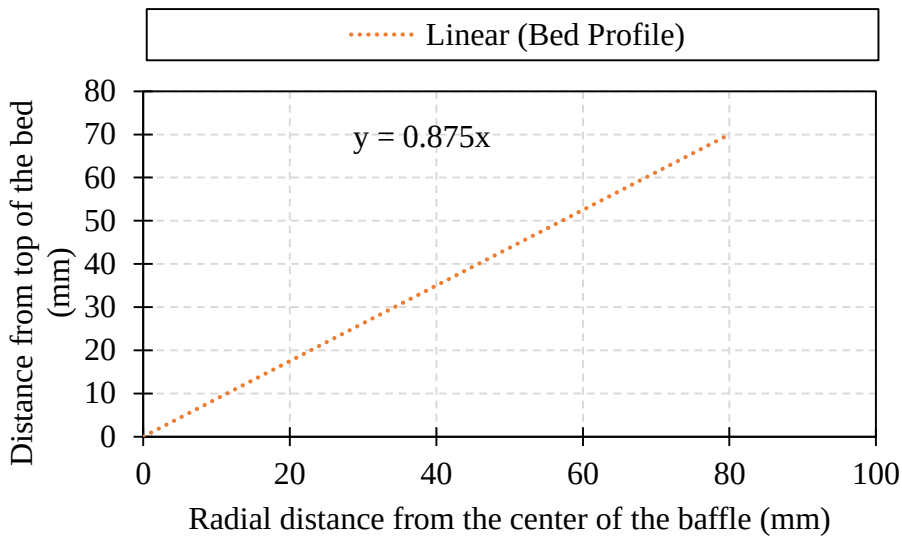

Figure 5.6: Assumption of bed profile after the baffle as a function of radial distance from the centre of the baffle.

The amount of deviation of the measured particle positions relative to the actual position of the particles in the system can then be calculated by,

$$\left.\begin{aligned} h &= 0.875\times R \\ \varepsilon_{Px} &= 0.172\times h \\ \varepsilon_{Py} &= 0.188\times h \end{aligned}\right\} \Rightarrow \left\{\begin{aligned} \varepsilon_{Px} &= 0.151\times R \\ \varepsilon_{Py} &= 0.164\times R \end{aligned}\right. \tag{5.1.5}$$

where ε is the error, h and R are the distance of particles relative to top of the bed and centre of the baffle, respectively, and subscripts Px and Py are positions of the particles relative to the centre point of the baffle in x and y directions, respectively.

5.1.3 Experimental Particle Velocity Distributions

The measured radial and tangential velocity distributions of particles in the cell located after the baffle forming the bed surface are shown in Figure 5.7 for 1250 particles over a period of 6 s (approximately 10,000 velocity samples). The total number of bins (11) and bin size that are used for generating the velocity distributions in this study are kept constant to aid the comparison. The radial and tangential velocity distributions of the particles have peak values at -0.55 and 0.39 m/s, respectively. The positive values in tangential and radial velocities indicate that the particles are moving anti-clockwise and towards the vessel wall, respectively.

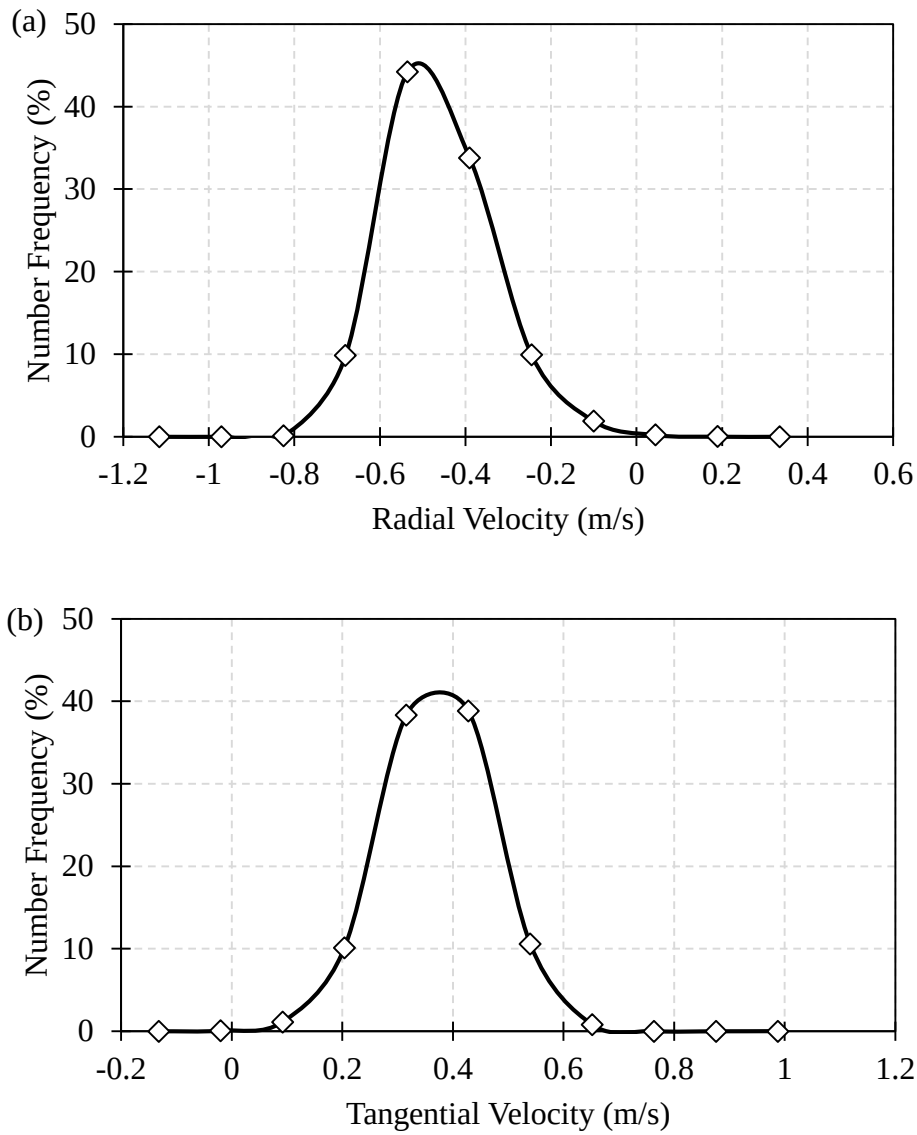

Figure 5.7: Experimental tangential (a) and radial (b) velocity distributions in the measurement cell located after the baffle.

5.2 DEM Simulations of Effect of Particle Shape

A series of DEM simulations were carried out using the EDEM® software (DEM-Solutions, Edinburgh, UK) by considering the rolling friction to account for non-sphericity of particles, and also approximating the shape by clumping a number of spheres with various sizes. The effect of particle shape is presented in terms of the radial and tangential velocity distributions of particles inside two cubic measurement cells in the seed coater as shown in Figure 5.8. The length of each side of the cubic measurement cell is 50 mm (approximately seven particle diameters).

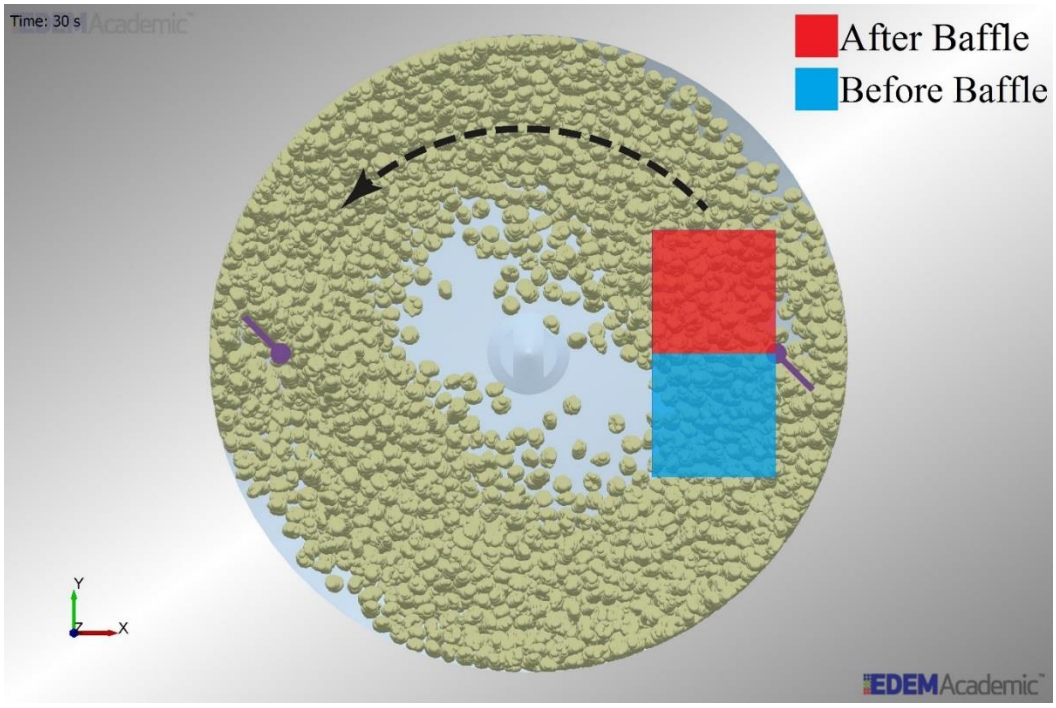

Figure 5.8: Measurement cells in DEM simulations for two positions in the vessel, one after (red) and another before (blue) the baffle

In these DEM simulations, the motion of particles in the absence of coating liquid is considered since the main interest is the bulk motion and its sensitivity on the coefficient of rolling friction. The simulations were conducted using Hertz-Mindlin contact model [29] with rolling friction based on viscous dissipation [30]. The size of vessel and particles were the same as those used in the experiments. A bed consisting of 4,200 particles corresponding to 1.2 kg of corn kernels was used. The simulations were carried out using a constant rotational speed of the base at 300 rpm for 25 s of process time. The elastic modulus of particles was reduced by two order of magnitude in order to speed up the simulations. This was considered to be appropriate since the motion of non-adhesive particles was of interest. It has been shown that varying elastic modulus to this degree is not influential on the flow patterns generated [22 - 23]. Coefficients of restitution and sliding friction of particles were measured experimentally using a high-speed video camera and the NanoCrusher® (Micro Materials, UK), at the University of Leeds, respectively. The particle properties and simulation settings are summarised in Table 5.1 and Table 5.2. A normal size distribution is considered to represent the particles in the 7.1 – 8.0 mm sieve-cut.

Table 5.1: Properties of particles and walls used in DEM simulations

Property	Seeds	Walls (steel)
Particle diameter (mm)	7.5 ± 3%	-
Shear Modulus (GPa)	0.01	70
Density (kg/m^3)	1163	7800
Poisson's Ratio (-)	0.25	0.3

Table 5.2: Contact properties used in DEM simulations

Property	Particles-Particle	Particle-Wall
Coefficient of Sliding Friction	0.3	0.3
Coefficient of Rolling Friction [52]	0.01 – 0.3	0.01
Coefficient of Restitution	0.6	0.69

5.2.1 Implementation of Clumped Spheres

X-ray tomography (XRT) is used to provide three-dimensional (3D) information on the granule structure. A Phoenix Nanotom© CT scanner (GE Measurement and Control, US) was used to obtain the 3D structure of a single corn seed in the 7.1 – 8.0 mm sieve-cut, as shown in Figure 5.9, followed by the generation of clumped spheres by the ASG2013 software, the method which is described in Section 3.3, (Cogency, South Africa) as shown in Figure 5.10. In order to investigate the effect of accuracy of shape representation, the clumped spheres were generated using 5, 10, 15 and 20 spheres, with volume errors of 0.1, 0.3, 0.1 and 0.2%, respectively, compared to the actual volume of the scanned corn seed.

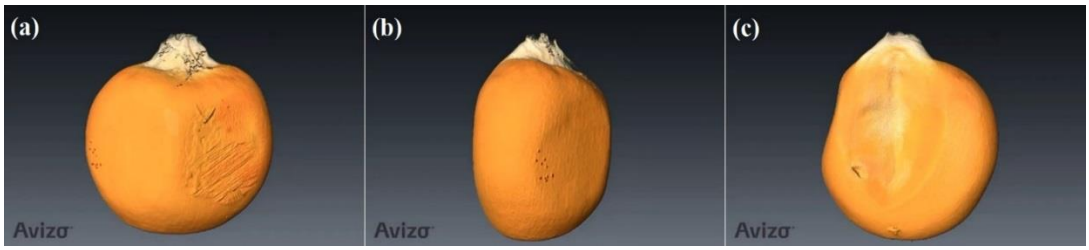

Figure 5.9: Three-dimensional structure of a corn seed obtained from XRT

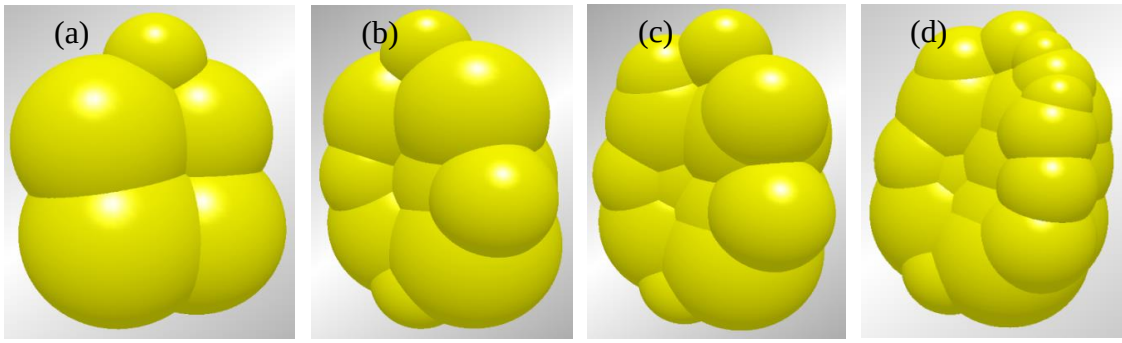

Figure 5.10: Representation of Corn Seeds in DEM using (a) five, (b) ten, (c) fifteen and (d) twenty spheres

5.2.2 Effect of the Rolling Friction Coefficient on Simulated Velocity Distributions

The predicted radial velocity distributions of spherical particles after the baffle are shown in Figure 5.11, where the rolling friction coefficient is varied from 0.01 to 0.3. The motion of particles is not sensitive to small values of rolling friction (i.e. 0.01 – 0.05). Once the rolling friction value of 0.05 is exceeded, the motion of the particles becomes more sensitive to the selected value. In the case of the tangential velocity of the particles after the baffle (Figure 5.12), the peak and span of the distribution remain relatively constant when changing the particle-particle rolling friction coefficient, suggesting the tangential motion of the particles after the baffle is not influenced by varying the particle-particle rolling friction coefficient.

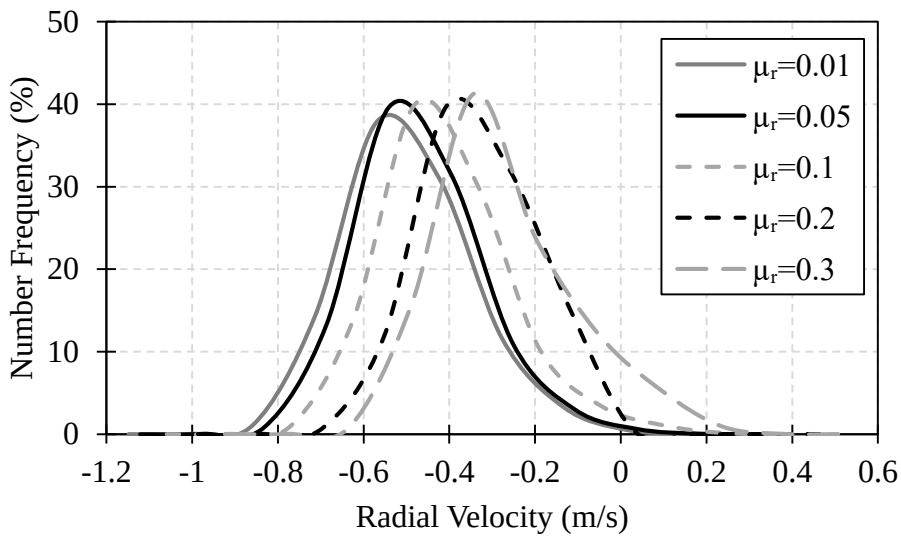

Figure 5.11: Predicted radial velocity distribution of particles in the measurement cell located after the baffle using rolling friction method

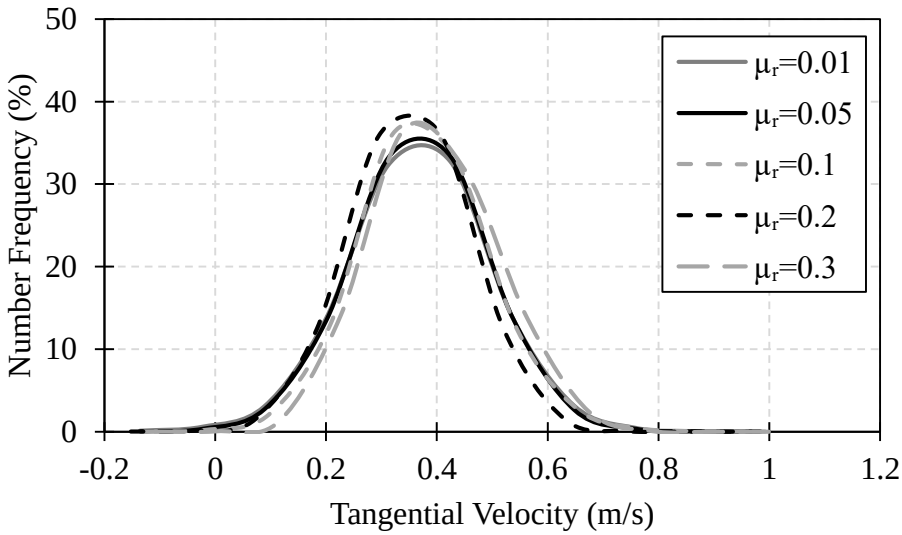

Figure 5.12: Predicted tangential velocity distribution of particles in the measurement cell located after the baffle using rolling friction method

The predicted radial velocity distributions of spherical particles in the measurement cell located before the baffle are shown in Figure 5.13. It is clear that the radial motion of particles in this case is sensitive for the entire range of investigated values of rolling friction. The magnitude of the radial velocity corresponding to the mode of the distribution decreases as the rolling friction is increased. It is most unlikely that the contacts between the particles have a shear component, therefore an increase in the rolling friction restricts the particles from rolling on each other and hence reduces the particle velocity. However, looking at the tangential velocity distribution of particles located before the baffle, as shown in Figure 5.14, the motion of particles is not sensitive to values of rolling friction coefficient in the range of 0.01 – 0.1. This suggests that using the current experimental setup (i.e. baffle angle and clearance gap), particles-particle rolling friction coefficient is more influential on the radial motion of the particles in the coater than the tangential motion.

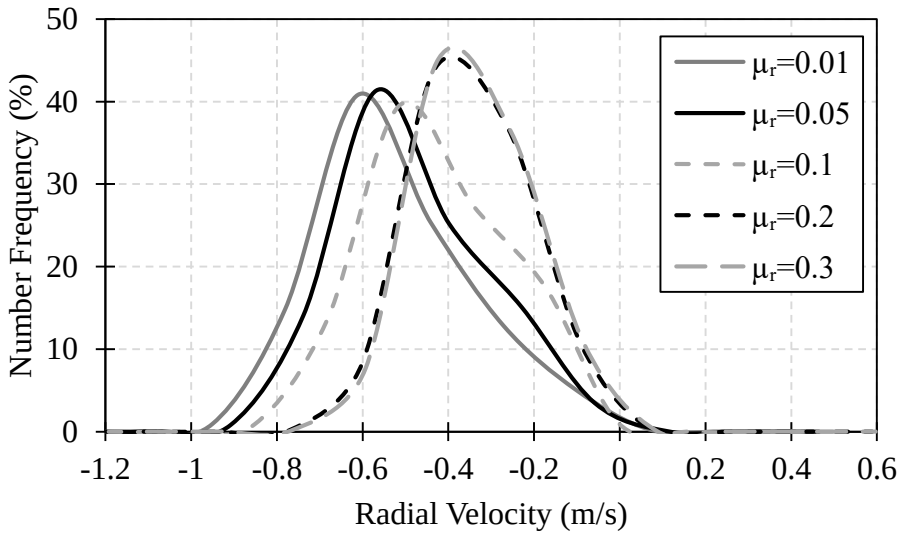

Figure 5.13: Predicted radial velocity distribution of particles in the measurement cell located before the baffle using rolling friction method

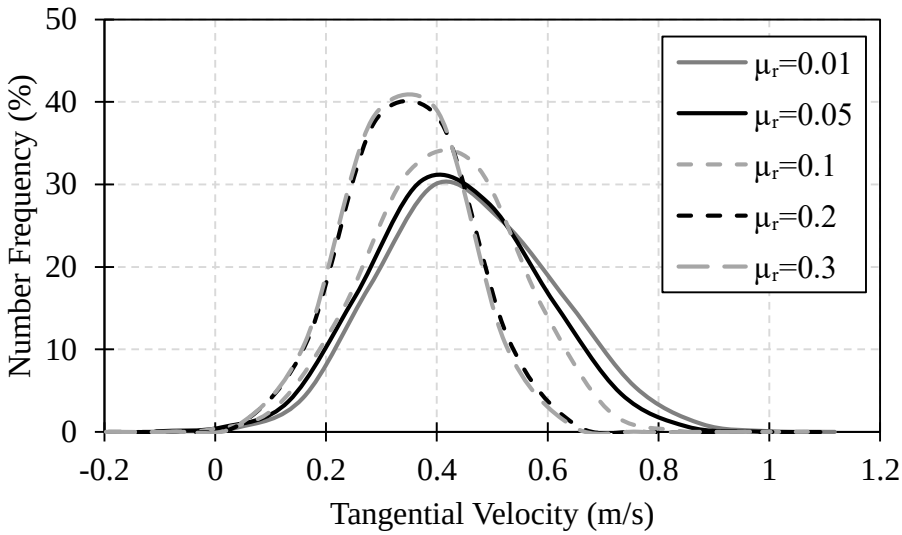

Figure 5.14: Predicted tangential velocity distribution of spherical particles in the measurement cell located before the baffle using rolling friction method

Comparing the tangential velocity distribution of particles in the measurement cells located before and after the baffle, the motion of particles is more sensitive to the value of rolling friction before the baffle than after. This is due to the fact that there are more inter-particle contacts before the baffle than after, as shown in Figure 5.15.

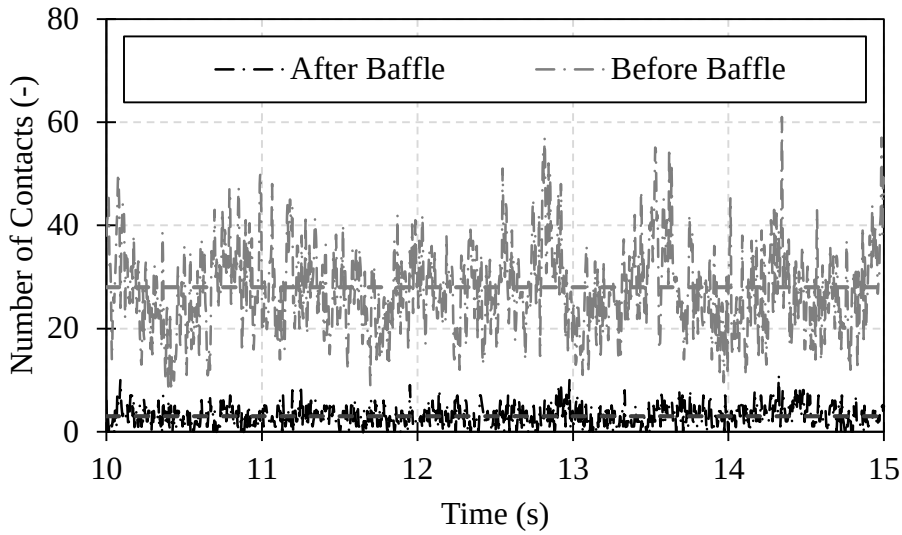

Figure 5.15: Comparison of number of inter-particle contacts in the measurement cells located after and before the baffle for the simulation of rolling friction coefficient of 0.1.

5.2.3 Effect of the Accuracy of Clumped Spheres on Simulated Velocity Distributions

The predicted radial velocity distributions of particles, as represented by a number of clumped spheres in the measurement cells located after and before the baffle, are shown in Figure 5.16 and Figure 5.17. The radial velocity of the particles is almost independent of the number of spheres used (for 5 – 20 spheres).

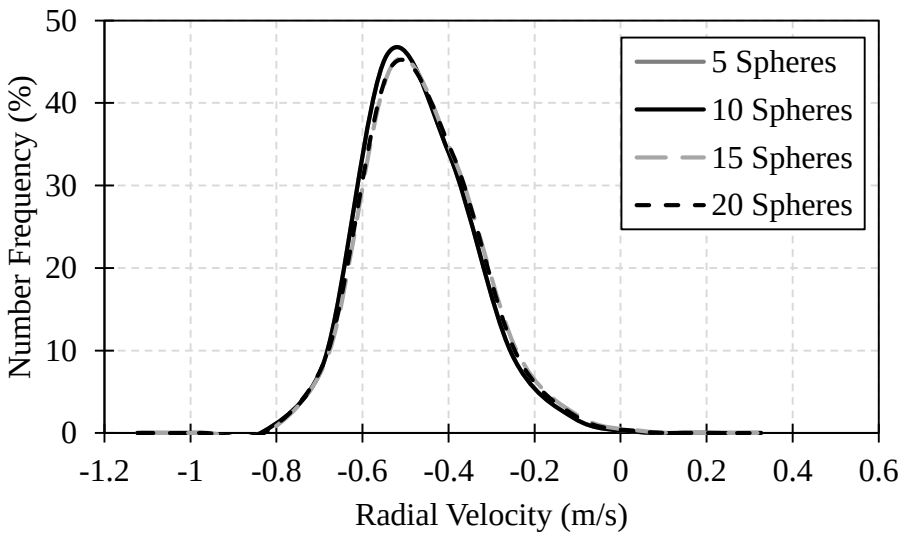

Figure 5.16: Predicted radial velocity distributions of particles in the measurement cells located after the baffle using the overlapping spheres method

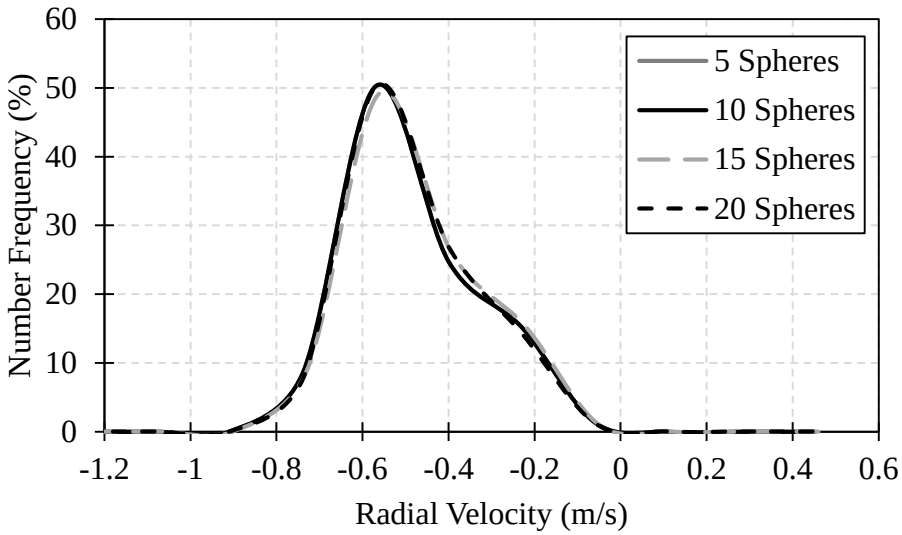

Figure 5.17: Predicted radial velocity distributions of particles in the measurement cells located before the baffle using the overlapping spheres method

A similar trend is also obtained for the tangential velocity distribution of the particles, as shown in Figure 5.18 and Figure 5.19. This clearly shows that the motion of particles is not sensitive to the number of spheres used to represent the particle shape in the DEM simulations of the seed coater in this study, as long as the general particle shape is represented. In this case five spheres was sufficient to represent the particle shape, however it remains to be seen if fewer clumped spheres can achieve this without the artificial use of the rolling friction. Moreover, the least number of clumped spheres can be used to accurately simulate this system in order to speed up the calculations.

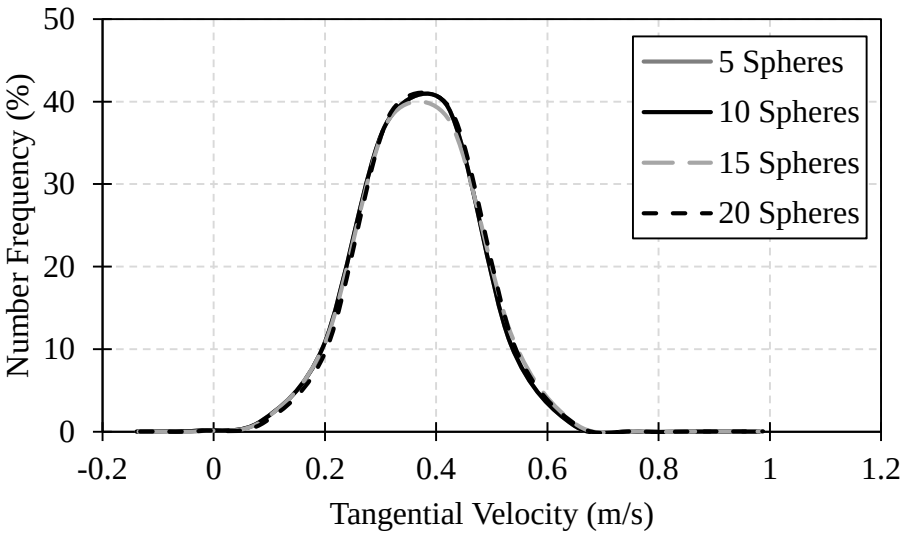

Figure 5.18: Predicted tangential velocity distribution of particles in the measurement cell located after the baffle using the overlapping sphere method

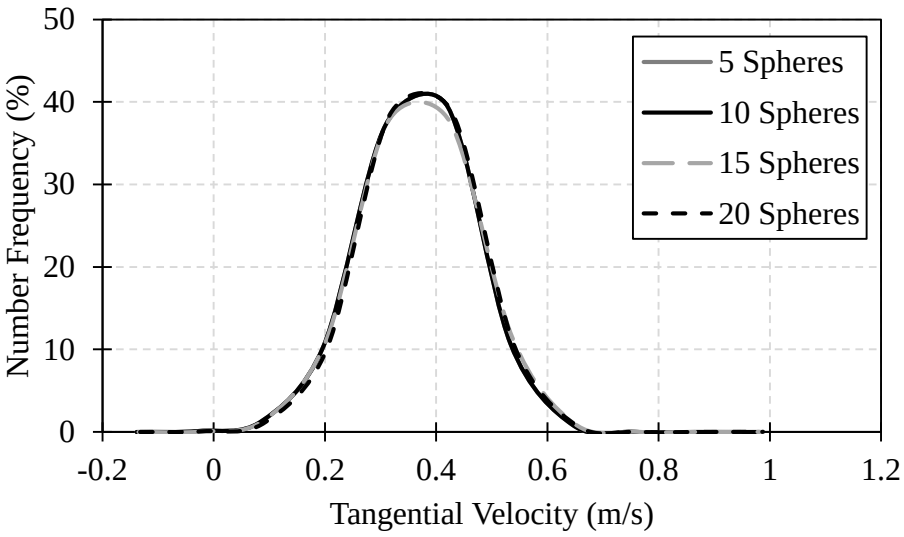

Figure 5.19: Predicted tangential velocity distribution of particles in the measurement cell located after the baffle using the overlapping sphere method

5.3 Comparison of Experimental Results and Simulation Predictions

The effectiveness of both methods is investigated by comparing the simulation predictions and experimental results. As there is no change in the tangential and radial velocity of particles when the number of clumped spheres is increased, the experimental results are compared for the simplest case, where the seeds are

represented by five clumped spheres. The radial and tangential velocity distributions of particles in the measurement cell located after the baffle are shown in Figure 5.20.

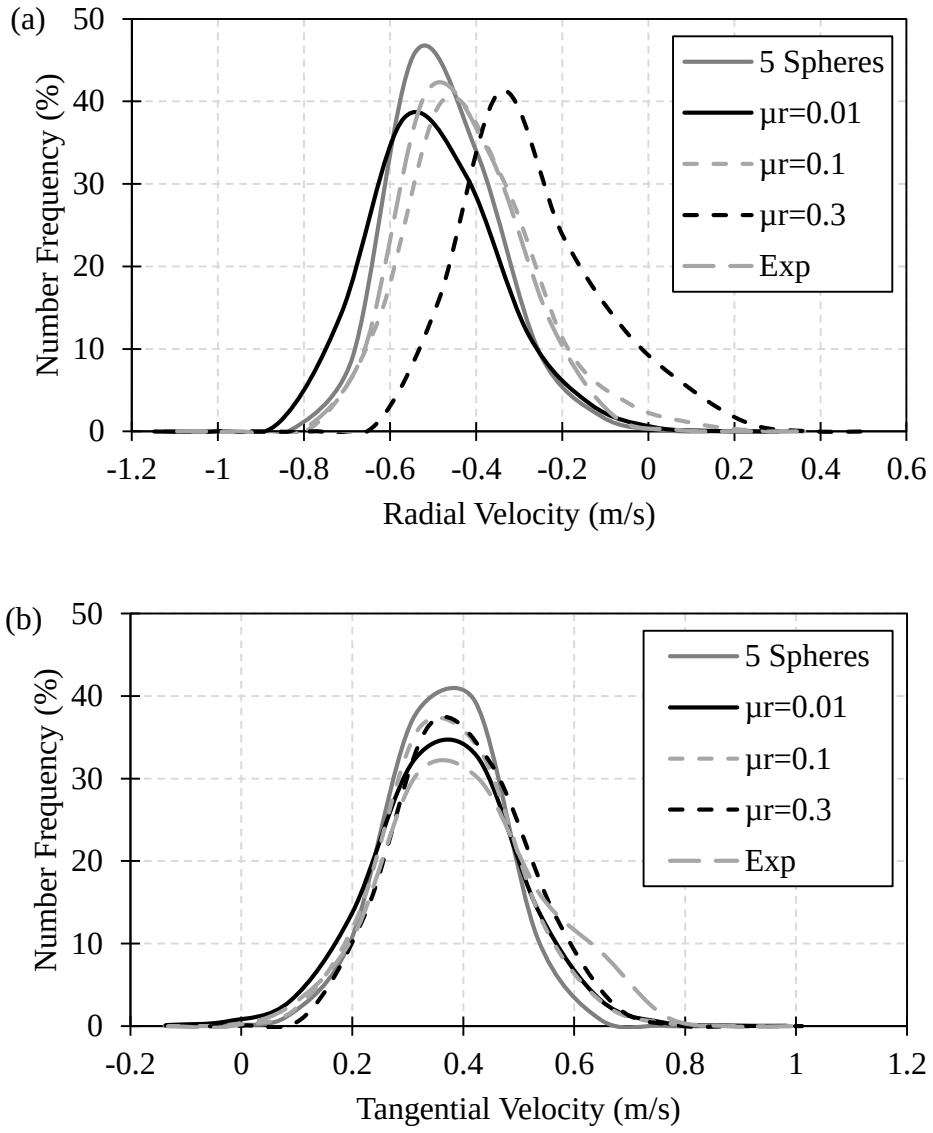

Figure 5.20: Comparison of experimental results and simulation predictions for the measurement cell located after the baffle: (a) radial velocity; (b) tangential velocity

In the case of radial velocity, the rolling friction coefficients of 0.01 and 0.3 provide a poor match to the experiments, whilst a rolling friction coefficient of 0.1 gives a reasonably good match. It can be seen that the DEM simulation of the seed coater using clumped spheres gives reasonably accurate prediction of the motion of particles. However, there is a slight lack of agreement on smaller values of magnitude of radial velocity and larger values of tangential velocity of the particles. This could be due to

the fact that some of the particles being tracked in the experiments were near the base of the coater; hence they tended to have larger tangential and smaller radial velocities. Moreover, it is clear that by using the rolling friction method, the motion of particles can be suitably simulated by DEM using a rolling friction coefficient of 0.1 (see the similarity between the velocity distributions using rolling friction coefficients 0.1 and experimental results in Figure 5.20). However, the value of this parameter is unknown a priori, so there is lack of predictability by this method.

It should be noted that the radial and tangential velocities of particles before the baffle could not be measured experimentally due to the complexity of particle motion. However, for the sake of comparison of the two methods, the velocity distributions of the particles before the baffle are compared using the methods of clumping multiple spheres and addition of rolling friction to spheres. A rolling friction value between 0.05 – 0.1 is representative of the motion of particles predicted using the clump sphere method as shown in Figure 5.21 and Figure 5.22. Average radial and tangential velocities of 0.58 and 0.42 m/s, respectively, are obtained for both methods of particle shape representation; however, the span of the distribution is slightly larger for the rolling friction method than the clumped sphere method. With the methodology established here the next step of addressing the quality of mixing is addressed using the clumped sphere method.

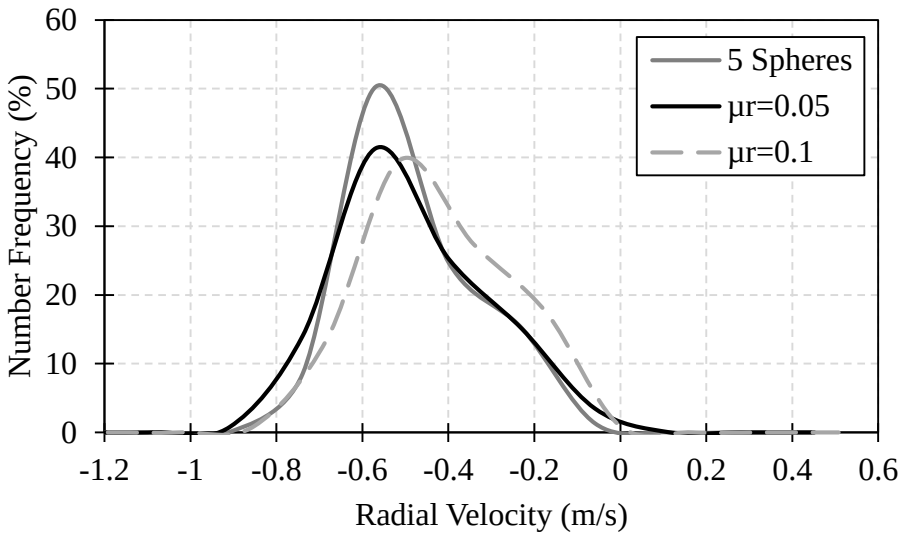

Figure 5.21: Comparison of radial velocity distribution of particles using clump sphere and rolling friction methods in DEM simulations

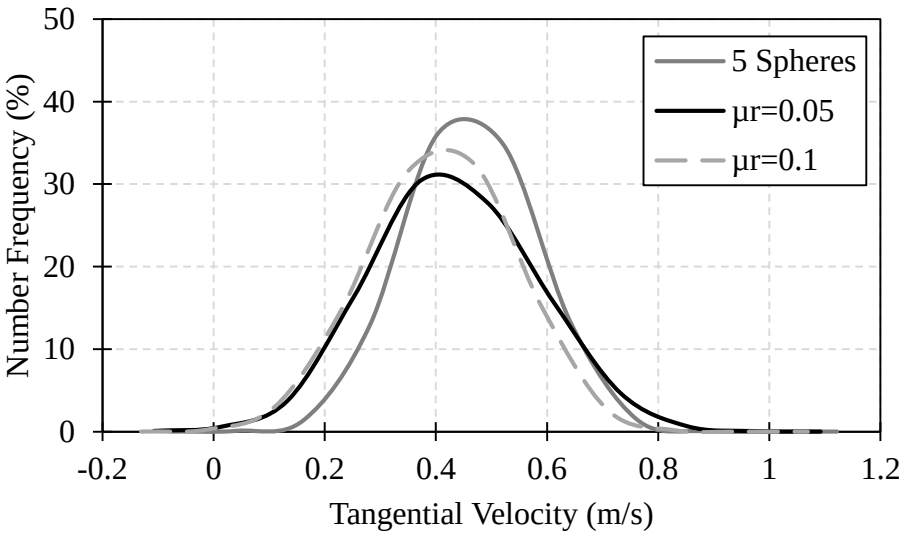

Figure 5.22: Comparison of radial velocity distribution of particles using clump sphere and rolling friction methods in DEM simulations

5.4 Concluding Remarks

The DEM results indicate that for simulating particle motion in rapid shear coaters, e.g. in the rotary batch seed coater investigated in this study, the motion of non-spherical particles can be simulated using clumped spheres or by controlling rolling friction. In the case of artificially changing the rolling friction of spherical particles, a reasonable agreement is found for both tangential and radial velocities for a narrow range of the chosen values. However, the motion of particles is slightly more sensitive to the value of rolling friction before the baffle, where there are more inter-particle contacts than after the baffle. It is also shown that the motion of particles can be predicted using the clumped sphere method. The number of spheres used to represent the particle shape is not critical for the range investigated. The work reported here suggests that clumped spheres provide a satisfactory representation of particle shape for rapid shearing systems with short collisional contacts. A small number of clumped spheres can provide a reasonable agreement with experimental results. Manipulating the rolling friction coefficient of single spheres can also provide results that closely match experiments to the clumped sphere method, but its most suitable value is unknown a priori, hence the approach is empirical rather than predictive.

CHAPTER 6 DEM Simulation of Coating Process

Coating of seeds is a common unit of operation in the seed processing industry. Particularly in corn seed coating, a large number of corn seeds are placed in a horizontal cylindrical drum, the base of the drum which is rotated around its vertical axis. A number of baffles are mounted inside the drum to enhance the axial and radial mixing of seeds. In the system investigated in this study, two baffles are placed in the drum, for which the angle, clearance gaps to walls and the base of coater can be adjusted. This enables better seed mixing to be achieved by optimising the process parameters; hence improving the inter-particle coating variability. The seed coating is done by a rotating atomiser disc where the coating liquid is fed on to the disk using a nozzle and the liquid is atomised at the edge of the atomiser disc, due to its high rotational speed and is spread to the surface of seeds bed. In seed coating, the coating formulation contains a large number of compounds, including fertilisers and pesticides. Due to health and safety risks while dealing with such liquids, de-ionised water is considered in this study as the coating liquid for measurement of droplets size, velocity and direction of movement. This enables a generic method to be established for investigation of such coating liquids in the future.

The SATEC ML2000 laboratory rotary batch seed coater (0.3 m in diameter and 0.1 m in height) is used in this study. This coater enables various process parameters such as baffles angle, clearance gap to the walls and base of coater, rotational speeds of base and atomiser disc distance to the base to be adjusted. In Chapter 5, the effect of particle shape on motion of particles was investigated and the appropriate type of shape for simulating the particle motion was chosen. In this chapter however, the coating model used to investigate the coating variability among the corn kernels is detailed and consequently the effects of various process parameters on coating variability of particles are presented.

6.1 Coating Contact Model

Spraying of coating liquid in this study is modelled by directly accounting for the spray droplets as solid particles. This is due to the fact that most of DEM software are designed for particle simulations and a spray description based on particles is closely aligned with reality, where the droplets size and velocity distributions can be

implemented in the simulations. Moreover, the spray pattern of the droplets can also be implemented by carrying out a number of experimental tests to achieve more realistic simulations. In our implementation, an additional particle properties termed "coating liquid mass" is introduced in addition to the existing properties for particles. In this model, similar to the model of Toschkoff *et al.* [69], the droplets are treated as solid particles with an exception in which the force calculation on droplets are ignored. The mass of the droplet particles are negligible in comparison to the corn seeds used in the simulations, hence would not have a strong influence on the momentum of corn seeds; it is therefore considered to be appropriate to ignore the force calculation on droplets to speed up the simulations. In addition, three criteria are used in the model to consider when the particle coating take in place. The droplet-droplet collisions are ignored and the contact detection is immediately proceeded to the next particle. This is considered to be appropriate in our study since it has a significant effect on the speed of simulations and the interest here is on the level of coating on particles rather than droplet-droplet interactions. Furthermore, since droplet velocities show little variation and move tangentially, the number of droplet-droplet collisions will be very low. However, it is possible to account for these collisions and establish the coalescence phenomena, but it is out of the scope of this work. In the case of droplet to corn kernel contacts, the mass of the droplets is added to the coating liquid mass of the corn kernels and the droplets are removed from the simulation. Similar to droplet-droplet collisions, force calculations are disabled, however, the contact detection remains in place. Similar collisional criteria is considered for droplet-wall collisions as for droplet-corn collisions. This criterion enables the use of larger simulation time-step; leading to faster simulations since large overlaps are allowed for droplet-particle and droplet-wall contacts. These collisional criteria are summarised in Table 6.1.

Table 6.1: Coating droplet collisional criteria in the proposed coating model

Collision Type	Description
Droplet-droplet	The collision is ignored; hence no contact detection and force calculation is considered and the calculation proceeds to the next particle.
Droplet-corn	The mass of the droplet is added to the coating liquid mass of the corn kernels and the droplet is removed from the simulation. No force calculation is carried out.
Droplet-wall	The mass of the droplet is added to coating liquid mass of the wall and the droplet is removed from the simulation. No force calculation is carried out.

In addition to the coating contact model, Hertz-Mindlin contact model with rolling friction based on viscous dissipation is used for simulating inter-particle interactions, as discussed in Section 2.3.3. It has to be noted that the effect of stickiness of coating liquid is neglected in this work since this is out of the scope of this study.

6.2 Implementation of Droplet Generation in DEM Simulations

In order to incorporate the coating liquid droplets into DEM simulations, a series of high speed video recordings are carried out to measure the droplet size and velocity distributions once they are released from the atomiser disc. To do so, the flow rate of the de-ionised water was fixed at 160 ml/min. The droplets were observed using a Redlake HG-100K high-speed video camera. The camera setup is shown in Figure 6.1.

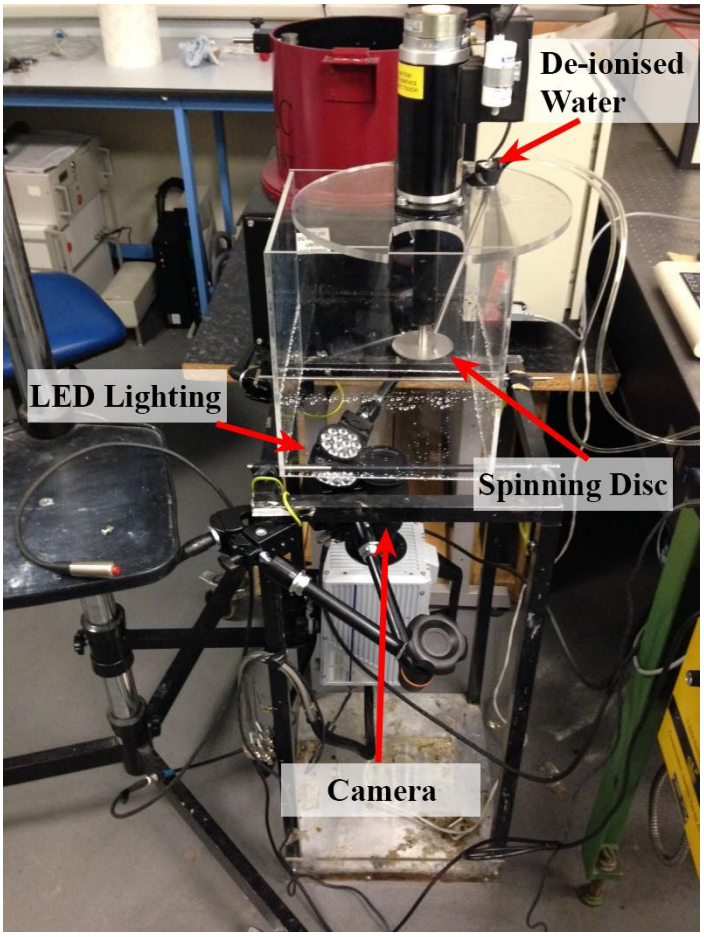

Figure 6.1:High-speed camera setup for measuring droplets size and velocity

The size of each droplet at each video frame (every 5 ms) is calculated based on the number of pixels they contain in the image. This is carried out over a period of 10 seconds. The droplets smaller than 50 microns in diameter are excluded in the analysis due to the resolution of captured images as they don't contain an adequate number of pixels (e.g. less than 5 pixels in diameter) and they could represent the noise in the acquired images. The magnitude of droplets velocity is calculated from the travelled distance of each droplet between the consecutive video frames (500 µs). The droplets size and velocity distributions are shown in Figure 6.2 and Figure 6.3, respectively.

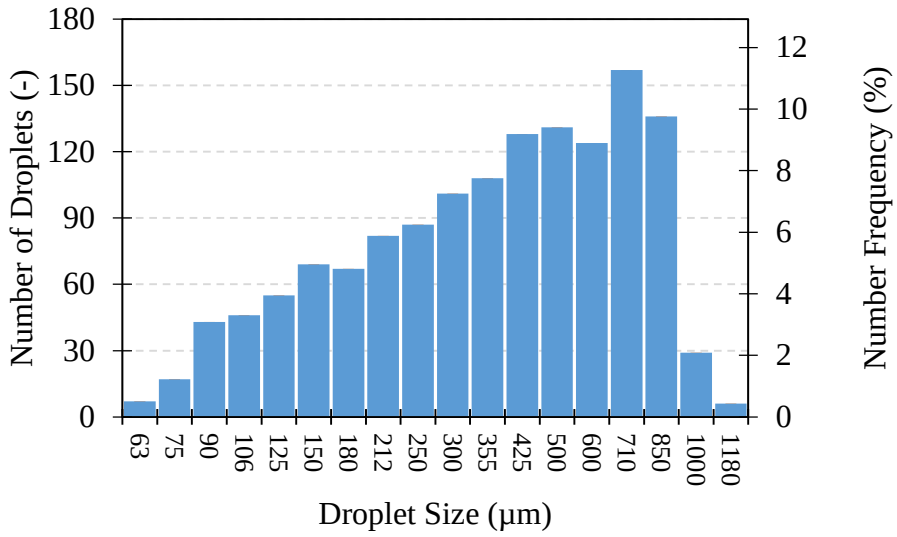

Figure 6.2: Measured droplet size distribution using high-speed video imaging

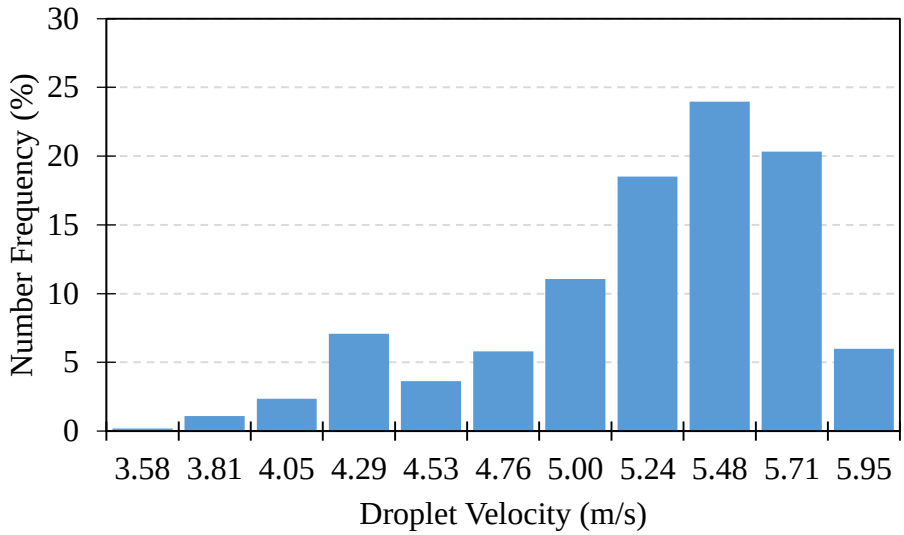

Figure 6.3: Measured droplet velocity distribution using high-speed video imaging

As it can be seen from the above figures, the de-ionised water droplet size and velocity distributions have peak values at 710 µm and 5.48 m/s, respectively. The droplet velocity distribution has a wide span, which could be due to the wide size distribution of generated droplets from the atomiser disc. For accurate representation in the DEM, it is important to understand the directional motion of the droplets once they are released from atomiser disc. Hence, a series of high-speed video recordings were carried out and it was found that the droplets tend to move tangentially relative to the

edge of the atomiser, as shown in Figure 6.4, which shows the tracked positions of some of the droplets after being released from the atomiser disc.

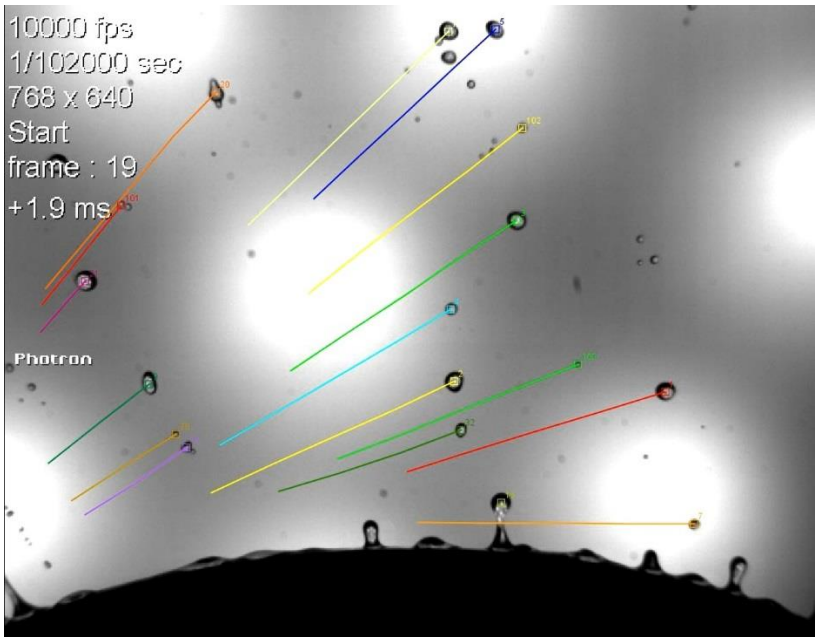

Figure 6.4: Motion of de-ionised water droplets after being released from the atomiser disc. The coloured lines showing the tracked position of droplets in the high-speed video images.

Based on the gained knowledge on size and velocity distributions and direction of motion of the droplets, a custom body force contact model is implemented for EDEM software for generation of droplets. A ring-shaped virtual geometry, as shown in Figure 6.5, is considered as the particle factory for initial generation of droplet particles. The droplets are randomly generated inside the particle factory geometry and at the first time step of generation of each droplet, an initial tangential velocity is given. EDEM custom application program interface (API) only supports inputting particle acceleration; hence the acceleration required to achieve the desired particle velocity by the end of the time-step is calculated in the code and applied to the droplet. The schematic diagram of how the droplets are generated in the proposed model is shown in Figure 6.6. The effect of gravitational force on the droplets is also neglected in order to retain their velocity magnitude. This process is repeated for the consecutive generated droplets in the droplet factory.

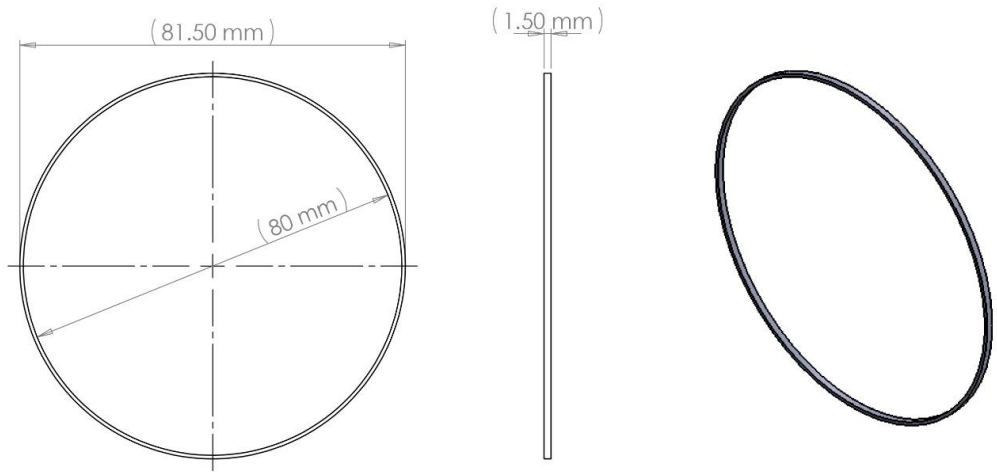

Figure 6.5: Geometry of droplets factory used in DEM simulations.

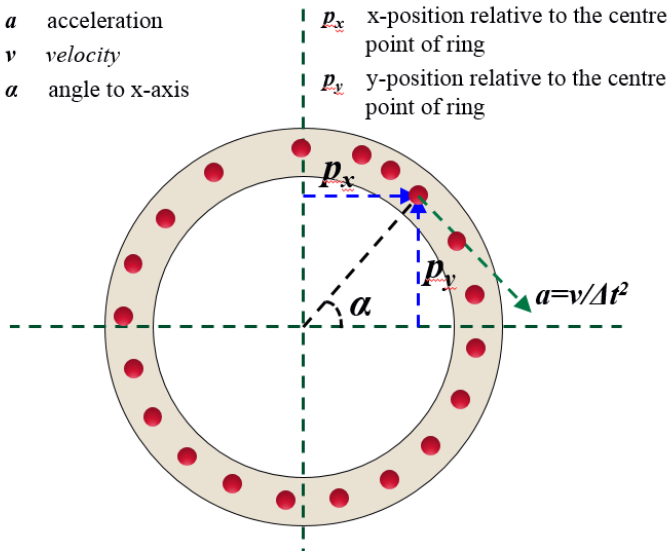

Figure 6.6: Schematic representation of droplet generation and motion of the droplets being released from the atomiser disc in DEM simulations.

In DEM simulations the rate of generation of droplet particles is chosen to equal that used in experiment. For all the simulations in this study, the flow rate of the de-ionised water were controlled by an automatic syringe pump, and is set to 160 ml/min which corresponds to 2.67 g/s by considering the density of de-ionised water.

6.3 Effect of Process Parameters on Coating Uniformity of Corn Kernels

In the previous section, we detailed the coating contact model proposed for this study where the liquid droplets are considered as solid particles. The proposed model is

used here to investigate the effect of various process parameters on coating uniformity of corn kernels. The process parameters are divided into two main categories based on (i) their effect on dynamics of motion of the kernels (i.e. baffle angle, clearance gap to walls of coater, design and base rotational speed) and (ii) coating mechanism (atomiser position and spraying mechanism). These process parameters are identified to be the key influential parameters on coating uniformity of seed kernels for the studied system.

6.3.1 Baffle Angle and Clearance Gap to the Walls

In order to investigate the effect of baffle angle and clearance gap to the walls on the coating uniformity of corn kernels, systematic simulation setups are considered where both parameters are varied over a range of for each process parameters. In our study, the baffles angle and clearance gap to the walls was varied from 25 to 55° and 5 mm to 20 mm, respectively. The latter was considered such that it represents a clearance gap to the wall corresponding to approximately 1 to 4 corn seed diameters. The definition of how the angle and clearance gap is interpreted is shown in Figure 6.7.

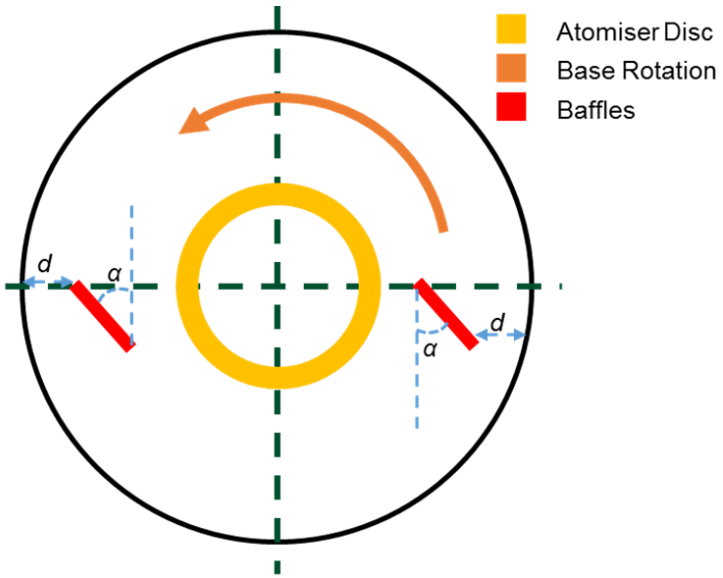

Figure 6.7: Schematic representation of baffle angle and clearance gap to the walls in the DEM simulations where *α* and *d* are the baffle angle and distance to the coater wall.

Based on this, 16 DEM simulations were considered, as shown in Table 6.2.

Table 6.2: Baffle angles and clearance gaps arrangements used in DEM simulations.

	Baffle Angle (°)

		25	35	45	55
Clearance Gap (mm)	5	✓	✓	✓	✓
	10	✓	✓	✓	✓
	15	✓	✓	✓	✓
	20	✓	✓	✓	✓

For all the cases mentioned above, the coater base rotation speed, atomiser disc distance to the base and flow rate of coating droplet were kept constant at 300 rpm, 30 mm and 160 ml/min, respectively. The coating simulations where carried out for 25 s of real time operation using a typical baffle design, as shown in Figure 6.8, and the coating uniformity of the particles were analysed by coefficient of variation of coating mass of particles in the system. This coating time was considered reasonable since the CV of coating mass is reached a relative asymptotic level and is typically used for industrial scale coaters, as shown in Figure 6.9.

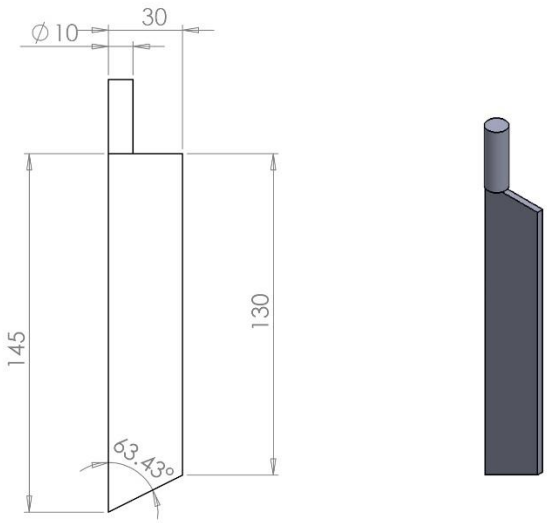

Figure 6.8: Schematic diagram of the original baffle design used for DEM simulations.

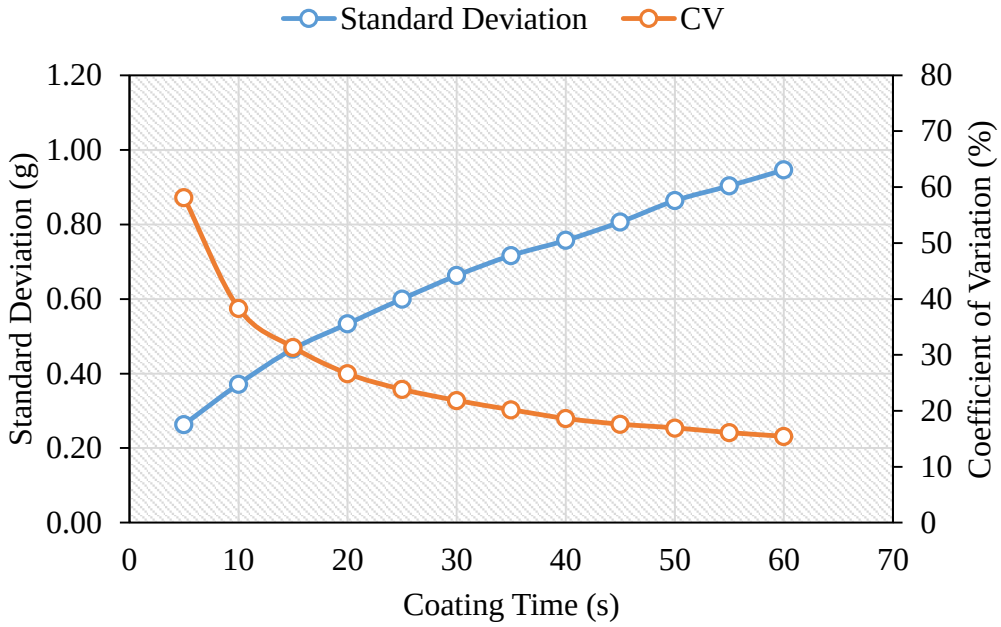

Figure 6.9: Standard deviation and CV of coating mass of corn kernels as a function of coating time for baffle angle and clearance gap of 45° and 15 mm, respectively.

The effect of baffle clearance gap to the walls of coater is shown in Figure 6.10. For all cases, the coating variability of particles is reduced as the clearance gap is increased and once this gap is increased further from the optimum value, the coefficient of variation of coating mass increases. It is evident that there is an optimum baffle clearance gap of 15 mm for the investigated system here since the CV decreases as the gap is increased to 15 mm, then increases above this. This optimum clearance gap remains constant for all baffle angles investigated here. The optimum clearance gap of 15 mm represents approximately two to three particle diameters. The difference between the two extreme cases of clearance gap is considered significant, where 5 percent of improvement in terms of coating uniformity is achieved by optimising the clearance gap.

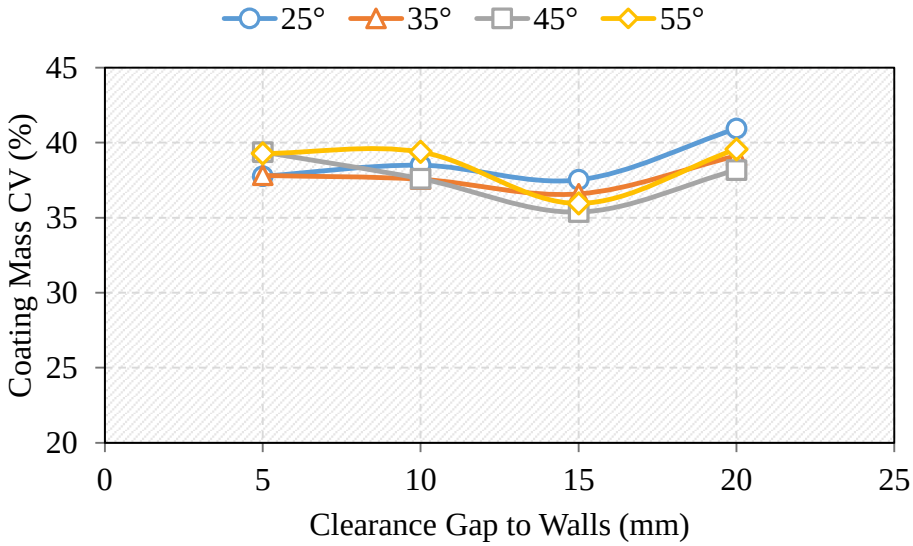

Figure 6.10: Effect of baffle clearance gap to the walls of the coater on coating uniformity of corn kernels

The above analysis can also be interpreted in terms of the effect of baffle angle on coating uniformity, as shown in Figure 6.11. In general, the coating uniformity of corn kernels is improved by increasing the angle of baffles relative to the y-axis of the system to 35 – 45 ° and once a baffle angle of 45° is exceeded, CV of the coating mass is increased. However, in the case of a 5 mm clearance gap, the optimum baffle angle was found to be 25 °.

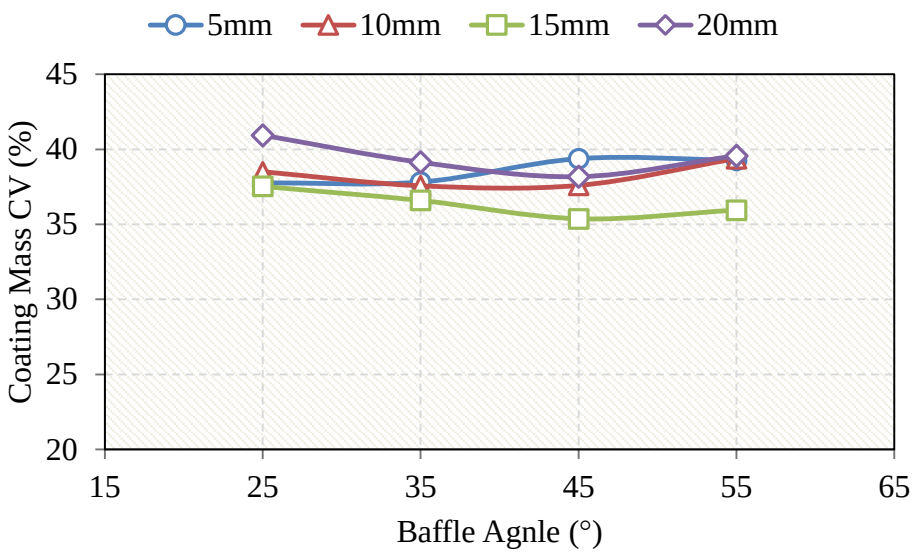

Figure 6.11: Effect of baffles angle on coating uniformity of corn kernels in DEM simulations

Using the above analysis, it can be concluded that optimum values of baffle angle and clearance gap to the wall of the coater are 45° and 15 mm, respectively, where the coating uniformity of corn kernels can be improved by 7% between the two extremes. The clearance gap is believed to control the proportionality of the surface that is renewed after each circulation of base, since this parameter controls the thickness of the particle layer being sliced off from the bed surface. Moreover, the baffle angle controls the direction and the position of the particles being sliced from the bed. In overall, these two parameters are believed to control the surface renewal rate of the bed which directly influences the coating uniformity of corn kernels since only the particles at the surface receive coating liquid.

6.3.2 Effect of Baffle Design on Coating Uniformity

In addition to baffle angle and clearance gap to the walls, surface renewal rate and motion of particles after being sliced off from the surface depend on the shape of the baffles; hence a number of baffle designs were proposed to investigate the influence of baffle shape. For this, three key features of the shape were considered: curvature, width and geometry. For curvature of the baffle, two cases are considered, flat and curved faces and three baffle widths are considered for each, as shown in Figure 6.12.

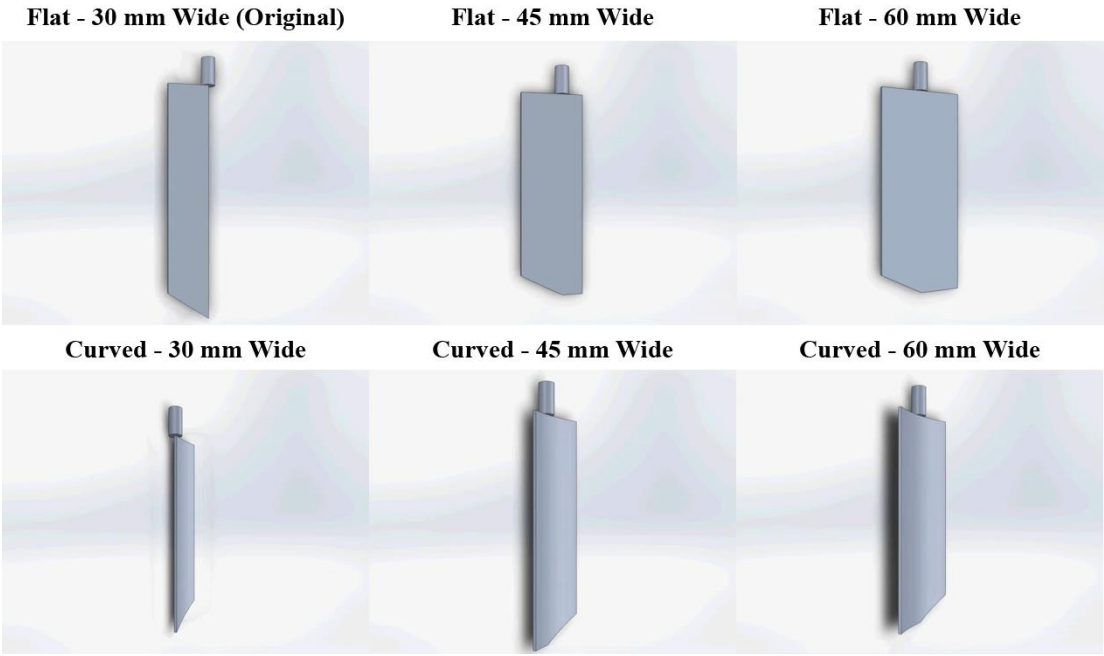

Figure 6.12: Baffles design used for investigation of effect of baffles width and face curvature on coating uniformity of corn kernels in DEM simulations.

In order to be able to compare the results, all other simulation parameters such as position of atomiser disk, base rotation speed and total mass input were kept constant and the optimum baffle angle and clearance gap to the walls are used.

The same approach for analysing coating uniformity of particles as summarised in Section 6.3.1 is considered here. The uniformity of coating for the proposed baffle designs are shown in Figure 6.13. It is clear that the effect of baffle width on coating uniformity of corn kernels for all the investigated cases is not singificant. However, in the case of the curved baffles, a baffle width of 45 mm improves inter-particle coating uniformity by approximately 1 and 2% compared to widths of 30 and 60 mm, respectively. Comparing the flatness and curvature of the baffles, it can be concluded that the curvature of the baffle does not strongly influence the coating uniformity; however, the curved baffle with a width of 45 mm results in a slightly lower coefficient of variation than the original flat baffle.

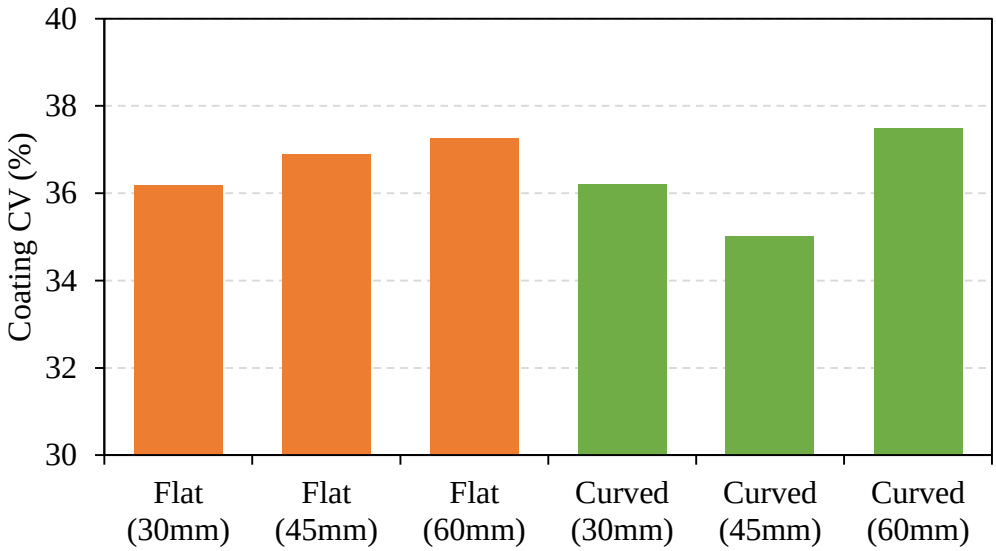

Figure 6.13: Effect of flatness and curvature of baffles on coating uniformity of corn kernels in DEM simulations

In order to understand the effect of baffle shape, a cross section plot of particles being sliced from the bed surface is plotted and shown in Figure 6.14 where each data point represents the centre point of each particle in the DEM simulation with the original baffle and angle and clearance gap of 45 ° and 15 mm, respectively. It is clear that by fixing the baffles clearance gap and angle, regardless of the width and curvature of the baffles, the proportionality of particles being sliced off from the surface of the bed is more or less similar.

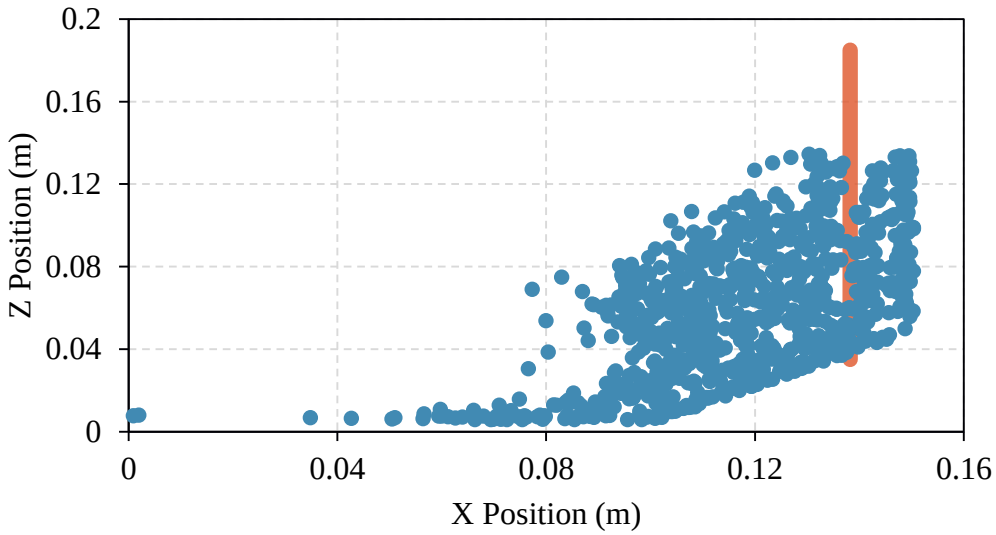

Figure 6.14: Cross section view of corn kernels being sliced off from the bed surface as they approach one of the baffles at angle and clearance gap of 45° and 15 mm, respectively; each data point represents the centre point of a corn kernels and the orange line represents the position of the baffle.

From the analysis above it is clear that the baffle curvature and width affect the motion of particles after passing the baffles, rather than influencing the surface renewal rate. A new baffle design was proposed, as shown in Figure 6.15, which changes the proportionality of particles being sliced off from the surface of the bed approaching the baffles. In this case, the baffles are designed to cut the surface of the bed at different angle compared to the original baffle design; hence changing the proportionality of particles being sliced off from the bed surface.

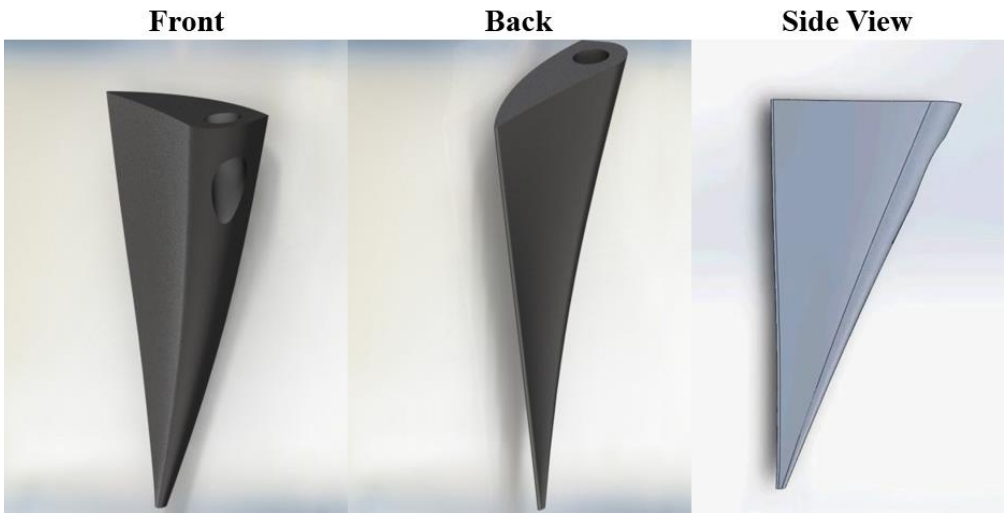

Figure 6.15: New baffle design for controlling the proportionality of particles being sliced off from the bed surface.

A comparison is made between the new baffle design and those investigated previously, where the coefficient of variation of particles coating mass is plotted in Figure 6.16. It can be seen from the figure that using the new baffle design, the particles coating uniformity has improved by 5%. This improvement is mainly due to the fact that the fraction of particles that being sliced off from the surface of the bed is changed; hence influencing the surface renewal rate of the particles. In order to understand this, a comparison is made between the flat and new baffle designs, where position of particles approaching the baffles in a cross sectional plot is shown (Figure 6.17). It is evident that the new baffle design is more successful in slicing the particles on the surface of the bed in comparison to the original baffle design.

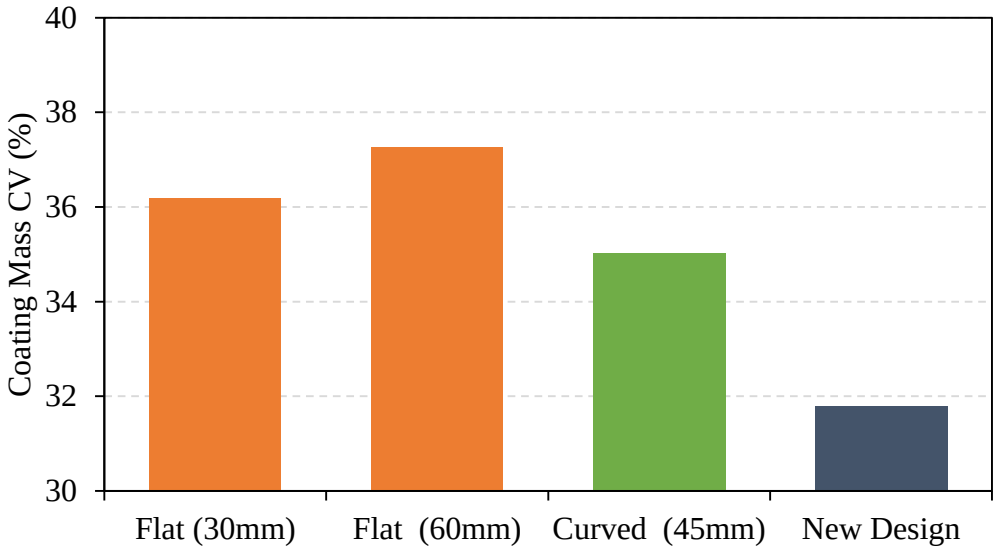

Figure 6.16: Effect of baffles shape on coating uniformity of corn kernels in DEM simulations.

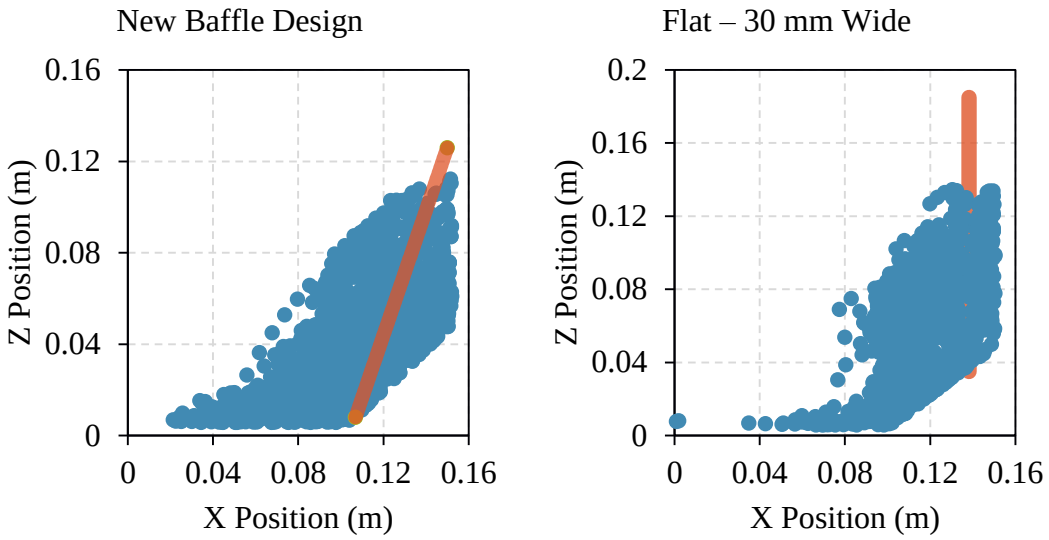

Figure 6.17: Cross sectional view of position of corn kernels approaching the baffle.

6.3.3 Effect of Atomiser Disc Vertical Position

In previous sections, the focus was on the effect of various baffle parameters, such as angle, clearance gap and shape which mainly affect the dynamics of motion and new surface generation of bed passing by the baffles. In this section, however, the focus is on the effect of the position of the atomiser disc. The position of atomiser disc relative to the base of the coater defines the proportion of particles being coated on the surface of bed. Since the coating droplets are generated using a rotating disc atomiser rather than a sprayer, a thin layer of droplets are generated. Hence, it is expected that the position of the disc influences the coating variability of particles. A series of DEM simulations was carried out by varying the vertical position of atomiser disc relative to the base of the coater from 30 to 70 mm, using the flat design baffle with clearance gap and angle of 15 mm and 45°, respectively. A schematic representation of the position of the atomiser disc is shown in Figure 6.18.

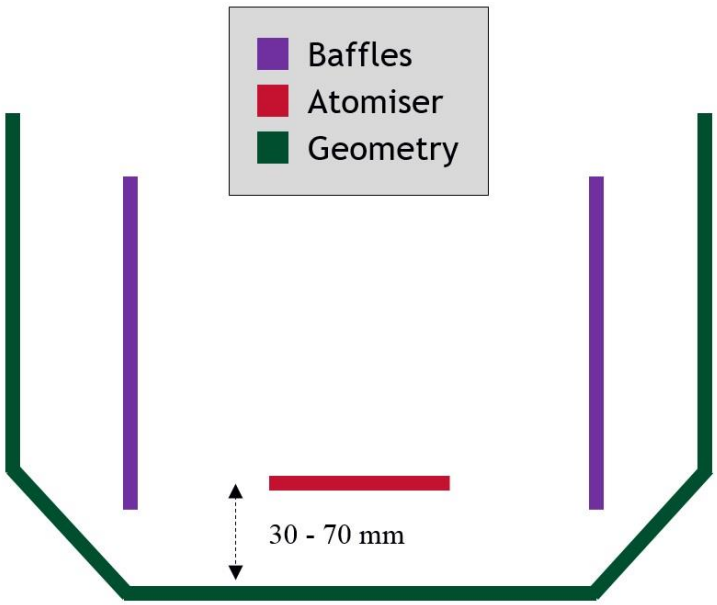

Figure 6.18: Schematic representation of atomiser disc position relative to the base of the coater.

A series of DEM simulations was carried out for calculating the particles coating mass coefficient of variation using the proposed vertical position of atomiser disc, as shown in Figure 6.19. It is evident that there is an optimum vertical position for the atomiser disc, 50 mm from the base, leading to the lowest coating mass coefficient of variation. Initially, the coating uniformity of the particles improves as the vertical position is increased, and once a vertical distance of 50 mm is exceeded, it starts to deteriorate (CV increases). Comparing the optimised vertical position of the spray disc (50 mm) with the initial position used in earlier simulations in previous sections (30 mm), the position of the disc relative to the base of coater has a noticeable influence on coating variability of the particles and approximately a 5% improvement of coating variability is achieved as shown in Figure 6.19. Hence, it can be concluded that this process parameter is one of the key influential parameters in the coating process using this type of drum coater.

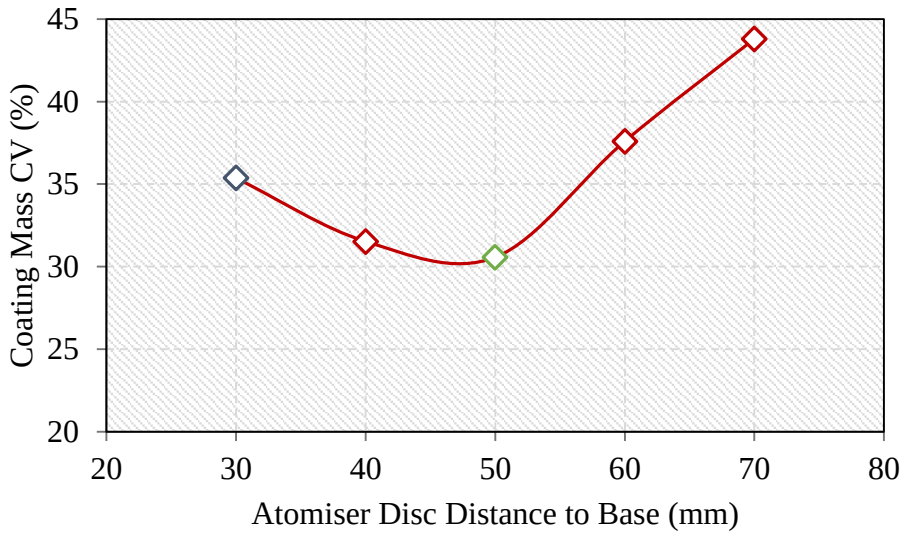

Figure 6.19: Effect of vertical position of atomiser disc relative to the base of coater on coating uniformity of corn kernels in DEM simulations; the blue and green data points represent the original and optimised position of atomiser disc, respectively.

6.3.4 Effect of Base Rotational Speed on Coating Variability

In addition to dynamics of coating droplet generation and surface renewal rate, the number of coating events (number of bed turnovers) is expected to influence the coating variability of the particles in the process. In general, a higher number of rotations should lead to a higher probability of new and less coated particles being available at the surface of the bed. Thus, leading to higher probability that all particles will be more uniformly coated in the system. It is expected that a minimum number of bed turnovers is required to let all the particles become coated. However, a too high rotational speed would lead to higher impact velocity of particles to the baffles which may damage both the particles and their coating. In this study, the intention was to focus on the coating variability of particles rather than the damage on their coating; hence the potential damage to the coating of the seeds is disregarded. Using the SATEC ML2000 coater, the rotational speed of the coater base can be controlled (200 – 700 rpm) and a range of rotational speeds for the base is considered to investigate the effect of this parameter on coating variability of the particles. The particles coating mass coefficient of variation as a function of base rotational speed is shown in Figure 6.20. It can be seen that, increasing the speed improves the coating uniformity of the particles; however the extent of improvement of coating uniformity compared to the range of speeds investigated here is negligible.

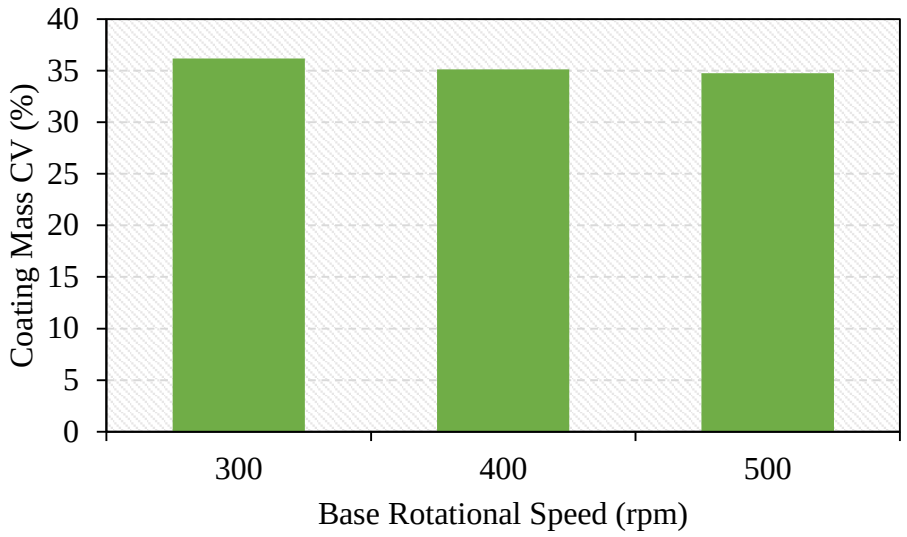

Figure 6.20: Effect of base rotational speed on coating variability of corn kernels in DEM simulations.

6.3.5 Concluding Remarks

The effect of various process parameters on coating variability of corn kernels was investigated using DEM simulations. A new coating contact model was proposed to calculate the coating mass coefficient of variation which directly represents the inter-particle coating variability of the particles. In the proposed model, the coating droplets were represented as small solid particles and once they come into contact with the corn kernels, their mass is stored in the corn kernel's coating mass parameter, and they were removed from the simulation. It was shown that using this model the amount of the coating on each particle can be tracked; hence useful information such as distribution of coating mass among the particles and coefficient of variation of coating mass of the particles can be assessed. Among the proposed process parameters, it was found that the position of the atomiser disc relative to the base of coater, the geometric shape of baffles and baffles clearance to the walls strongly influence the coating uniformity of the particles. In the case of baffle geometric shape, a new baffle design was proposed were an improvement of approximately 5% in terms of coating mass coefficient of variation compared to the original baffle design provided with the coater is achieved. Moreover, it was found that the position of atomiser disc plays an important role on improving the coating uniformity of particles and a vertical clearance of 50 mm with the base of the coater decreased the particles coating mass coefficient of variation by 5% compared to the original position of the disc. In the case of baffle clearance to the

walls, it was found that using the flat baffle design a clearance gap to the wall of 15 mm provides the lowest inter-particle coating variability compared to small and large clearance gaps. An improvement of approximately 7% was achieved between the optimised and worst case combination of baffle angle and clearance gap investigated in this study. On the other hand, it was found that the rest of process parameters (e.g. baffles angle, curvature, width and base rotational speed) had insignificant effects on coating uniformity of the particles where only a 1 – 2 % change in coating mass coefficient of variation was observed.

CHAPTER 7 Conclusions and Recommended Future Work

7.1 Conclusions

The overall aims of this PhD were to further understand the coating uniformity of the corn kernels in a typical seed mixer and tailor the existing methodologies for assessing the extent of breakage of powders under shear deformation to agricultural seeds.

Distinct Element Method simulations were considered for analysing the uniformity of corn seed coating mass, since it reveals a wide range of information about the processes that are either expensive or impossible to be obtained experimentally. In traditional DEM simulations, spheres are used to represent the particles in the process. However, in this study it was shown that although the surfaces of corn seeds are smooth, they are relatively non-spherical and at the single particle level the motion of the seeds upon impact onto a flat stainless steel platen is dependent on the orientation and shape of the corn seeds. Hence the need for implementation of particle shape into DEM simulations was needed.

Two commonly used methods of incorporation of particle shape in DEM simulations were considered: i) manipulating rolling friction coefficient of spheres and ii) clumping multiple spheres to form a single particle. The former is considered an empirical approach since rolling friction coefficient does not represent a physical property of a material and cannot be measured experimentally, whilst the shape of the particles can be acquired using various imaging techniques such as XMT. Therefore, an extensive work was carried out to compare the accuracy of the two mentioned methods. For acquiring the shape of corn kernels, the XRT technique was used and consequently ASG2013 software was used to generate the shape of the kernels by clumping multiple spheres together. The accuracy of the generated shape was also investigated by controlling the number spheres (5 – 20) used in the clumped sphere assemblies. In the case of manipulating the rolling friction coefficient of spheres, a wide range of values (0.01 – 0.3) was used.

For evaluation of the accuracy of the DEM simulations using the mentioned approaches, high speed video imaging was used to measure the radial and tangential

velocity distributions of corn kernels in the mixer, experimentally. The obtained velocity distributions were then compared to those calculated from DEM simulations. For comparison, a measurement cell located after the baffle was considered for both experiments and simulations. In DEM simulations, a measurement cell before the baffle is also considered, where the number of inter-particle contacts before the baffle was found to be greater than after the baffle by the DEM analysis. It was shown that the tangential velocity distribution of the corn kernels in both measurement cells was sensitive to the value of rolling friction coefficient. However, the radial velocity distribution of the kernels was relatively insensitive for the range of chosen values. It should be noted that rolling friction coefficients beyond this range are unrealistic. In the case of clumped sphere method, however, it was found that the velocity distributions of the kernels were not sensitive to the number of spheres used in the clumped spheres assemblies; suggesting that for the system investigated here the accuracy of shape representation does not significantly influence the flow of the kernels, as long as the general shape of kernels is preserved. Comparing the obtained results from DEM simulations and those measured experimentally, it was concluded that both methods can provide a satisfactory result for simulating the motion of the particles in the mixer where a small number of clumped spheres can provide a reasonable agreement with experimental results. Equally well, manipulating the rolling friction of spheres can also provide that closely match experiments. However, the most suitable value of rolling friction coefficient is unknown *a priori*, hence the approach is considered empirical rather predictive.

For assessing the coating uniformity of the corn kernels in DEM, a new coating contact model based on model of Toschkoff *et al.* [69] was used. In the model, the spraying of coating liquid is modelled by directly incorporating the spray droplets as solid particles, since a spray description based on particles is closely aligned with reality. The size and velocity distributions of the droplets, once released from the atomiser disc, were measured experimentally and implemented in the simulations.

The assessment of variation of inter-seed coating mass was done by considering the coefficient of variation of coating mass on the corn seeds. It was shown that by increasing the coating time, the coating uniformity of the corn kernels was improved and after 25 seconds it reached an almost asymptotic level. The effects of various process parameters on the kernel's coating mass coefficient of variation were also

investigated. It was shown that the baffle angle and base rotational speed of the mixer do not strongly influence the coating uniformity of the corn seeds, whereas the baffle design, clearance gap to the walls and atomiser disc position relative to the base of the coater strongly influence the coating variability of the corn seeds.

In the simulations of the seed mixer, it was shown that by changing the dynamics of slicing the seeds on the surface of the bed, by changing the shape of the baffles and position of the atomiser disc, the coating variability of the seeds can be significantly improved. Various aspects of baffle's shape were considered: (i) curvature, (ii) width and (iii) geometry. It was concluded that the geometry of the baffle is the most influential factor on coating uniformity of the corn kernels, since it changes the proportion of the bed being diverted to reveal new bed surface for coating. However, the curvature and width of the baffles did not have a significant effect of coating uniformity of the corn kernels. Similar to the effect of the geometry of the baffle, a significant effect was found for the position of the atomiser disc relative to the base of the mixer. The proposed coating model and the sensitivity analysis of the effect of the process parameters helps to determine the dynamics of the coating process in the investigated seed mixer and optimise the key influential process parameters for improved coating uniformity.

An annular shear cell was used to assess the extent of breakage of turnip and corn seeds under shear deformation. Most work reported in the literature is mainly on pharmaceutical powders, hence the existing methods for assessing particle breakage were modified to be tailored for agricultural seeds. Turnip seeds were initially used to develop the appropriate methodology for breakage assessments. Four breakage criteria were proposed to reflect the definition of broken seeds. Based on the work done by Hare [29] and Neil and Bridgwater [25] on assessment of extent of breakage of various powders, the size of damaged particles after shearing was considered to be in the range of two sieve-cuts below the feed particle size. However, our study showed that the extent of breakage of agricultural seeds has to be assessed slightly differently, where any seeds below the feed size material are considered to be damaged. Hence, the extent of breakage was assessed based on the mass of broken seeds collected below the feed material sieve-cut size. This is due to the fact that any physical damage to the seeds would lead to loss of their germination potential. The proposed methodology was improved further by inspecting individual seeds under microscope to identify the

damaged particles that remained in the feed size sieve-cut. Comparing these criteria, both lead to relatively similar results, whilst the former should much faster to perform. Hence, a strategic decision is required for which criterion be considered for assessing the extent of breakage of agricultural seeds.

7.2 Recommended Future Work

The proposed model for simulating the coating of particles does not consider the interaction of coating droplets and particles. Addition of coating liquid on the surface of particles would affect the surface adhesion of the particles. Hence, for more realistic simulations, the effect of particles adhesion should be considered in the future. As mentioned in Section 6.1, the inter-droplet interactions are ignored in the proposed model, however future work can add this to the model. Furthermore, in this work the coating liquid used assumed to instantaneously spread across the surface of a given seed. In reality liquid droplets would remain on the surface of a seed, with the rate and degree of spreading depending on the liquid viscosity, surface tension and wetting angle. The collisions between corn seeds would lead to seed to seed coating liquid transfer. Such an approach would be necessary for systems where the drying time of the coating liquid is not so short.

Although the motion of corn seeds are validated with experimental results, there is a lack of validation on the coating contact model. Hence, the proposed model can be validated by experimentally coating the surface of the corn seeds in the mixer and comparing the variation of coating mass with those calculated in DEM simulations by either chemical or image analysis techniques.

References

[1] ICRISAT. Genebank Manual [Internet]. Topics, International Crops Research Institute for the Semi-Arid. [cited 2012 Aug 3]. Available from: http://www.icrisat.org/gene-bank-manual.htm

[2] Ghadiri M, Zhang Z. Impact Attrition of Particulate Solids . Part 1 : A Theoretical Model of Chipping. Chem Eng Sci. 2002;57(17):3659–69.

[3] Ahmadian H, Ghadiri M. Analysis of Enzyme Dust Formation in Detergent Manufacturing Plants. Adv Powder Technol. Society of Powder Technology Japan; 2007 Jan 1;18(1):53–67.

[4] Ghadiri M, Ning Z, Kenter S., Puik E. Attrition of Granular Solids in a Shear Cell. Chem Eng Sci. 2000 Nov;55(22):5445–56.

[5] Ning Z, Ghadiri M. Distinct Element Analysis of Attrition of Granular Solids Under Shear Deformation. Chem Eng Sci. 2006 Sep;61(18):5991–6001.

[6] Paramanathan BK, Bridgwater J. Attribution of Solids—I : Cell Development. Chem Eng Sci. 1983;38(2):197–206.

[7] Wiącek J, Molenda M, Horabik J, Ooi JY. Influence of Grain Shape and Intergranular Friction on Material Behavior in Uniaxial Compression: Experimental and DEM Modeling. Powder Technol. Elsevier B.V.; 2012 Feb;217:435–42.

[8] González-Montellano C, Fuentes JM, Ayuga-Téllez E, Ayuga F. Determination of the Mechanical Properties of Maize Grains and Olives Required for Use in DEM Simulations. J Food Eng. 2012 Aug;111(4):553–62.

[9] Boac JM, Casada ME, Maghirang RG. Material and Interaction Properties of Selected Grains and Oilseeds for Modeling Discrete Particles. 2010;53(4):1201–16.

[10] Coetzee CJ, Els DNJ. Calibration of Discrete Element Parameters and the Modelling of Silo Discharge and Bucket Filling. Comput Electron Agric. 2009 Mar;65(2):198–212.

[11] Coetzee CJ, Els DNJ, Dymond GF. Discrete Element Parameter Calibration and the Modelling of Dragline Bucket Filling. J Terramechanics. ISTVS; 2010 Feb;47(1):33–44.

[12] Grima AP, Wypych PW. Development and Validation of Calibration Methods for Discrete Element Modelling. Granul Matter. 2010 Jul 23;13(2):127–32.

[13] GeoPyc 1360 Envelope Density Analyzer | Micromeritics [Internet]. [cited 2012 May 4]. Available from:

http://www.micromeritics.com/Pressroom/Press-Release-List/GeoPyc-1360-Press-Release.aspx

[14] Fischer-Cripps AC. Nanoindentation. Springer; 2002. 217 p.

[15] Shelef L, Mohsenin N. Effect of Moisture Content on Mechanical Properties of Shelled Corn. Cereal Chem. 1969;

[16] Bedford AM, Fowler W. Engineering Mechanics: Statics and Dynamics Principles. Prentice Hall; 2002. 832 p.

[17] Wong C, Daniel M. Energy Dissipation Prediction of Particle Dampers. J Sound Vib. 2009;319:91–118.

[18] Shipway PH, Hutchings IM. Attrition of Brittle Spheres by Fracture Under Compression and Impact Loading. Powder Technol. 1993 Jul;76(1):23–30.

[19] Bemrose CR, Bridgwater J. A Review of Attrition and Attrition Test Methods. Powder Technol. 1987;49(2):97–126.

[20] Paramanathan BK, Bridgwater J. Attrition of Solids—II : Material Behaviour and Kinetics of Attrition. Chem Eng Sci. 1983 Jan;38(2):207–24.

[21] Gwyn JE. On the Particle Size Distribution Function and the Attrition of Cracking Catalysts. AIChE J. 1969;15(1):197–206.

[22] Benbow JJ, Bridgwater J. The Influence of Formulation on Extrudate Structure and Strength. Chem Eng Sci. 1987;42(4):753–66.

[23] Potapov A V., Campbell CS. Computer Simulation of Shear-induced Particle Attrition. Powder Technol. 1997 Dec;94(2):109–22.

[24] Neil AU. Particle Damage in Chemical Processing. University of Birmingham; 1986.

[25] Neil AU, Bridgwater J. Attrition of Particulate Solids Under Shear. Powder Technol. 1994 Sep;80(3):207–19.

[26] Schuhmann R. No Title. AIMETP. 1940;1189.

[27] Ouwerkerk CED. A Micro-mechanical Connection Between the Single-particle Strength and the Bulk Strength of Random Packings of Spherical Particles. Powder Technol. 1991 Mar;65(1-3):125–38.

[28] Kenter SJ. Wear and Fragmentation of Spherical Catalysts. University of Twente; 1992.

[29] Hare CL. Particle Breakage in Agitated Dryers. University of Leeds; 2010.

[30] USDA. Grain Grading Procedures. Washington DC: Federal Grain Inspection Service; 1980.

[31] Fiscus DE, Foster GH, Kaufmami HH. Physical Damage of Grain Caused by Various Handling Techniques. Trans Am Soc Agric Biol Eng. 1971;14(3):480–5.

[32] Paulsen MR, Hill LD. Breakage Susceptibility of Exported Corn at Origin and Destination. Trans Am Soc Agric Biol Eng. 1983;26(1):265–9.

[33] S. S. Singh MFF. A Centrifugal Impacter for Damage Susceptibility Evaluation of Shelled Corn. Trans Am Soc Agric Eng. 1983;26(6):1858–63.

[34] Thompson RA, Foster GH. Stress Cracks and Breakage in Artificially Dried Corn. USDA Mark Res Rep. 1963;631.

[35] Watson SA, Herum FL. Comparison of Eight Devices for Measuring Breakage Susceptibility of Shelled Corn. Cereal Chem. 1986;63(2):139–42.

[36] Asota C. Mechanical Seed Quality of Soyabeans Related to Drying Parameters. J Food Eng. 1997;8774(96).

[37] Dondee S, Meeso N, Soponronnarit S, Siriamornpun S. Reducing Cracking and Breakage of Soybean Grains under Combined Near-infrared Radiation and Fluidized-bed Drying. J Food Eng. Elsevier Ltd; 2011 May;104(1):6–13.

[38] Zhu HP, Zhou ZY, Yang RY, Yu AB. Discrete Particle Simulation of Particulate Systems: Theoretical Developments. Chem Eng Sci. 2007 Jul;62(13):3378–96.

[39] Cundall PA, Strack ODL. A Discrete Numerical Model for Granular Assemblies. Géotechnique. 1979 Jan 3;29(1):47–65.

[40] Solutions D. EDEM 2.2 User Guide. DEM Solutions; 2009.

[41] Ketterhagen WR, Am Ende MT, Hancock BC. Process Modeling in the Pharmaceutical Industry Using the Discrete Element Method. J Pharm Sci. 2009;98(20):442–70.

[42] Di Renzo A, Di Maio FP. Comparison of Contact-force Models for the Simulation of Collisions in DEM-Based Granular Flow Codes. Chem Eng Sci. 2004 Feb;59(3):525–41.

[43] Ahmadian H. Analysis of Enzyme Dust Formulation in Detergent Manufacturing Plant. University of Leeds; 2008.

[44] Thornton C, Ning Z. A Theoretical Model for the Stick/Bounce Behaviour of Adhesive, Elastic-plastic Spheres. Powder Technol. 1998;99(2):154–62.

[45] Mindlin RD, Deresiewicz H. Elastic Spheres in Contact Under Varying Oblique Forces. J Appl Mech. 1953;20:327–44.

[46] Favier JF, Abbaspour-Fard MH, Kremmer M. Modeling Nonspherical Particles Using Multisphere Discrete Elements. J Eng Mech. 2001;127:971–7.

[47] Cordelair J, Greil P. Discrete Element Modeling of Solid Formation During Electrophoretic Deposition. J Mater Sci. 2004;39(3):1017–21.

[48] Ting JM, Meachum L, Rowell JD. Effect of Particle Shape on the Strength and Deformation Mechanisms of Ellipse-shaped Granular Assemblages. Eng Comput. 1995;12(2):99–108.

[49] Cleary PW. DEM Prediction of Industrial and Geophysical Particle Flows. Particuology. Chinese Society of Particuology; 2010 Apr;8(2):106–18.

[50] Morgan JK. Particle Dynamics Simulations of Rate- and State-Dependent Frictional Sliding of Granular Fault Gouge. Pure Appl Geophys. 2004 Aug;161(9-10):1877–91.

[51] Ai J, Chen J-F, Rotter JM, Ooi JY. Assessment of Rolling Resistance Models in Discrete Element Simulations. Powder Technol. Elsevier B.V.; 2011 Jan;206(3):269–82.

[52] Zhou YC, Wright BD, Yang RY, Xu BH, Yu AB. Rolling Friction in the Dynamic Simulation of Sandpile Formation. Phys A Stat Mech its Appl. 1999 Jul;269(2-4):536–53.

[53] Iwashita K, Oda M. Rolling Resistance at Contacts in Simulation of Shear Band Development by DEM. J Eng Mech. 1998;124(3):285–92.

[54] Wensrich CM, Katterfeld A. Rolling Friction as a Technique for Modelling Particle Shape in DEM. Powder Technol. Elsevier B.V.; 2012 Feb;217:409–17.

[55] Favier JF, Abbaspour-Fard MH, Kremmer M, Raji AO. Shape Representation of Axi-Symmetrical, Non-Spherical Particles in Discrete Element Simulation Using Multi-Element Model Particles. Eng Comput. 1999;16(4):467–80.

[56] Kodam M, Bharadwaj R, Curtis J, Hancock B, Wassgren C. Force Model Considerations for Glued-sphere Discrete Element Method Simulations. Chem Eng Sci. 2009 Aug;64(15):3466–75.

[57] Kruggel-Emden H, Rickelt S, Wirtz S, Scherer V. A study on the validity of the multi-sphere discrete element method. Powder Technol. Elsevier B.V.; 2008 Dec;188(2):153–65.

[58] González-Montellano C, Ramírez Á, Gallego E, Ayuga F. Validation and Experimental Calibration of 3D Discrete Element Models for the Simulation of the Discharge Flow in Silos. Chem Eng Sci. 2011 Nov;66(21):5116–26.

[59] Balevičius R, Kačianauskas R, Mróz Z, Sielamowicz I. Discrete-Particle Investigation of Friction Effect in Filling and Unsteady/Steady Discharge in Three-dimensional Wedge-Shaped Hopper. Powder Technol. 2008 Oct;187(2):159–74.

[60] González-Montellano C, Gallego E, Ramírez-Gómez Á, Ayuga F. Three Dimensional Discrete Element Models for Simulating the Filling and Emptying of Silos: Analysis of Numerical Results. Comput Chem Eng. Elsevier Ltd; 2012 May;40:22–32.

[61] Lu Z, Negi SC, Jofriet JC. A Numerical Model for Flow of Granular Materials in Silos . Part 1 : Model Development. 1997;223–9.

[62] Li J, Webb C, Pandiella S. A Numerical Simulation OF Separation of Crop Seeds by Screening — Effect of Particle Bed Depth. Food Bioprod. 2002;80(June).

[63] Kalbag A, Wassgren C. Inter-tablet Coating Variability: Tablet Residence Time Variability. Chem Eng Sci. 2009;64(11):2705–17.

[64] Muliadi AR, Sojka PE. a Review of Pharmaceutical Tablet Spray Coating. At Sprays. 2010;20(7):611–38.

[65] Yamane K, Sato T, Tanaka T, Tsuji Y. Computer Simulation of Tablet Motion in Coating Drum. Pharm Res. Kluwer Academic Publishers-Plenum Publishers; 1995;12(9):1264–8.

[66] Leaver TM, Shannon HD, ROWE RC. A Photometric Analysis of Tablet Movement in a Side-vented Perforated Drum (Accela-Cota). J Pharm Pharmacol. Blackwell Publishing Ltd; 1985;37(1):17–21.

[67] Park J, Wassgren CR. Modeling the Dynamics of Fabric in a Rotating Horizontal Drum Using the Discrete Element Method. Part Sci Technol. 2003;21(2):157–75.

[68] Sandadi S, Pandey P, Turton R. In Situ, Near Real-time Acquisition of Particle Motion in Rotating Pan Coating Equipment using Imaging Techniques. Chem Eng Sci. 2004;59(24):5807–17.

[69] Toschkoff G, Just S, Funke A, Djuric D, Knop K, Kleinebudde P, et al. Spray Models for Discrete Element Simulations of Particle Coating Processes. Chem Eng Sci. 2013 Sep;101:603–14.

[70] Mellmann J. The Transverse Motion of Solids in Rotating Cylinders-forms of Motion and Transition Behavior. Powder Technol. 2001;118(3):251–70.

[71] Kalbag A, Wassgren C, Sumana Penumetcha S, Pérez-Ramos JD. Inter-tablet Coating Variability: Residence Times in a Horizontal Pan Coater. Chem Eng Sci. 2008;63(11):2881–94.

[72] Ketterhagen WR, Curtis JS, Wassgren CR. Stress Results from Two-dimensional Granular Shear Flow Simulations using Various Collision Models. Phys Rev E - Stat Nonlinear, Soft Matter Phys. 2005;71(6):1–11.

[73] Acharya A. A Distinct Element Approach to Ball Mill Mechanics. Commun Numer Methods Eng. 2000;16(11):743–53.

[74] Cleary P. Modelling Comminution Devices using DEM. Int J Numer Anal Methods Geomech. 2001;25(1):83–105.

[75] Moreno-Atanasio R, Xu BH, Ghadiri M. Computer Simulation of the Effect of Contact Stiffness and Adhesion on the Fluidization Behaviour of Powders. Chem Eng Sci. 2007 Jan;62(1-2):184–94.

[76] Lommen S, Schott D, Lodewijks G. DEM speedup: Stiffness Effects on Behavior of Bulk Material. Particuology. Chinese Society of Particuology; 2014 Feb;12:107–12.

[77] Prater DA, Wilde JS, Meakin BJ. A Model System for the Production of Aqueous Tablet Film Coatings for Laboratory Evaluation. J Pharm Pharmacol. Blackwell Publishing Ltd; 1980;32(S1):90P – 90P.

[78] Pandey P, Turton R. Movement of Different-shaped Particles in a Pan-coating Device using Novel Video-imaging Techniques. AAPS PharmSciTech. 2005;6(2):E237–44.

[79] Pandey P, Song Y, Kayihan F, Turton R. Simulation of Particle Movement in a Pan Coating Device using Discrete Element Modeling and its Comparison with Video-imaging Experiments. Powder Technol. 2006;161(2):79–88.

[80] Suzzi D, Toschkoff G, Radl S, Machold D, Fraser SD, Glasser BJ, et al. DEM Simulation of Continuous Tablet Coating: Effects of Tablet Shape and Fill Level on Inter-tablet Coating Variability. Chem Eng Sci. 2012 Feb;69(1):107–21.

[81] Brone D, Muzzio F. Enhanced Mixing in Double-cone Blenders. Powder Technol. 2000 Jun;110(3):179–89.

[82] Lacey PMC. Developments in the Theory of Particle Mixing. J Appl Chem. 2007 May 4;4(5):257–68.

[83] Li J, Wassgren C, Litster JD. Multi-scale Modeling of a Spray Coating Process in a Paddle Mixer/Coater: The Effect of Particle Size Distribution on Particle Segregation and Coating Uniformity. Chem Eng Sci. 2013 May;95:203–10.

[84] Just S, Toschkoff G, Funke A, Djuric D, Scharrer G, Khinast J, et al. Optimization of the Inter-tablet Coating Uniformity for an Active Coating Process at Lab and Pilot Scale. Int J Pharm. 2013 Nov 30;457(1):1–8.

[85] Hilton JE, Ying DY, Cleary PW. Modelling Spray Coating using a Combined CFD–DEM and Spherical Harmonic Formulation. Chem Eng Sci. Elsevier; 2013;99:141–60.

[86] Hsieh J. Computed Tomography: Principles, Design, Artifacts, and Recent Advances. SPIE; 2009. 556 p.

[87] Rothenburg L, Bathurst RJ. Numerical Simulation of Idealized Granular Assemblies with Plane Elliptical Particles. Comput Geotech. 1991 Jan;11(4):315–29.

[88] Cundall PA. Formulation of a Three-Dimensional Distinct Element Model—Part I. A Scheme to Detect and Represent Contacts in a System Composed of Many Polyhedral Blocks. Int J Rock Mech Min Sci Geomech Abstr. 1988 Jun;25(3):107–16.

[89] Potapov A V., Campbell CS. A Three-Dimensional Simulation of Brittle Solid Fracture. Int J Mod Phys C. World Scientific Publishing Company; 1996 Oct 20;07(05):717–29.

[90] Pournin L, Weber M, Tsukahara M, Ferrez J a., Ramaioli M, Liebling TM. Three-dimensional Distinct Element Simulation of Spherocylinder Crystallization. Granul Matter. 2005;7(2-3):119–26.

[91] Williams JR, Pentland AP. Superquadrics and Modal Dynamics for Discrete Elements in Interactive Design. Eng Comput. MCB UP Ltd; 1992 Feb 11;9(2):115–27.